



PHD

## Optical fibre transitions for device applications

Leon-Saval, Sergio G.

*Award date:*  
2005

*Awarding institution:*  
University of Bath

[Link to publication](#)

## Alternative formats

If you require this document in an alternative format, please contact:  
[openaccess@bath.ac.uk](mailto:openaccess@bath.ac.uk)

### General rights

Copyright and moral rights for the publications made accessible in the public portal are retained by the authors and/or other copyright owners and it is a condition of accessing publications that users recognise and abide by the legal requirements associated with these rights.

- Users may download and print one copy of any publication from the public portal for the purpose of private study or research.
- You may not further distribute the material or use it for any profit-making activity or commercial gain
- You may freely distribute the URL identifying the publication in the public portal ?

### Take down policy

If you believe that this document breaches copyright please contact us providing details, and we will remove access to the work immediately and investigate your claim.

# OPTICAL FIBRE TRANSITIONS FOR DEVICE APPLICATIONS

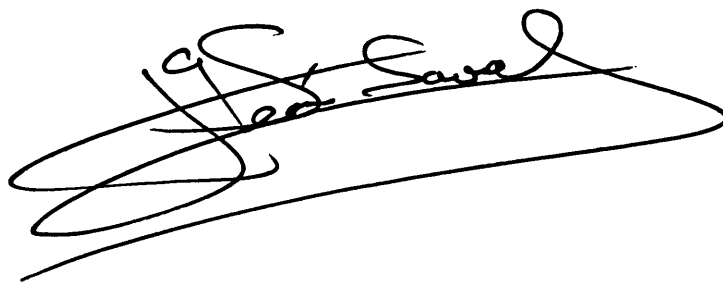
Submitted by Sergio G. Leon-Saval

for the degree of

Doctor of Philosophy

of the University of Bath

October 2005

A handwritten signature in black ink, appearing to read 'Sergio G. Leon-Saval', written over a horizontal line.

## COPYRIGHT

Attention is drawn to the fact that copyright of this thesis rests with its author. This copy of the thesis has been supplied on condition that anyone who consults it is understood to recognise that its copyright rests with its author and no information derived from it may be published without the prior written consent of the author.

This thesis may be made available for consultation within the University library and may be photocopied or lent to other libraries for the purposes of consultation.

UMI Number: U208558

All rights reserved

INFORMATION TO ALL USERS

The quality of this reproduction is dependent upon the quality of the copy submitted.

In the unlikely event that the author did not send a complete manuscript and there are missing pages, these will be noted. Also, if material had to be removed, a note will indicate the deletion.



UMI U208558

Published by ProQuest LLC 2013. Copyright in the Dissertation held by the Author.  
Microform Edition © ProQuest LLC.

All rights reserved. This work is protected against  
unauthorized copying under Title 17, United States Code.



ProQuest LLC  
789 East Eisenhower Parkway  
P.O. Box 1346  
Ann Arbor, MI 48106-1346

LIBRARY OF CONGRESS  
45 14 JUL 2005  
Ph.D.

---

*“It is not because things are difficult that we do not dare;  
it is because we do not dare that they are difficult.”*

Seneca (5 BC - 65 AD)

---

# Abstract

This thesis focuses on the exploration of different applications and devices based on optical fibre transitions. These are made by two methods: tapering and fibre drawing. Two types of optical fibres have been considered, conventional step-index single-mode optical fibres (SMFs) and photonic crystal fibres (PCFs), the latter having an array of holes along the length of the fibre in the cladding.

I carried out two studies of tapered SMFs. Firstly I investigated tapered fibres surrounded by porous sol-gel derived silica. This took the form of thin relatively dense layers, or tapered SMFs were embedded in aerogel. Both were achieved with low losses for the first time. Secondly, SMFs were tapered to submicron waists that exhibit unusual dispersion and nonlinear properties.

When tapering PCFs there is an extra degree of freedom, the size of the air holes. I demonstrated the ability to control this and exploited it to interface PCFs to SMFs and other systems. Firstly, “fast and cold” tapering (to minimise hole collapse) was used to simultaneously make and interface to submicron-core PCFs. Secondly, a new hole-inflation technique took advantage of the new degree of freedom to interface between large-core and small-core PCFs. The third method was to incorporate an SMF inside a PCF preform and draw the entire structure to fibre. The final PCF core is formed by the tapered-down SMF. This method enables interfacing to any kind of index-guiding PCF, all-fibre mode convertors, and multimode fibre devices with single-mode performance. A variation of the technique led to low-contrast solid bandgap fibres.

In this way I have demonstrated several new types of transitions and shown how they can be exploited in a range of device applications.

# Acknowledgements

Esta tesis esta dedicada a mi familia por todo el apoyo durante estos largos años en el “exilio”. En especial a mis padres Ramón y Mercedes por haber aguantado a este “cascarrabias” comprendiendo y respetando mis decisiones durante estos años.

Os echo de menos.....

Debo agradecer también todo el apoyo prestado por el “club de exiliados”: Antonio, Sergio, Clara, Julio, Iliana, Arturo y el “hijo prodigo” Fernandito. Los cuales han compartido penas y glorias durante estos años y siempre han estado ahí como una familia para mí. Agradecimientos deben ir también a todos mis amigos en Sevilla: Fernando, Alberto, Rafa, Ale....(demasiados para completar la lista). Los cuales cada vez que vuelvo, después de cinco años, me hacen sentir como si nunca me hubiera ido.

A todos muchas gracias de corazón.....

.....

I would like to dedicate this thesis to the love of my life, Susan. Thanks for all your support and love during the past four years that we have been together. I must also thank my English “family” David and Mary for “adopting” me during theses years.

I specially would like to thank my supervisor Tim Birks for his motivating and enthusiastic supervision. Thank you very much for all the support and the many many hours that you dedicated to help and supervise me over the three years of my PhD.

I must also thank Philip Russell and Jonathan Knight for giving me the opportunity of working in such a great research group.

Many thanks to the entire optogroup and physics department people from the University of Bath, in particular:

William Wadsworth the “soundproof” man (just kidding...) for all the ideas and help in the lab. Alan George (god! this man knows how to do everything?....) for all the help and lessons in fibre drawing. The office group Ravi, Georges (paper?....I believe I am wining the race...), Mathew and Agata for making the office and the labs a more

enjoyable place. Nico the “fibre drawing guru” (good luck in Lille...keep in touch). George Kakarantzas for introducing me into the “tapering world”. Fetah thanks for your always original and peculiar point of view, never change. Fabio, Roberts, Pottage and Alex the “theory gang”, wonderful guys. Eva, the “engine” of the department, always helpful and nice no matter how much you bother her. Wendy the friendliest person in the world, a pleasure meeting you. To the rest of the people that I have probably forgot to mention. Thank you all.



# Contents

<b>Publications</b>	<b>ix</b>
<b>List of Abbreviations</b>	<b>xii</b>
<b>1. Conventional Step-Index Silica Optical Fibres</b>	<b>1</b>
1.1. Fabrication Process.....	2
1.2. Light Guiding in Conventional Fibres.....	3
1.3. Losses in Conventional Optical Fibres.....	9
<b>2. Photonic Crystal Fibres and Tapered Fibres</b>	<b>12</b>
2.1. Photonic Crystal Fibres (PCFs).....	12
2.1.1. Fabrication Process.....	13
2.1.2. Index Guiding PCFs.....	14
2.1.3. Bandgap Guiding PCFs .....	16
2.2. Tapered Optical Fibres.....	18
2.2.1. Fabrication Process.....	19
2.2.2. Optical Properties.....	20
2.2.3. Tapered PCFs.....	21
2.3. Nonlinear Optics in Optical Fibres .....	22
2.3.1. Nonlinear Refractive Index.....	23
2.3.2. Four-Wave Mixing (FWM).....	23
2.3.3. Supercontinuum (SC) Generation in PCF and Tapered Fibres.....	24

<b>3. Sol-Gel, Aerogel and Tapered Conventional Fibres</b>	<b>27</b>
3.1. Sol-Gel Coating of Tapered Fibres.....	27
3.1.1. Sol Preparation .....	29
3.1.2. Coating Technique.....	29
3.1.3. Laser Densification of Porous Films on Tapered Fibres.....	31
3.2. Tapered Fibres Embedded in Aerogel .....	39
3.2.1. Synthesis of Aerogel.....	40
3.2.2. Experimental Work.....	42
3.3. Conclusions.....	46
<b>4. Submicron Fibre Waveguides</b>	<b>47</b>
4.1. Dispersion in Submicron Fibre Waveguides.....	47
4.2. Submicron Tapered SMFs.....	49
4.2.1. Fabrication and Loss of Submicron SMF Tapered Fibres .....	49
4.2.2. Nonlinearity in Submicron Tapered SMFs.....	51
4.3. Submicron-Core PCFs.....	54
4.3.1. Fabrication of Submicron-Core PCFs by Tapering.....	54
4.3.2. Nonlinearity in Submicron-Core PCFs.....	56
4.4. Discussion and Conclusion.....	57
<b>5. Hole Inflation in PCFs</b>	<b>59</b>
5.1. Hole Collapse/Expansion and Surface Tension.....	60
5.2. Adiabaticity in Hole Size Transitions.....	61
5.3. Hole Inflation and Tapering Technique.....	62

5.4. Experiment.....	64
5.4.1. Hole Inflation Without Tapering.....	64
5.4.2. Hole Inflation and Tapering to Small-Core PCFs.....	67
5.4.3. Nonlinear Application.....	69
5.5. Core Shape Transitions.....	70
5.5.1. Optical Measurements.....	72
5.6. Conclusion.....	74
<b>6. Interfacing SMFs to PCFs: The “Ferrule” Idea</b>	<b>75</b>
6.1. Ferrule Transition Idea.....	75
6.2. Experimental Technique.....	76
6.2.1. Endlessly Single-Mode PCFs.....	79
6.2.2. Highly Nonlinear PCFs.....	81
6.3. Conclusion.....	83
<b>7. Using Ferrules to Interface More than One SMF to One PCF</b>	<b>84</b>
7.1. Multicore PCF.....	84
7.1.1. Experiment: Two-Core PCF.....	85
7.2. Fibre Mode Convertor.....	86
7.2.1. Principle of Operation.....	87
7.2.2. Experiment: $LP_{01}$ to $LP_{11}$ Mode Convertor.....	89
7.3. Multimode Fibre Device with Single-Mode Performance.....	91
7.3.1. Transition Between an MMF and Several SMFs.....	93
7.3.2. SMF Bragg Grating Response in a Multimode Fibre Device.....	95
7.4. Conclusion.....	98

<b>8. All Solid-Silica Photonic Bandgap Fibres</b>	<b>99</b>
8.1. Fabrication.....	100
8.2. Optical Characterisation .....	103
8.3. Conclusion.....	106
<b>9. Conclusions</b>	<b>107</b>
9.1. Summary .....	107
9.2. Future Work Directions.....	110
<b>Figures and Tables</b>	<b>112</b>
<b>References</b>	<b>120</b>

# Publications

The following is a list of papers published or submitted to refereed journals as a result of work done in this Ph.D.

1. G.Kakarantzas, S.G.Leon-Saval, T.A.Birks, P.St.J.Russell: "Low-loss deposition of sol-gel derived silica films on tapered fibers", *Optics Letters*, 29, April 2004, pp.694-696.
2. S.G.Leon-Saval, T.A.Birks, W.J.Wadsworth, P.St.J.Russell, M.W.Mason: "Supercontinuum generation in submicron fibre waveguides", *Optics Express*, 12, June 2004, pp.2864-2869.
3. A.Argyros, T.A.Birks, S.G.Leon-Saval, C.M.B.Cordeiro, F.Luan, P.St.J.Russell: "Photonic bandgap with an index step of one percent", *Optics Express*, 13, January 2005, pp.309-314.
4. A.Argyros, T.A.Birks, S.G.Leon-Saval, C.M.B.Cordeiro, P.St.J.Russell: "Guidance properties of low-contrast photonic bandgap fibres", *Optics Express*, 13, April 2005, pp.2503-2511.
5. S.G.Leon-Saval, T.A.Birks, N.Y.Joly, A.K.George, W.J.Wadsworth, G.Kakarantzas, P.St.J.Russell: "Splice-free interfacing of photonic crystal fibers", *Optics Letters*, 30, July 2005, pp.1629-1631.
6. S.G.Leon-Saval, T.A.Birks, N.Y.Joly, A.K.George, W.J.Wadsworth, G.Kakarantzas, P.St.J.Russell: "Splice-free interfacing of photonic crystal fibers", *Virtual Journal on Nanoscale Science and Technology*, 12, July 2005.
7. W.J.Wadsworth, A.Witkowska, S.G.Leon-Saval, T.A.Birks: "Hole inflation and tapering of stock photonic crystal fibres", *Optics Express*, 13, August 2005, pp.6541-6549.
8. S.G.Leon-Saval, T.A.Birks, J.Bland-Hawthorn, M.Englund: "Multimode fibre devices with single-mode performance", *Optics Letters*, 30, October 2005, pp.2545-2547.

The following is a list of publications in national and international conferences as a result of work done during the course of this Ph.D.

1. S.G.Leon-Laval, G.Kakarantzas, T.A.Birks, P.St.J.Russell: "Tapered photonic crystal fibre transitions and devices", presented at the Rank Prize Funds Mini-Symposium on Passive Optical Components (Grasmere, UK), June 2003.
2. G.Kakarantzas, S.G.Leon-Saval, T.A.Birks, P.St.J.Russell: "All-fiber devices based on sol-gel coated tapered fibers", Proceedings of the Conference on Lasers and Electro-Optics (CLEO, San Francisco, California), May 2004, paper CWM6.
3. S.G.Leon-Saval, G.Kakarantzas, A.K.George, T.A.Birks, P.St.J.Russell: "Splice-less interfacing of conventional fibers to photonic crystal fibers", Proceedings of the Conference on Lasers and Electro-Optics (CLEO, San Francisco, California), May 2004, paper CThCC7.
4. S.G.Leon-Saval, T.A.Birks, W.J.Wadsworth, P.St.J.Russell, M.W.Mason: "Efficient single-mode supercontinuum generation in submicron-diameter silica-air fibre waveguides", Proceedings of the Conference on Lasers and Electro-Optics (CLEO, San Francisco, California), May 2004, *postdeadline paper* CPDA6.
5. T.A.Birks, S.G.Leon-Saval, C.M.B.Cordeiro, W.J.Wadsworth, G.Antonopoulos, P.St.J.Russell: "New waveguides for old: tapering conventional and photonic crystal fibres down to the nano-scale", Proceedings of the Australian Conference on Optical Fibre Technology (ACOFT, Canberra, Australia), July 2004 (*invited*).
6. S.G.Leon-Saval, W.J.Wadsworth, T.A.Birks, P.St.J.Russell, M.W.Mason: "Visible broadband continuum generation in nano-scale silica-air waveguides", presented at the Summer School on Advanced Glass-Based Nano-Photonics (POWAG, Bath, UK), July 2004.
7. S.G.Leon-Saval, T.A.Birks, J.Bland-Hawthorn, M.Englund: "Single-mode performance in multimode fibre devices", Proceedings of the Optical Fiber Communication Conference (OFC, Anaheim, California), March 2005, *postdeadline paper* PDP25.
8. T.A.Birks, S.G.Leon-Saval, W.J.Wadsworth, P.St.J.Russell: "Optical micro- and nano-structures using fibre tapers", Proceedings of the Conference on Lasers and Electro-Optics (CLEO, Baltimore, Maryland), May 2005, paper CMD1 (*invited*).
9. S.G.Leon-Saval, T.A.Birks, A.K.George, W.J.Wadsworth, P.St.J.Russell: "Wavelength-independent high-extinction fibre mode convertor", Proceedings of the Conference on Lasers and Electro-Optics (CLEO, Baltimore, Maryland), May 2005, paper CThZ2.
10. T.A.Birks, S.G.Leon-Saval, J.Bland-Hawthorn, M.Englund: "Adiabaticity in multicore fibre transitions", Proceedings of the Workshop on Optical Waveguide Theory and Numerical Modelling (Sydney, Australia), July 2005, p.19 (*invited*).

11. A.Argyros, T.A.Birks, S.G.Leon-Saval, C.M.B.Cordeiro, P.St.J.Russell: "Scalar photonic bandgap fibres", Proceedings of the Workshop on Photonic Crystals: Fundamentals to Devices (Sydney, Australia), July 2005, p.49.
12. A. Witkowska, W. J. Wadsworth, S. G. Leon-Saval, T. A. Birks, "Novel optical devices made by inflating the holes of a photonic crystal fibre", Photonex Europe 05, October 2005, Coventry (UK).

Patents filed from work done during this PhD:

1. T.A.Birks, S.G.Leon-Saval, J.C.Knight, J.Bland-Hawthorn: "Improvements in and relating to optical-fibre devices (chinese lantern)", British patent application number 0504083.7, February 2005.
2. W. J. Wadsworth, T. A. Birks, S. G. Leon-Saval, A. Witkowska: "Differential Fibre Inflation", Submitted for British patent, September 2005.

Articles appeared in technical press from work carried out during this PhD:

1. Photonics Spectra, USA, Breck Hitz, "Holey Fibers Connect to Conventional Fibers with Low Loss", Aug 2005, Vol 39, 8, pp.84-85.
2. Photonics Spectra, USA, Breck Hitz, "Multimode Fiber Thinks It's Singlemode", to appear in December 2005.

# List of Abbreviations

<i>AD</i>	Anomalous Dispersion
<i>ARROW</i>	Antiresonant Reflecting Optical Waveguide
<i>ESM</i>	Endlessly Single-Mode
<i>FSM</i>	Fundamental Space-Filling Mode
<i>FWM</i>	Four-Wave Mixing
<i>GVD</i>	Group-Velocity Dispersion
<i>HC-PCF</i>	Hollow-Core Photonic Crystal Fibre
<i>IMF</i>	Index Matching Fluid
<i>LPG</i>	Long Period Grating
<i>MFD</i>	Mode Field Diameter
<i>MCVD</i>	Modified Chemical Vapour Deposition
<i>MMF</i>	Multimode Fibre
<i>NA</i>	Numerical Aperture
<i>ND</i>	Normal Dispersion
<i>OD</i>	Outer Diameter
<i>PBG</i>	Photonic Bandgap
<i>PCF</i>	Photonic Crystal Fibre
<i>SC</i>	Supercontinuum
<i>SEM</i>	Scanning Electron Microscope
<i>SIF</i>	Step-Index Fibre
<i>SMF</i>	Single-Mode Fibre
<i>SPM</i>	Self-Phase Modulation
<i>TEOS</i>	Tetraethoxysilane
<i>TIR</i>	Total Internal Reflection
<i>TMOS</i>	Tetramethoxysilane
<i>UV</i>	Ultra-Violet
<i>ZDW</i>	Zero-Dispersion Wavelength



---

# Chapter 1

## Conventional Step-Index Silica Optical Fibres

For many years optical fibres have been developed for many different applications. The achievements of low-loss transmission, along with the advantages of large information carrying capacity, immunity from electromagnetic interference, and small size and weight, have created the technology of optical telecommunications. A wide range of techniques and instruments have been developed to handle and process these fibres [Agrawal 95, Hecht 99]. Optical fibre is also used in sensor applications, where the high sensitivity, low loss, and electromagnetic interference immunity of the fibres can be exploited. Optical fibres are versatile and sensors can be designed to detect many physical parameters, such as temperature, pressure, strain, and electrical and magnetic fields, using either the power transmission properties of multimode fibres or the phase sensitive properties of single-mode fibres.

The conventional step-index optical fibre design has been refined during the last decades but remains basically the same. The optical fibre is a cylindrical waveguide. The basic structure consists of a central light-carrying portion, called the core, which is surrounded by a cylindrical region, called the cladding. The cladding is then covered with a protective plastic coating (Fig. 1.1). The most widely used conventional telecoms fibre is the well-known Corning SMF-28. This is a single-mode fibre with a silica Ge doped core of 9  $\mu\text{m}$  in diameter and an outer diameter cladding of 125  $\mu\text{m}$  with a polymer coating jacket. The total diameter of the fibre including the coating is around 250  $\mu\text{m}$ . The SMF-28 is single-mode (explained in Subsection 1.2) for all wavelengths beyond 1260 nm.

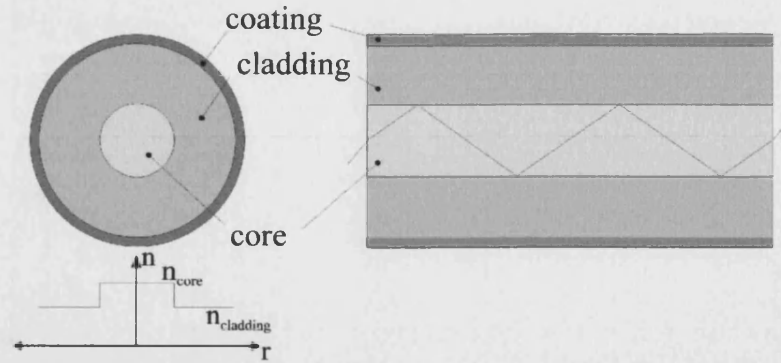


Fig. 1.1. Schematic diagram of a conventional step-index fibre.

### 1.1. Fabrication Process

Fabrication of silica fibres involves two stages. In the first stage a vapour-phase technique such as modified chemical vapour deposition (MCVD) [Nagel 82] is used to make a cylindrical preform with the desired refractive index profile. The MCVD process is also known as inner-vapor-deposition method, as the core and the cladding layers are deposited inside a silica tube. The final preform is typically around 1 m long and a couple of cm in diameter and contains core and cladding layers with the correct relative dimensions for the desired fibre.

In the second stage the preform is fed into a furnace in a controlled manner where it is heated to a temperature of about  $2000^{\circ}\text{C}$ . It is drawn into fibre by using a precision feed mechanism (Fig. 1.2). During the process the fibre a polymer coating is applied for protecting the fibre, which gives a better mechanical strength to the fibre. The fibre diameter is accurately controlled by a laser diameter monitor. The diameter  $\varnothing_f$  of the final fibre is governed by the feeding speed of the preform  $v_p$ , the pulling speed of the tractor or fibre drawing speed  $v_f$  and the diameter of the preform  $\varnothing_p$ . Conservation of mass gives the following equation:

$$\frac{\varnothing_p}{\varnothing_f} = \left( \frac{v_f}{v_p} \right)^{1/2} \quad \text{Equation (1.1)}$$

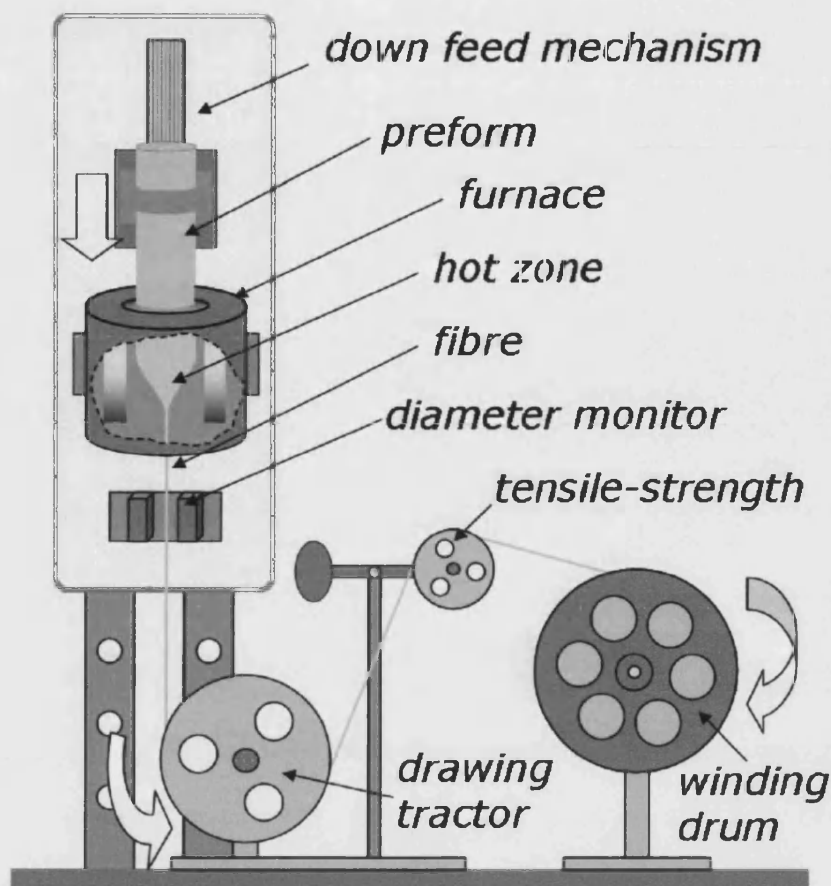


Fig. 1.2. Schematic drawn of the most significant parts of a fibre drawing tower.

Important parameters such as surface tension and stress have to be taken into account during the drawing process. These parameters will be discussed in Chapter 4, when photonic crystal fibres with internal structures have to be drawn.

## 1.2. Light Guiding in Conventional Fibres

Conventional optical fibres guide light by total internal reflection (TIR). TIR is explained by Snell's law which defines the behaviour of an electromagnetic wave when this one is incident upon the boundary between two dielectric media with different refractive indices  $n$ . In general a portion of that wave is reflected and the remainder transmitted. We suppose the wave to be incident on the interface at an angle  $\theta_1$  to the normal and that the reflected and transmitted waves are at angles  $\theta_1$  and  $\theta_2$  respectively, as shown in Fig. 1.3.

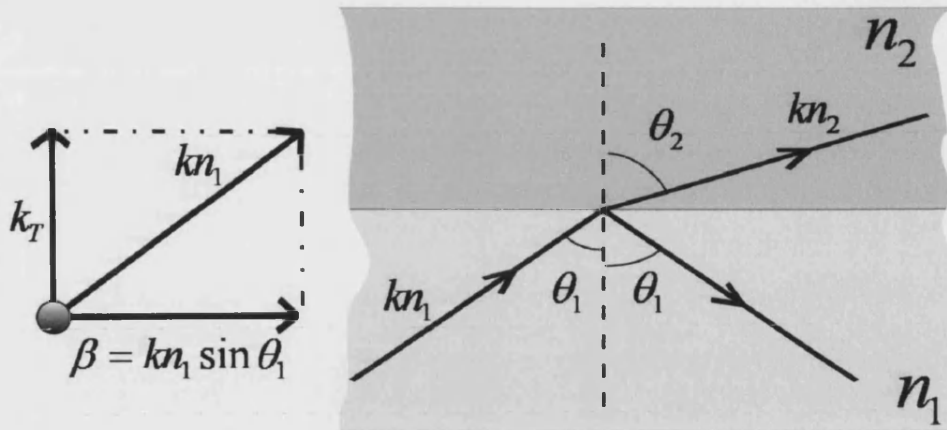


Fig. 1.3. Illustration of the behaviour of a light ray incident on the boundary between two media with refractive indices  $n_1$  and  $n_2$  where  $n_2 < n_1$ . In general, a transmitted and a reflected beam are produced. It is also shown that the propagation constant  $\beta$  is the projection of the wave vector  $kn_1$  onto the horizontal axis.

These angles are related by the Snell's law:

$$n_1 \sin \theta_1 = n_2 \sin \theta_2 \quad \text{Equation (1.2)}$$

We will be particularly interested in the situation when  $n_1 > n_2$  and when  $\theta_1 > \theta_c$  since it is then possible to have TIR, where:

$$\theta_c = \sin^{-1} \left( \frac{n_2}{n_1} \right) \quad (\text{where } \sin \theta_2 = 1 \text{ at } \theta_1 = \theta_c) \quad \text{Equation (1.3)}$$

The propagation constant  $\beta$  is the projection onto the horizontal axis of a wave vector  $kn_1$  propagating in a medium with refractive index  $n_1$  (Fig. 1.3). From here we can see that the value of  $\beta$  always is  $\leq kn_1$ . If we multiple by the wave number  $k = 2\pi/\lambda$  on both sides of Snell's law [Equation (1.2)], we find that the propagation constant is conserved:

$$kn_1 \sin \theta_1 = kn_2 \sin \theta_2 = \beta \quad \text{Equation (1.4)}$$

Since for TIR to occur  $\theta_1 > \theta_c$ , then  $\beta > kn_2$ , so the propagation constant of the wave under TIR has to lie within the range of values

$$kn_2 < \beta < kn_1 \quad \text{Equation (1.5)}$$

So far we have explained the behaviour of an incident wave onto the boundary between two infinite dielectric media with different refractive indices. But an optical fibre has a finite core. To make the analogy to an optical fibre we will consider again two dielectric media with refractive indices  $n_1$  and  $n_2$ . The medium with a higher refractive index  $n_1$  and width  $a$  is surrounded by an infinite medium with a lower refractive index  $n_2$ , in such way that TIR occurs [Fig. 1.4(a)].

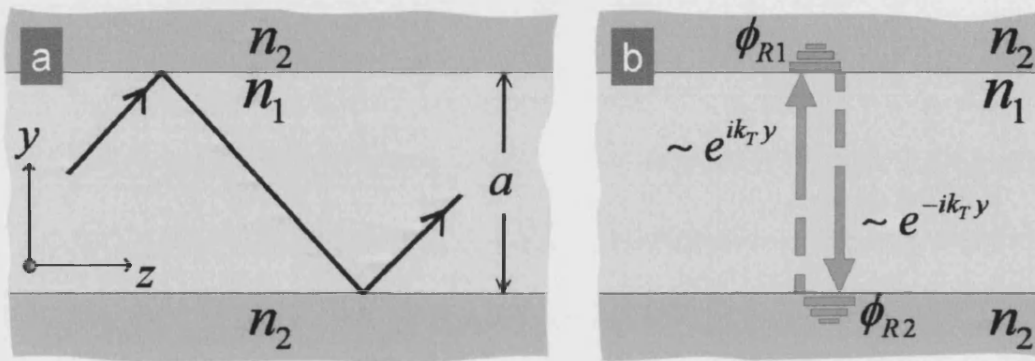


Fig. 1.4. (a) Illustration of the behaviour of a light ray travelling within a finite dielectric medium of width  $a$  and with a higher refractive index  $n_1$ , surrounded by an infinite dielectric medium with a lower refractive index  $n_2$ . (b) Schematic representation of the transverse phase change over a round trip.

When a wave travels between within these boundaries we can estimated how the phase of the wave varies transversely. Locally as the wave makes a round trip, the phase of the wave varies as  $\sim e^{ik_T y}$  and  $\sim e^{-ik_T y}$  respectively. Also the phase changes in each reflection by  $\phi_{R1}$  and  $\phi_{R2}$  respectively [Fig. 1.4(b)]. We can express the total change in phase after a round trip of the wave as follows:

$$\phi_{Total} = k_T a + \phi_{R1} + k_T a + \phi_{R2} \quad \text{Equation (1.5)}$$

where  $k_T$  is the transverse component of the wave vector  $kn_1$  (Fig. 1.3). For the wave to propagate along the waveguide it has to suffer constructive interference. This means that the total change in phase after a round trip must be an integer multiple of  $2\pi$ .

From this condition it follows that  $k_T$  is not continuous but discrete.  $k_T$  and the propagation constant  $\beta$  are related by

$$k_T = \left(k^2 n_1^2 - \beta^2\right)^{\frac{1}{2}} \quad \text{Equation (1.6)}$$

we can see that the allowed  $\beta$  in the waveguide is also discrete. Each of the propagation constants correspond to a *mode of the waveguide*. A mode is a wave whose field distribution remains unchanged along the propagation axis with the exception of the phase.

It can be shown that for a step-index fibre the number of modes ( $N$ ) that can be propagated in the core is determined by a parameter which is called the *normalised frequency* or *V parameter* and is defined as follows [Snyder 83]:

$$V = \frac{2\pi a}{\lambda} \sqrt{(n_1^2 - n_2^2)} = \frac{2\pi a}{\lambda} (NA) \quad \text{Equation (1.7)}$$

where  $\lambda$  is the *wavelength in the vacuum*,  $a$  is the radius of the core, and  $NA = \sqrt{(n_1^2 - n_2^2)}$  is the *numerical aperture* of the fibre. In a step-index fibre with a large  $V$  parameter the number of modes propagating in the fibre can be approximated by:

$$N \approx \frac{V^2}{4} \quad \text{Equation (1.8)}$$

This approximation gives the number of spatial modes, but if polarization states are counted separately this number should be multiplied by 2.

As  $V$  decreases, the modes with the smallest propagation constants  $\beta$  stop being guided. This is referred to as the cut off of a mode. It may be shown [Snyder 83] that when  $V$  is less than 2.405 for a certain wavelength only one mode can propagate along the fibre. This mode is referred to as the *fundamental mode*. When an optical fibre can only propagate the fundamental mode at a certain wavelength the fibre is described as a *single-mode fibre (SMF)*. As  $V$  increases, the next mode to be guided is called the *second mode*. For a given optical fibre, the wavelength at which the value of the  $V$  parameter is

equal to 2.405 is called the *cut off wavelength*. When an optical fibre is designed to support more than one mode it is called a *multimode fibre (MMF)*, although Equation (1.7) shows that even an SMF becomes multimode for sufficiently short wavelengths.

The field intensity distribution of the light in the fundamental mode of the fibre has a Gaussian-like profile, Fig. 1.5. Even in the case of the full internal reflection, the light wave does always penetrate slightly in the material beyond the interface. This field propagating along the cladding is known as the *evanescent field*. This evanescent field is characteristic of every mode. For a given mode as  $V$  decreases, the evanescent field extends further into the cladding and light in that mode becomes less well guided. In practice the growth of bend loss as  $V$  decreases means that an SMF is only an effective low-loss waveguide for  $V \geq 1$  approximately [Black 87].

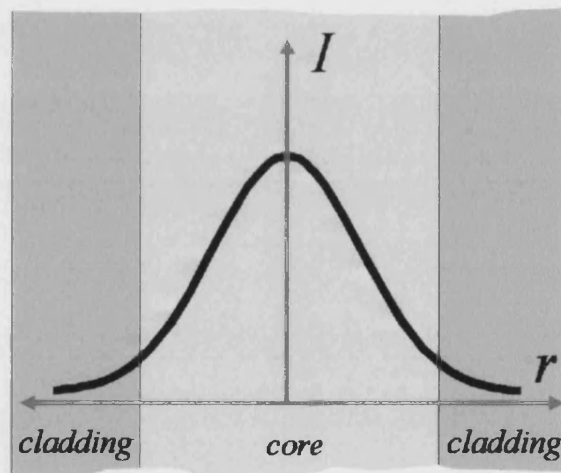


Fig. 1.5. Illustration of the mode field intensity distribution of the fundamental mode of an optical fibre. The Gaussian-like tails of the intensity profile spread into the cladding forming the evanescent field.

It is convenient to introduce a parameter to quantify how much a mode spreads. This is the *mode field diameter (MFD)* and can be defined by [Gambling 77]:

$$MFD = 2 \left( \frac{\int_0^{\infty} r^2 I dA}{\int_0^{\infty} I dA} \right)^{\frac{1}{2}} \quad \text{Equation (1.12)}$$

where  $I(r, \theta)$  is the mode field intensity distribution.

In practice the cladding of an optical fibre is not infinite. Light in the cladding can be confined by TIR at the outer cladding-air boundary of the fibre as so-called cladding modes. To avoid this, the polymer coating of an optical fibre is usually chosen to have higher refractive index than silica. In this way the cladding modes are refracted out of the cladding avoiding any undesirable light propagating along the fibre.

When an electromagnetic wave interacts with the bound electrons of a dielectric, the response of the medium in general depends on the *optical frequency*  $\omega$ . This property, referred to as *chromatic dispersion* is manifested through the frequency dependence of the refractive index  $n(\omega)$ . Thus the propagation constant also depends on the optical frequency and its first derivative is related to the *group velocity*  $v_g$  by

$$\beta_1 = \frac{d\beta}{d\omega} = \frac{1}{v_g} \quad \text{Equation (1.15)}$$

The  $\beta_2$  represents dispersion of the group velocity and is responsible for pulse broadening. This phenomenon is known as the *group-velocity dispersion (GVD)*. Optical fibre dispersion plays a critical role in propagation of optical pulses [Buck 95, Agrawal 01]. The dispersion of an optical fibre is quantified by the parameter  $D$  that is commonly used in place of  $\beta_2$ . It is defined and related to  $\beta_2$  by

$$D = \frac{d\beta_1}{d\lambda} = -\frac{2\pi c}{\lambda^2} \beta_2 \quad \text{Equation (1.16)}$$

The dispersion parameter  $D$  is a scalar number which units are expressed in ps/nm/km. This means that if the fibre has a dispersion of 1 ps/nm/km, a laser pulse will spread by a picosecond per nanometre of the pulse spectral width and per kilometre. The wavelength at which  $D$  becomes zero is referred to as the *zero-dispersion*



wavelength ZDW ( $\lambda_{ZD}$ ) (Fig. 1.6). For wavelengths such that  $D < 0$ , the fibre is said to exhibit *normal dispersion* (ND). In the normal dispersion regime, shorter wavelengths (blue-shifted) components of an optical pulse travel slower than the longer wavelengths (red-shifted) components of the same pulse. By contrast, the opposite occurs in the *anomalous dispersion* (AD) regime in which  $D > 0$ .

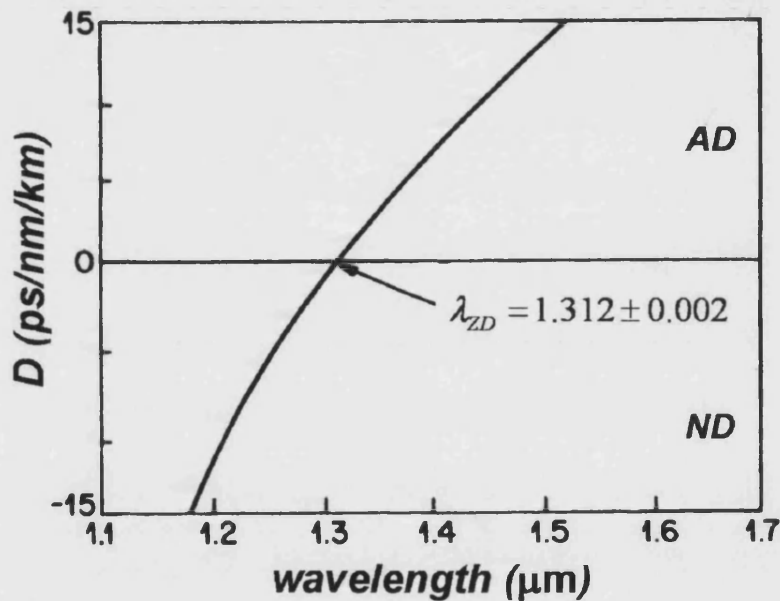


Fig. 1.6. [From Li 85] Measured variation of the dispersion parameter  $D$  with wavelength for a single-mode fibre.

### 1.3. Losses in Conventional Optical Fibres

An important fibre parameter is a measure of power loss during transmission of the optical signal inside the optical fibre. This is usually expressed in decibel units  $dB$ . The most common use of decibel scale occurs for power ratios. If a beam of power  $P_i$  is launched into one end of an optical fibre, and  $P_o$  is the power coming out at the other end, then

$$Loss = 10 \log_{10} (P_o/P_i) dB \quad \text{Equation (1.17)}$$

An important parameter of an optical fibre is the attenuation, which is the loss per unit length. A general well-known technique to measure the transmission loss is the cut back method. This consists of measuring the optical power at the output of the fibre, then cutting a length of the fibre from the end and measuring the power at that point. The process is done without changing the input coupling conditions. The attenuation is obtained by dividing the total loss by the cut length of the fibre. This technique can be applied to measure the insertion loss of connectors, splices and devices. In this case the reading of the power is taken at the output of the device (or connector/splice) and then the fibre is cut at the input of the device to measure the input optical power. This is a reliable technique to measure attenuation and insertion losses. When a fibre device is being made it is sometimes possible to measure its loss simply by monitoring the transmitted power while it is made, and dividing the initial power by the final power. Sometimes when dealing with splices, connectors or even devices, the fibres are uncoated. To eliminate the possibility of cladding modes interfering with the transmission losses measurements, index matching fluid (IMF) is often used. This IMF is a liquid (or gel) which has a similar or higher refractive index than silica. By applying this, any cladding modes propagating along the fibre are stripped out.

Several factors contribute to the loss spectrum of a conventional optical fibre, with material absorption and Rayleigh scattering dominant. Silica glass has electronic resonances in the ultraviolet (UV) region and vibrational resonances in the infrared (IR) region beyond 2  $\mu\text{m}$ , but absorbs little light in the wavelength region 0.5-2  $\mu\text{m}$  [Keck 73, Thomas 00]. However, even a relatively small amount of impurities can lead to significant absorption in that wavelength window. The most important impurity affecting fibre loss is OH, which has a fundamental vibrational absorption peak at around 2.73  $\mu\text{m}$ . The overtones of this OH-absorption peak are responsible for a dominant absorption peak near 1.4  $\mu\text{m}$  and a smaller near 1.23  $\mu\text{m}$ .

Bends in the optical fibre are another source of loss. When bending, part of the mode energy is radiated into the cladding and lost. For SMFs bending losses can be minimized by choosing the  $V$  parameter as close to the cut-off value of 2.405 at the operating wavelength as possible, so that the mode energy is mostly confined to the core.

Another significant cause of losses arises from the need to interface dissimilar fibres within the same all-fibre system, particularly fibres with different core diameters. Input coupling to small-core fibres is not easy even with bulk optics. Direct splicing of very dissimilar fibres is far from being a solution, because of difference in MFD between the fibres (Fig. 1.7). For example, a direct splice between a  $2\ \mu\text{m}$  core fibre and a  $9\ \mu\text{m}$  core fibre would give a transmission loss in excess of 10 dB. This mode mismatch is the fundamental reason for high transmission losses in the interfacing of dissimilar fibres.

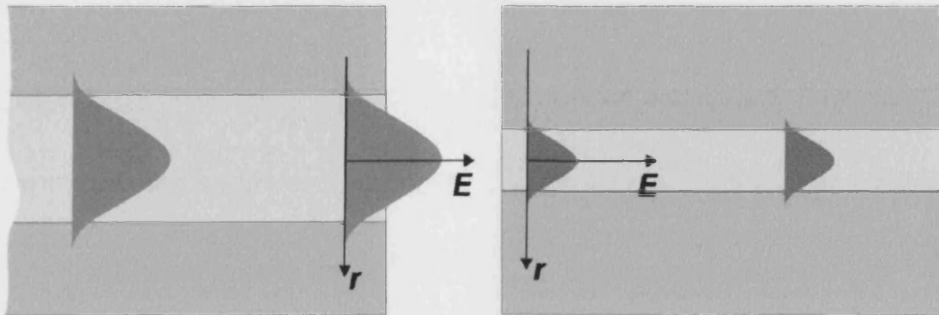


Fig. 1.7. Illustration of mode mismatch as cause for loss when interfacing between two optical fibres with very different MFDs.

---

# Chapter 2

## Photonic Crystal Fibres and Tapered Fibres

In this chapter I will describe the properties and features of photonic crystal fibres (PCFs) and tapered optical fibres. In the first two sections (Section 2.1 and 2.2) of this chapter, the fabrication processes as well as the optical guidance properties of such structures are explained. The most relevant nonlinear properties of PCFs and tapered fibres are discussed in Section 2.3.

### 2.1. Photonic Crystal Fibres (PCFs)

Photonic crystal fibre is unlike conventional fibre in that it is usually manufactured from only one material, usually pure silica. PCF has a cladding that consists of a periodic 2-dimensional array of air holes that run down the entire length of the fibre [Russell 03]. The core is formed by a “defect” that breaks the periodicity of this array. Light is confined to the core by the surrounding air holes and not by any material index differences within the glass.

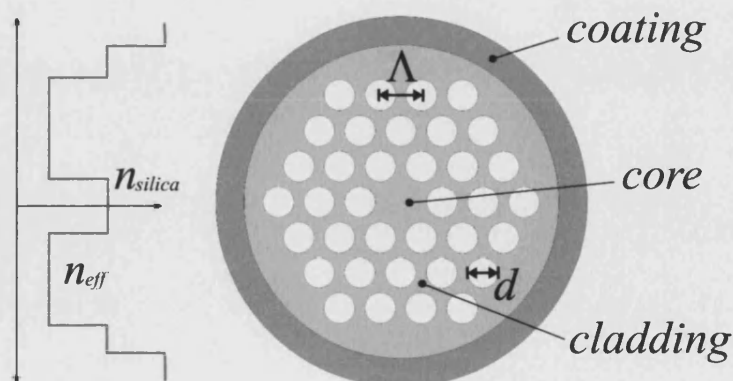


Fig. 2.1. Schematic drawing of a coated index-guiding PCF, where the white regions are air and the light grey regions are silica. The effective refractive index profile and the parameters used to define a PCF are also shown.

Unlike conventional fibre, PCF can guide light by two mechanisms. If the defect in the holey array is of high index (for example a missing air hole) the fibre can guide by total internal reflection because of the lower effective refractive index of the silica/air cladding [Knight 96]. If the defect has a lower refractive index (such as an enlarged hole) light may still be guided by being confined by a photonic bandgap in the cladding [Cregan 99]. Important design parameters for simple PCFs are therefore the hole diameter  $d$  and the centre-to-centre hole separation or pitch  $\Lambda$  (Fig. 2.1). Their ratio  $d/\Lambda$  determines the air-filling fraction of the cladding.

### 2.1.1. Fabrication Process

The fabrication process is broadly the same as for conventional fibres. Firstly a preform is made and secondly the preform is drawn to fibre. But for photonic crystal fibres the preform is made in a different way. Preform fabrication is not an MCVD process as in conventional fibres but a process of drawing and stacking capillaries (see Fig. 2.2).

In this process a silica tube several millimetres in external diameter is drawn on a fibre-drawing tower to reduce its diameter down to about 1 mm (Step 1). As result, a number of capillaries all with the same external diameter are obtained, each of which will form one unit cell of the fibre cladding. After that, the same process is followed with a solid silica rod in order to get a rod with the same diameter as the capillaries, which will act as the core (in the case of an index-guiding PCF). Capillaries that are suitably uniform are selected and stacked by hand to form a close-packed hexagonal array (Step 2). Intentional defects, such as a solid silica core or a bigger central hole, are added at this stage. The stack is placed in a silica tube (Step 3) and it is then drawn down on the drawing tower to reduce the diameter of the whole structure (Step 4). This jacketing tube is added to increase the amount of silica in the structure and increase the stability of the stack. Vacuum is applied in the region between the stack and the tube to make the interstitial holes between the capillaries collapse while preserving the inside holes of the capillaries. After this stage several preforms of about 1-2 mm in diameter are obtained. The preform may or may not be placed inside another jacketing tube (to

change the fibre's outer diameter and core size) and is drawn down to fibre (Step 5). The final diameter of the fibre normally ranges between 50 to 200  $\mu\text{m}$ . The versatility of this fabrication process allows the manufacture of many different PCF structures and devices, as will be shown in Chapters 6 and 7.

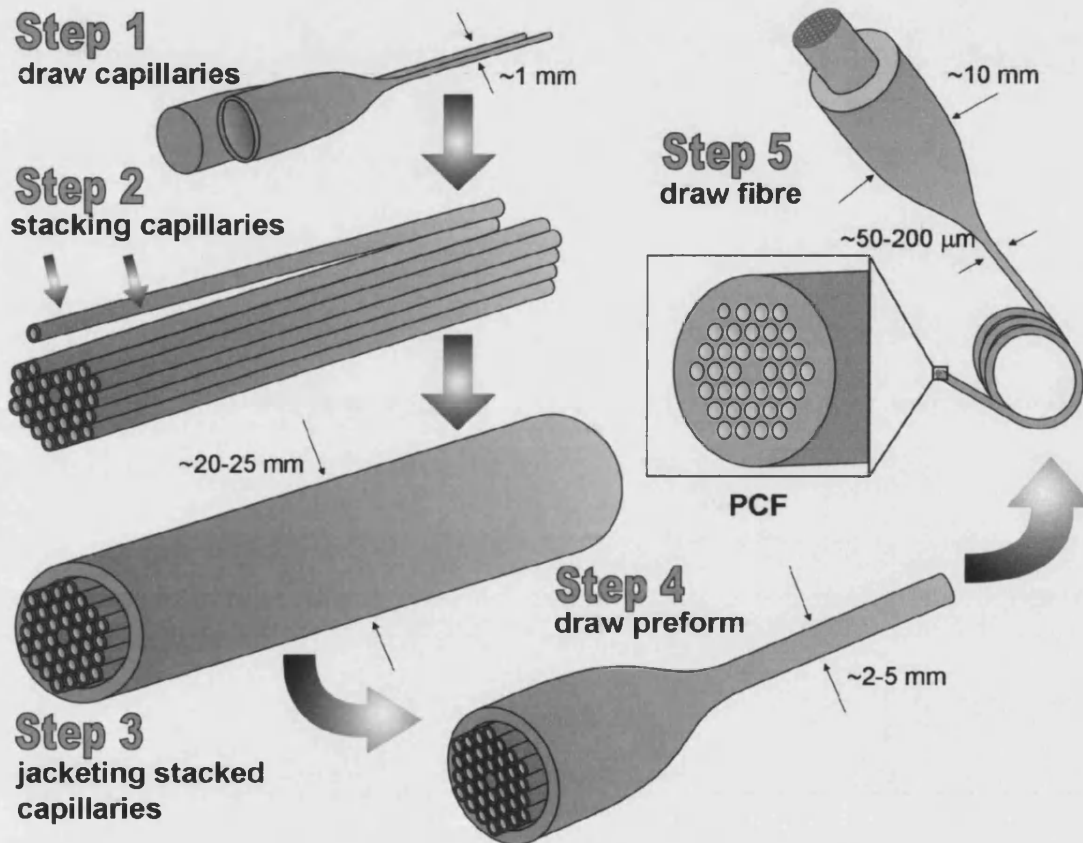


Fig. 2.2. Schematic drawing of the PCF fabrication process by the stacking and draw technique.

### 2.1.2. Index-Guiding PCFs

The high-index defect in index-guiding PCFs is formed by a pure silica core. The 2-dimensional array of holes reduces the refractive index of the cladding giving a lower *effective refractive index*  $n_{eff}$  (Fig. 2.1). Under these circumstances the light is transmitted by TIR in the same way as conventional step-index fibres. The  $V$  parameter as defined for standard fibre is not immediately suitable for PCF. However, using the “effective index” model an effective  $V$  parameter  $V_{eff}$  [Birks 97] can be defined as:

$$V_{eff} = \frac{2\pi}{\lambda} \Lambda \sqrt{n_0^2 - n_{eff}^2} \quad \text{Equation (2.1)}$$

where  $n_0$  is the refractive index of the core (i.e. silica),  $\Lambda$  is the pitch (approximately the core radius), and  $n_{eff}$  is the effective refractive index of the photonic crystal cladding defined by

$$n_{eff} = \beta_{FSM} / k \quad \text{Equation (2.2)}$$

where  $\beta_{FSM}$  is the propagation constant of the fundamental space-filling mode (FSM), which is the fundamental mode of the infinite photonic crystal cladding with the core omitted. From this definition, it can be appreciated that PCFs behave in some ways similarly to conventional fibres. However, in a PCF the cladding effective index varies with wavelength, since light can redistribute itself between air and glass. For short wavelengths this variation cancels the explicit  $\lambda$  dependence in Equation (2.1), giving  $V$  an upper bound that depends on the size of the holes. The fibre will be endlessly single-mode (i.e. single-mode at all wavelengths) if the relative hole size  $d/\Lambda$  is small enough [Birks 97]. Specifically for  $d/\Lambda < 0.4$ , the PCF is single-mode at all wavelengths [Birks 99]. Also the fibre can be single-mode even if the absolute size of the pitch is large [Knight 98].

The versatility of the PCF fabrication technique allows the manufacture of very different PCF structures as shown in Fig. 2.3. Index-guiding PCFs range from single mode fibres [Fig. 2.3 (a) and (b)] to high air-filling fraction PCFs [Fig. 2.3 (c) and (d)] which are referred to as cobweb fibres because of the shape of the holes and the thin silica strands suspending the core. Other types of index-guiding PCFs include a high numerical aperture (NA) fibre (e) and a highly birefringent polarization maintaining fibre (f).

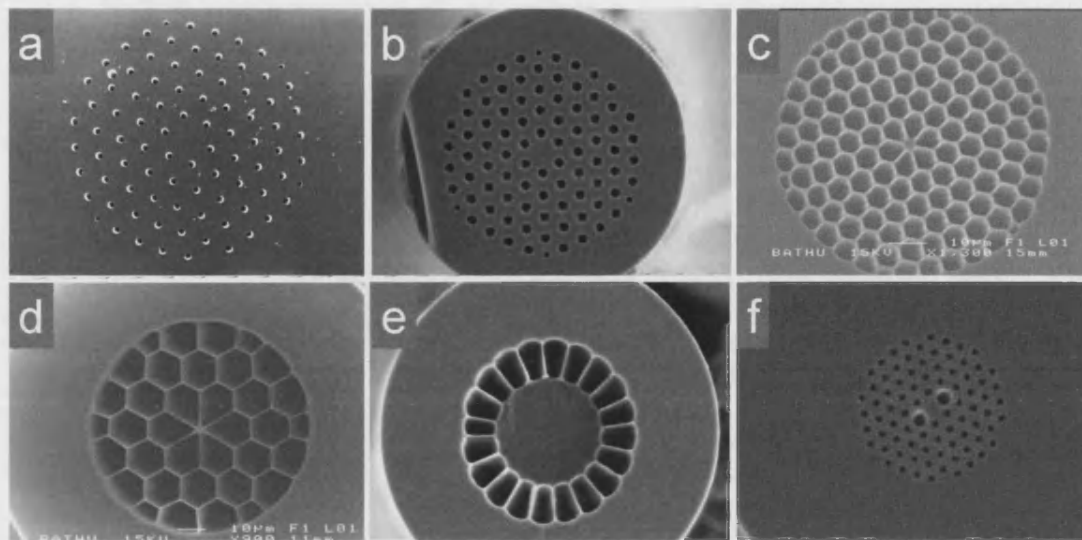


Fig. 2.3. SEM photographs of (a) and (b) single-mode PCFs; (c) and (d) cobweb PCFs with a high air-filling fraction; (e) high NA PCF; and (f) highly birefringent PCF. Fibres (a) to (d) were manufactured during the work of this PhD, fibres (e) and (f) were courtesy of Blazephotonics Ltd.

### 2.1.3. Bandgap Guiding PCFs

Hollow-core fibres are appealing, but the light in those fibres cannot be guided by TIR. In such fibres the light can be instead be guided by photonic bandgaps (PBGs). The periodicity in the refractive index of the 2-dimensional array of holes in the PCF cladding can create photonic band-gaps for out-of-plane propagation (i.e. in a direction normal to the plane of periodicity) [Birks 95b]. The presence of these band-gaps (or forbidden bands) in the values of the propagation constant in the cladding of a PCF makes it possible for light to be guided in a low-index defect acting as the core. We can see how this may happen by looking at the band-plots of a PCF cladding and a lower refractive index medium such as a hollow air-filled core (Fig. 2.4).



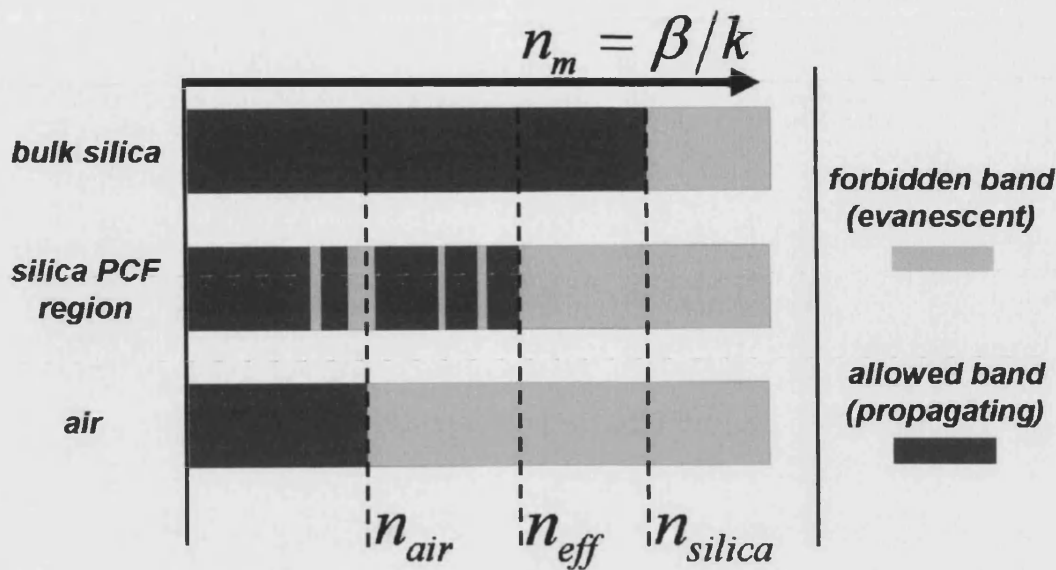


Fig. 2.4. Schematic sketch of allowed (dark grey) and forbidden ranges of modal index  $n_m = \beta/k$  in silica, air and a suitable PCF cladding ( $k$  is the free-space wave-vector).

Here, light guided in air can take any value of modal index ( $n_m = \beta/k$ ) between 0 and  $n_{air} = 1$ . The effective index of the cladding  $n_{eff}$  will always be greater than  $n_{air}$ , so TIR cannot occur. If the structure of the cladding is such that there are full 2-D bandgaps below the air-line ( $n_m < n_{air}$ ), then there can be modes that propagate in the air but which will be evanescent in the cladding. In this case the core can support modes that lie within the forbidden bands. Therefore, it is possible to fabricate a PCF with a hollow-core in which light is guided in air by means of PBG guidance. These fibres are referred to as hollow-core PCFs (HC-PCFs) [Cregan 99].

This effect is not restricted to silica and air. These types of fibres can be made from any two kinds of refractive index material that accomplish the condition in Fig. 2.4 for the forbidden bands [Luan 04].

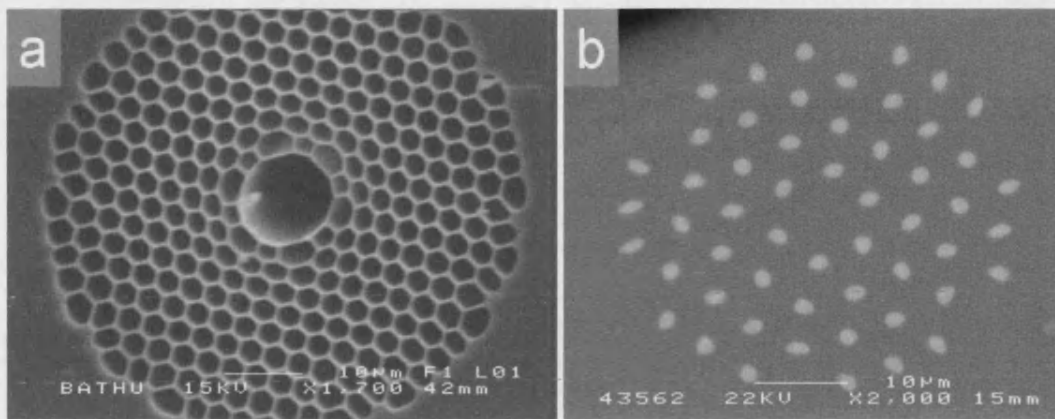


Fig. 2.5. SEM photographs of (a) air core HC-PCF (low-index inclusions) and (b) all solid silica core PBG fibre (high-index inclusions). Fibre (a) was courtesy of Blazephotonics, and fibre (b) was manufactured during this PhD and will be explained in detail in Chapter 8.

There are two types of PBG fibres, those with isolated low refractive index rods which is the case of the HC-PCF [isolated air holes within silica material Fig. 2.5(a)] and those with isolated high index rods in a lower refractive index material which also acts as the core [high index nodes within a lower background material Fig. 2.5(b)]. Such fibres with isolated high-index inclusions have been referred to as antiresonant reflecting optical waveguides (ARROWs) [White 02, Litchinitser 03]. According to the ARROW picture of guidance, the high-index nodes in the cladding allow light to leak out from the core if they are on resonance but reflect it back into the core if they are antiresonant. This is a useful simplification of the full bandgap description.

## 2.2. Tapered Optical Fibres

It is useful to make optical devices entirely from fibre. One way to do this is the tapering technique. A taper is made by stretching a heated fibre, forming a structure comprising a narrow stretched filament (see Fig. 2.6) that is called the taper waist. Each end of the taper waist is linked to unstretched fibre by a conical tapered section that is called the taper transition.

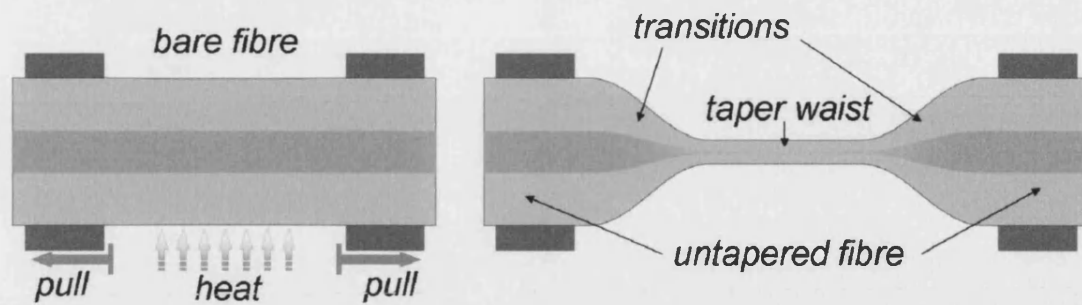


Fig. 2.6. Schematic illustration of the tapering process.

### 2.2.1. Fabrication Process

To perform the tapering process, a “taper rig” has been built and improved over many years of research. This taper rig [Fig. 2.7(a)] at the University of Bath consists of two motorized stages used to stretch the fibre and another motorized stage that moves a burner [Fig. 2.7(a) inset] that supports an oxy-butane flame. The motion of those stages is controlled by a PC. The flame is moved to and fro along the fibre as a “flame brush”, as shown schematically in Fig. 2.7(b), producing waists of uniform and predictable diameter whilst stretching the fibre at constant speed [Bilodeau 88].

In our variant the travel distance of the flame changes as tapering proceeds, giving control of waist length independently of transition length and shape [Birks 92]. Otherwise, long waists would have impracticably long transitions. Other advantages of this technique are the achievement of uniform taper waists and also the predictability of the shape of the transitions as well as the diameter of the waist [Birks 92]. (The predictability of the taper waist diameter will be discussed in more detail in Chapter 4.) Also because of this travelling flame technique the fabrication of tapered fibres is not sensitive to the nature of the flame. The addition of a CO<sub>2</sub> laser to our taper rig makes it possible to form tapered fibres without the use of a flame. Unlike the flame, however, the laser beam heats the fibre to different temperatures as the fibre changes diameter, so it is necessary to vary the laser power as tapering proceeds [Dimmick 99]. The laser beam really comes into its own as a tool for imposing sub-millimetre scale structure along taper waists, thus complementing the flame which is the better tool for forming uniform taper waists.

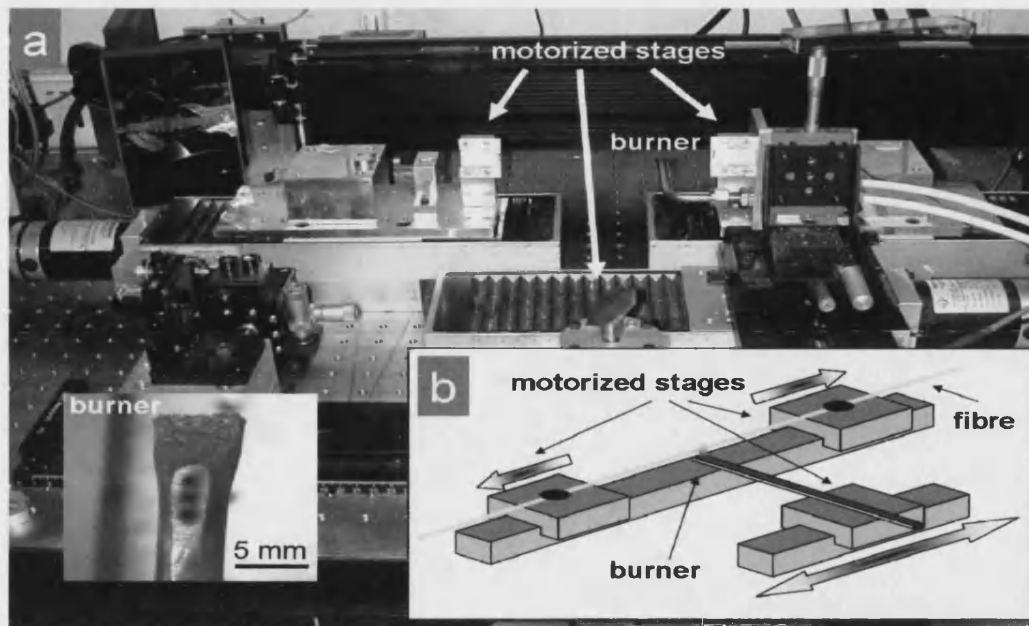


Fig. 2.7. (a) Photograph of the taper rig at the University of Bath, (inset) metallic burner used to produce the tapering flame. (b) Schematic drawing of the flame brush technique used for tapering.

### 2.2.2. Optical Properties

Optically, the taper transitions transform the local fundamental mode from a core mode to a cladding mode in the taper waist (see Fig. 2.8). If the taper transition is gradual enough there is negligible mode coupling from the fundamental mode to high order modes along the transition, resulting in a low loss tapered fibre. In the other hand if the transition is abrupt, the fundamental mode propagating along the untapered fibre couples to high order cladding modes at the taper waist that will remain cladding modes of the untapered fibre at the output. Those modes will be absorbed by the polymer fibre coating and not transmitted to the output of the fibre, making the taper lossy. So for this transformation to be accompanied by little loss of light from the fundamental mode, the shape of the taper transitions must be gradual enough to satisfy a criterion for adiabaticity at every point [Stewart 85, Love 86, Burns 86, Love 87]. This is a condition on the length scale of the transitions and the taper

angles. By using our taper rig with ordinary fibres such as SMF-28, tapered fibres of up to 13-14 cm waist length with around 1 cm transitions can be achieved with total transmission losses of less than 0.1 dB in a straightforward manner.

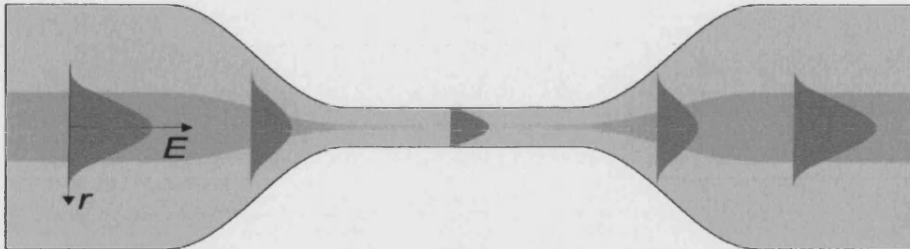


Fig. 2.8. Illustration of the behaviour of the light in a taper. The fundamental mode in the core spreads out as it narrows until it is guided by the outer boundary in the taper waist.

In the taper waist the core is too small to guide light. Light is guided by total internal reflection at the cladding-air outer boundary. In this way the evanescent field of the guided mode is propagating through the air. This property of tapered conventional fibres allows the interaction of the light in the evanescent field with different materials, such as liquids, that can be placed surrounding the taper waist [Cordeiro 05]. This situation can be used for the fabrication of several devices. In Chapter 3 I will explore this property of tapered fibres by using sol-gel materials.

### 2.2.3. Tapered PCFs

Tapering a conventional fibre preserves its refractive index distribution, which simply scales with diameter. This technique cannot be applied to PCFs in a simple way. In a PCF the sizes of the air holes relative to the fibre diameter can also change, as surface tension attempts to collapse them. Hence tapering of PCFs involves two types of variation (see Figure 2.9) and in a real transition both of them will combine. This complicates the tapering of PCFs and must be controlled if low-loss taper transitions in PCF are to be achieved. On the other hand, the extra degree of freedom of collapsing

the holes can be used for many applications [Kakarantzas 01, Kakarantzas 02]. Some applications because of changes in hole size are studied and exploited in Chapter 5.

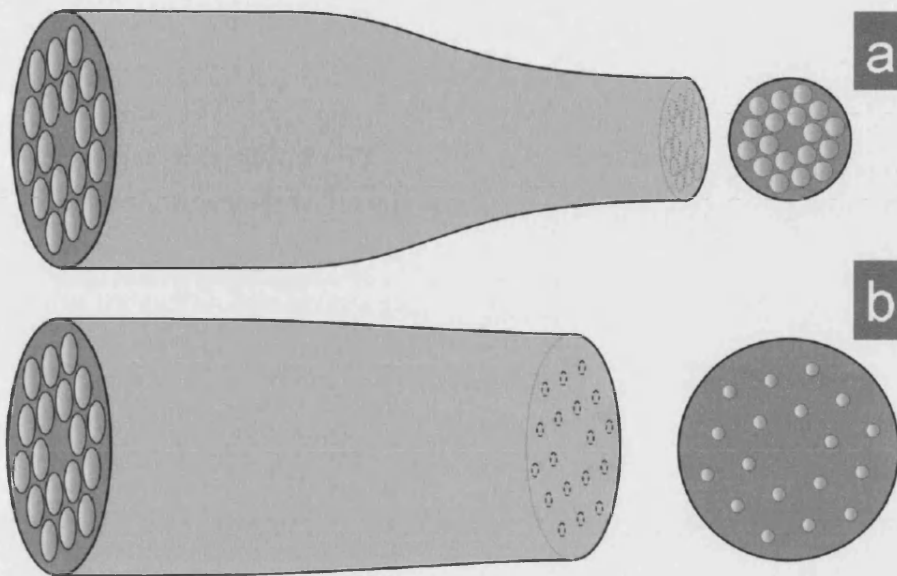


Fig. 2.9. Degrees of freedom when tapering PCFs; (a) Stretching: reduce cross-section, constant  $d/\Lambda$ ; (b) Hole collapse: change  $d/\Lambda$ , approximately constant cross-section.

### 2.3. Nonlinear Optics in Optical Fibres

In any dielectric material, such as silica used in optical fibres, the response of light becomes nonlinear for intense electromagnetic field. The structure of silica glass effectively has inversion symmetry, so the second-order susceptibility  $\chi^{(2)}$  vanishes [Shen 84]. As a result, optical fibres do not normally exhibit second-order nonlinear effects. The lowest-order nonlinear effects in optical fibres come from the third-order susceptibility  $\chi^{(3)}$ , which is responsible for different phenomena such as third-harmonic generation, four-wave mixing and nonlinear refraction [Shen 84].

### 2.3.1. Nonlinear Refractive Index

The third-order nonlinearity  $\chi^{(3)}$  is manifested as an increase of refractive index  $n$  with the intensity  $I$  of the light propagating through the medium:

$$n = n_0 + n_2 I \quad \text{Equation (2.3)}$$

where  $n_2$  is the so-called nonlinear refractive index of the medium and  $n_0$  is the ordinary linear refractive index. Measurements of  $n_2$  for silica yield a value  $n_2 = 2.7 \times 10^{-20} \text{ m}^2 / \text{W}$  at the 1.06  $\mu\text{m}$  wavelength [Milam 76].

The intensity dependence of the refractive index leads to a number of nonlinear effects such as self-phase modulation (SPM) and four wave mixing (FWM). SPM refers to the self-induced phase shift experienced by an optical field during its propagation in optical fibres [Agrawal 01].

### 2.3.2. Four-Wave Mixing

In the nonlinear process of phasematched degenerate FWM, pump light of one frequency can generate new frequencies which are called sidebands. These sidebands are spaced at equal frequency intervals from the pump and they are referred to as the signal (higher frequency) and idler (lower frequency) [Coen 01, Dudley 02a, Reeves 03, Wadsworth 04a]. Gain for these processes is provided by the nonlinear index of silica  $n_2$ . Phase matching (conservation of momentum) and conservation of energy give the equations [Agrawal 01]

$$2k_{\text{pump}} = k_{\text{signal}} + k_{\text{idler}} + 2\gamma P \quad \text{Equation (2.4)}$$

and

$$2\omega_{\text{pump}} = \omega_{\text{signal}} + \omega_{\text{idler}} \quad \text{Equation (2.5)}$$

where  $k$  are the wave vectors (propagation constants) and  $\omega$  the frequencies of the pump, signal and idler waves.  $P$  is the pump power (in the quasi-CW case the peak pump power) and  $\gamma$  is the nonlinear coefficient of the fibre,

$$\gamma = \frac{2\pi n_2}{\lambda A_{eff}} \quad \text{Equation (2.6)}$$

where  $\lambda$  is the pump wavelength and  $A_{eff}$  is a nonlinear parameter known as the effective core area, which is defined as [Agrawal 01]:

$$A_{eff} = \frac{\left( \int \int_{-\infty}^{\infty} |F(x, y)|^2 dx dy \right)^2}{\int \int_{-\infty}^{\infty} |F(x, y)|^4 dx dy} \quad \text{Equation (2.7)}$$

Its evaluation requires the use of modal field distribution  $F(x, y)$  for the mode propagating along the fibre. Clearly  $A_{eff}$  depends on fibre parameters such as the core size and the core-cladding index difference.

These phasematching conditions specify the wavelengths for peak gain in a given fibre, and will depend on the chromatic dispersion of the fibre.

### 2.3.3. Supercontinuum (SC) Generation in PCF and Tapered Fibres

Supercontinuum generation refers to the nonlinear broadening of a relatively narrow spectral bandwidth of a laser into a broad bandwidth, typically spanning an optical octave or more (from a certain wavelength to twice that wavelength). The process of SC generation has been known for many years. The majority of experiments in SC generation in PCFs and tapered fibres have focused on the ultra-short pulse regime, with femtosecond pulses from modelocked lasers [Ranka 00, Birks 00, Wadsworth 02, Teipel 03]. In that case, SPM, soliton effects and pulse walk-off are important considerations, and the propagation is described by the generalised nonlinear Schrödinger equation [Ortigosa-Blanch 02, Dudley 02b]. However, much longer pulses, such as ns pulses, can be considered as quasi-CW. In this case the major



nonlinear process is phasematched FWM. Nevertheless, in both short and long pulse regime, the key parameter for an efficient broad SC generation is the dispersion of the fibre.

Optimising dispersion relaxes the need for high intensity, allowing SC generation for larger cores and/or longer pulses [Coen 01]. This approach is particularly effective for the wavelengths of Nd lasers (eg 1064 nm for Nd:YAG) where material dispersion is not large, giving greater scope for modifying waveguide dispersion to tailor net dispersion. Hence single-mode SC can be generated from the ns pulses of a Q-switched Nd:YAG microchip laser (a compact and low-cost source) in 20 m of PCF with a core diameter as big as 5  $\mu\text{m}$  [Wadsworth 04a].

A PCF with large air holes and a small silica core is physically similar to a strand of silica surrounded by air, i.e. a tapered conventional fibre. The tapered fibre and the core of the PCF concentrate light into a small nonlinear effective area while dramatically modifying the dispersion characteristics. The dispersion of such PCFs has been shown to be similar to that of tapered fibres of similar diameter [Wadsworth 02].

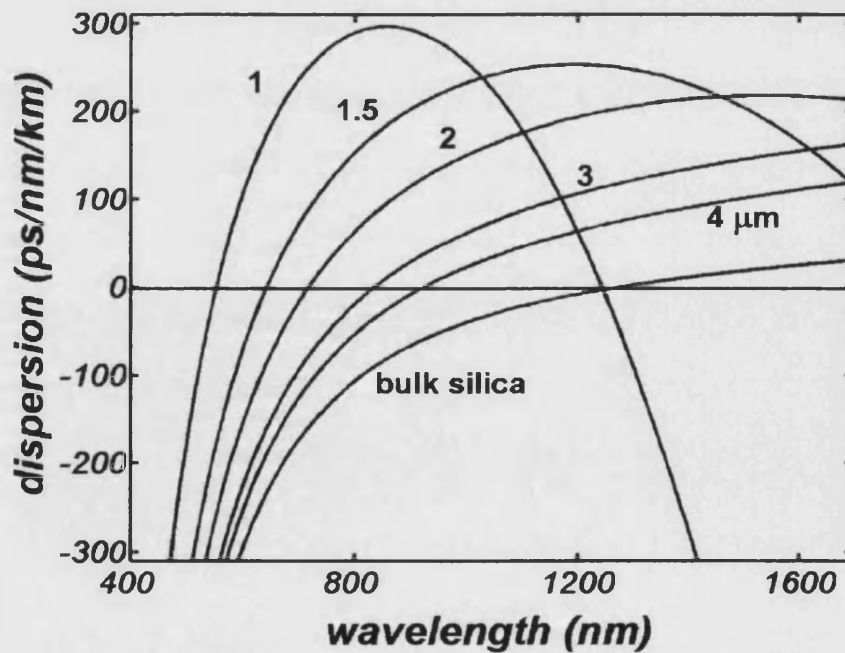


Fig. 2.10. Evolution of the calculated dispersion spectra of taper waists (a strand of silica surrounded by air) as the diameter (labelled) decreases, together with the dispersion of the bulk silica material.

The dramatic shift in the zero dispersion wavelength  $\lambda_{ZD}$  to shorter wavelengths in small taper diameters are shown in Fig. 2.10. The peculiar dispersion properties of small solid-silica core PCFs and tapered fibres makes them ideal waveguides for several nonlinear processes. The nonlinear process of SC generation in PCFs and tapered fibres will be studied and explored in Chapters 4 and 5.

---

# Chapter 3

## Sol-Gel, Aerogel and Tapered Conventional Fibres

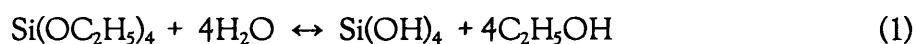
A process that has gained importance in the glass and ceramic fields is the sol-gel reaction. This chemistry produces a variety of inorganic networks from silicon or metal alkoxide monomer precursors. Although first discovered in the late 1800s and extensively studied since the early 1930s, a renewed interest surfaced in the early 1990s [Brinker 90, Hench 90] when monolithic inorganic gels were formed at low temperatures and converted to glasses without a high temperature melting process

The sol-gel method has proved to be an excellent method for the preparation of optical coatings and bulk materials. The sol-gel process is based on the hydrolysis of an alkoxy silane to form a gel, which is an open porous silica network filled with a solvent. The sol can then be dried to expel the solvent, leaving a dry porous glass. The porosity of the glass depends on the drying process. In this chapter I describe the deposition of sol-gel-derived silica around tapered fibres. In Section 3.1, the glass is applied in thin layers of low porosity. In Section 3.2, the taper is embedded in a large block of silica aerogel, which is a highly porous glass.

### 3.1. Sol-Gel Coating of Tapered Fibres

In this section I describe the deposition of thin coatings of sol-gel-derived silica onto tapered fibres. Being porous, the coating has a slightly lower refractive index than the tapered fibre, so the light in the fibre can interact with it via the evanescent field. A CO<sub>2</sub> laser beam was used to periodically change the porosity of the coating and so form a long period grating [Kakarantzas 04].

The sol-gel process, as the name implies, involves the formation of inorganic networks through the formation of a colloidal suspension (sol) and gelation of the sol to form a network in a continuous liquid phase (gel). Most widely used precursors are tetramethoxysilane (TMOS), tetraethoxysilane (TEOS) and polyethoxydisiloxane (PEDS). The reaction for TEOS is described by equations (1) and (2):



This description is too simplified and it omits many factors. Water and TEOS are immiscible, and they require adding alcohol to form a solution. Ethanol (EtOH) is the most commonly reported solvent for sol-gel work using TEOS. The influence of the solvent is important not only because it can take part in the reverse of reactions (1) and (2) but also because its removal during drying largely determines the final morphology and porosity. Although hydrolysis and condensation can occur without addition of an external catalyst, this is usually employed. The rate and extent of the hydrolysis reaction is most influenced by the strength and concentration of the acid or base catalyst. Mineral acids (HCl) and ammonia are most generally used, however other catalysts are acetic acid, KOH, amines, KF, and HF [Brinker 90]. Changing the catalyst can have a large influence on the microstructure of the gels formed as well as on the rate of the gelation process. The pH under which the sol-gel process is carried out determines the gelation time and the pore size [Hoang 97].

From all the above it is clear that the characteristics and properties of a particular sol-gel inorganic network are related to a number of factors that affect the rate of hydrolysis and condensation reactions, such as pH, temperature and time of reaction, reagent concentrations, catalyst nature and concentration,  $\text{H}_2\text{O}/\text{Si}$  molar ratio, aging temperature and time, and drying [Prassas 84]. Of the factors listed above, pH, nature and concentration of catalyst, and  $\text{H}_2\text{O}/\text{Si}$  molar ratio are the most important.

### 3.1.1. Sol Preparation

Sol was made inside a fume cupboard with a low constant airflow in order to keep a clean environment. The precursor for synthesizing sol-gel was TEOS with 98% purity. The sol was prepared under acidic conditions, choosing hydrochloric acid (HCl) as a catalyst. De-ionized water with a pH of 7 is employed to make the acidified water for the solution. The solvent used to help the miscibility of the solution is ethanol (EtOH) with 99.99% purity. The sol mixture is stirred at room temperature on a magnetic stirring plate controlling the stirring speed and time.

As mentioned before, the sol-gel process depends on many factors that can influence the final structure. In order to simplify the procedure some of these parameters were fixed. Following a number of references for optical coatings (eg. [Brinker 90]), the TEOS/EtOH/acidified water ratio was kept constant at 1:4:2 molar ratio respectively. The composition used for this experiment was 0.125 moles of TEOS, 0.5 moles of EtOH and 0.25 moles of acidified water. For optical coatings, an important factor to control is the porosity, which determines the refractive index of the layer. The most important parameter driving the porosity is the pH of the sol-gel mixture. Therefore a range of pH values for the acidified water was tried. The mixtures were stirred at 350 r.p.m for two and a half hours at room temperature. It was found to be important to put a lid on the beaker during the stirring process. This reduces the evaporation rate of the alcohol in the mixture while stirring. Without a lid, at least  $\frac{1}{4}$  of the mixture was evaporated after the stirring. On the other hand, with the lid on, this amount is reduced drastically.

### 3.1.2. Coating Technique

Of the many wet-coating methods available, dip coating has the capability of laying down very thin layers of precise thickness [Landau 42]. The substrate is immersed in a liquid and then withdrawn at a well-defined speed under controlled temperature and atmospheric conditions. The coating thickness is mainly defined by the withdrawal speed. Thin layers of sol were deposited onto tapered fibres by a modified dip coating

method, in which a droplet of sol suspended at the tip of a syringe needle was repeatedly passed along the fibre (Fig. 3.1).

After the sol was prepared it was passed through a filter of  $0.2\ \mu\text{m}$  hole size into a syringe for the final deposition. The filtering was to eliminate contamination as well as any big particles of gel that have already formed. The syringe was on a XYZ stage driven by a translation motor of the taper rig as shown in Fig. 3.1. The main factors influencing the thickness of the layer were the motor speed and the number of reversals. A few reversals of the translation motor driving the syringe needle were enough at the chosen fixed speed of  $600\ \text{mm/minute}$ .

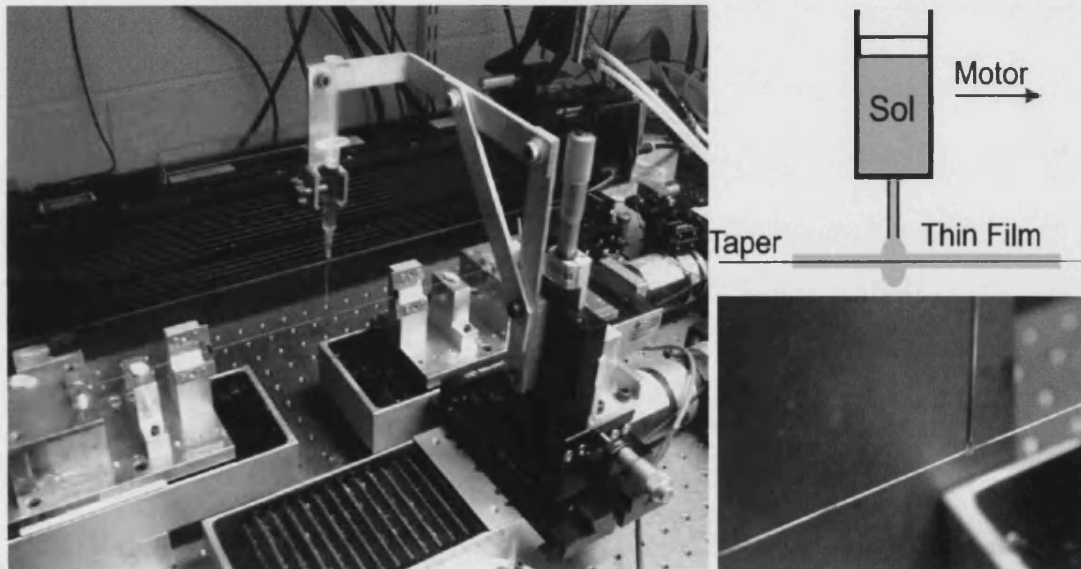


Fig. 3.1. Modified dip coating setup.

The size of the droplet was controlled by a screw attached to the syringe holder acting as a compressing mechanism, to move the droplet out or in by tightening or releasing the screw. The droplet was released from the syringe when the translation motor was already moving, and was withdrawn before the translation motor stopped at the end of the process. With this procedure the layer deposited was more likely to be uniform.

A few seconds after the substrate had emerged from the droplet, the sol started to gel and dry in contact with the air. The result was a thin film comprising many layers of porous silica, which then require heat treatment for densification of the layer.

### 3.1.3. Laser Densification of Porous Films on Tapered Fibres

Densification of sol-gel is normally accomplished in a furnace but absorbed laser irradiation provides an alternative method of heating [Schmidt 90, Keddie 91]. The sol-gel refractive index varies with the temperature of densification in different ways for laser and furnace firing as shown in Fig. 3.2. These differences are due to the speed of the process. In the furnace, heating and cooling take place for much longer. However laser heating gives the potential of a localized heat-treatment and fast heating and cooling of the material.

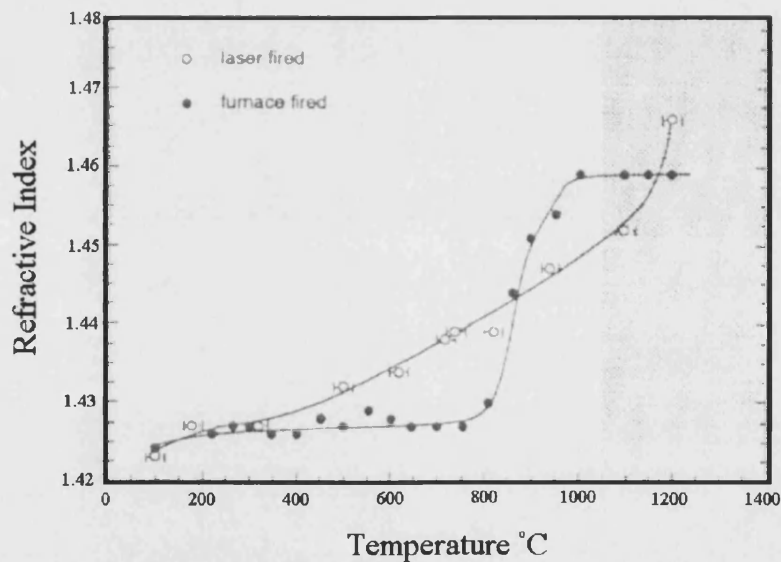


Fig. 3.2. [From Taylor 92] Change in refractive index of laser-densified (open circles) and furnace-fired (closed circles) TEOS coatings.

For the densification a CW CO<sub>2</sub> laser beam with a 600 μm spot size was directed with a galvanometer mirror that was driven by a computer and focused with a 300mm

focal length lens onto the taper waist of the fibre to be coated and heat-treated. The CO<sub>2</sub> laser beam was redirected anywhere along a certain length of the taper waist by scanning the galvanometer mirror. This set-up is shown in Fig. 3.3. This versatile experimental set-up was able to produce a very fast scanning laser beam along the taper waist for a certain period of time. The entire process is controlled by a computer, to control: (a) the laser power with an attenuator and a shutter, and (b) the motion of the scanning mirror controlling the beam.

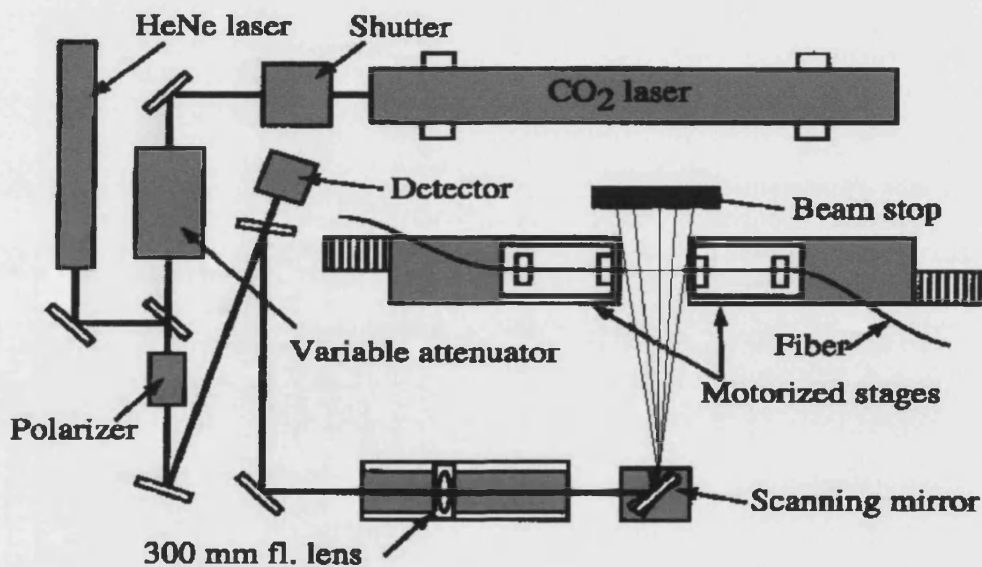


Fig. 3.3. Schematic CO<sub>2</sub> laser rig set-up.

The tapers used for this experiment were 40 mm long and 10  $\mu\text{m}$  diameter in the taper waist. The background losses of the tapers were less than 0.1 dB. The transmission spectra of the coated tapers as well as the background losses were recorded in real time. Different pH sols were used for the experiment. It was found that the sols with pH concentrations from 2.30 to 2.40 were the optimum values for depositing low-loss thin layers. With a pH 2.31 sol, losses of 0.1 dB for a single coating and 0.3 dB for three successive coatings on the same taper waist were achieved.



Having established the conditions for low-loss deposition, patterning of the layer were demonstrated by using the CO<sub>2</sub> laser as a localized heat source. Different zones along the fibre can be given different properties based on different laser-firing conditions onto the coating. By heating a local section of the coating for a longer time, an increase in the index of refraction of that particular zone is achieved because the porosity is reduced. A periodic pause as the beam is scanned along the taper waist gives a periodic perturbation on the coating that behaves as a long period grating (LPG).

In LPGs light typically couples from the fundamental core mode to discrete, forward-propagating cladding modes. The cladding modes are quickly attenuated and this results in series of loss bands in the transmission spectrum of the grating [Kayshap 99]. This coupling is caused by a periodic variation in refractive index along the fibre. Typically, in a single mode fibre a LPG couples the core mode to a co-propagating cladding mode at the coupling (or resonance) wavelength where

$$\beta_1 - \beta_2 = \frac{2\pi}{\Lambda} \quad \text{Equation (3.1)}$$

$\beta_1$  and  $\beta_2$  are the propagation constants of the two modes and  $\Lambda$  is the period of the grating. The exact forms of the spectrum, and the centre wavelengths of the attenuations bands, are sensitive to the period of the LPG, the length of the LPG and to the local environment: temperature, strain, bend radius and the refractive index of the medium surrounding the fibre. The procedure for making LPGs was the same as for making uniform coatings but now the scanning laser beam was set to pause for a few milliseconds at certain points to create the periodic perturbation. The stopping times as well as the period were controlled by the computer.

The fact that the transmission was observed in real time made it possible to increase the grating notch with consecutive sweeps of the laser until reaching the maximum coupling efficiency, before saturation and signs of over-coupling appeared. Typical parameters were 6 to 10 scans with stopping times from 60 to 350 milliseconds, keeping the laser power steady. Parameters for three different LPGs are shown in Table

3.1 and the LPG spectral responses for these gratings are shown in Fig. 3.4. Background losses of the gratings (away from the resonance wavelength) were less than 0.2 dB.

Table 3.1: Parameters of the three different fabricated LPGs.

LPGs	$\Lambda(\mu\text{m})$	periods	Sol pH	Dip coating layers	Laser power (W)
A	500	50	2.36	9	3.8
B	450	50	2.23	6	5.1
C	400	60	2.31	9	4.0

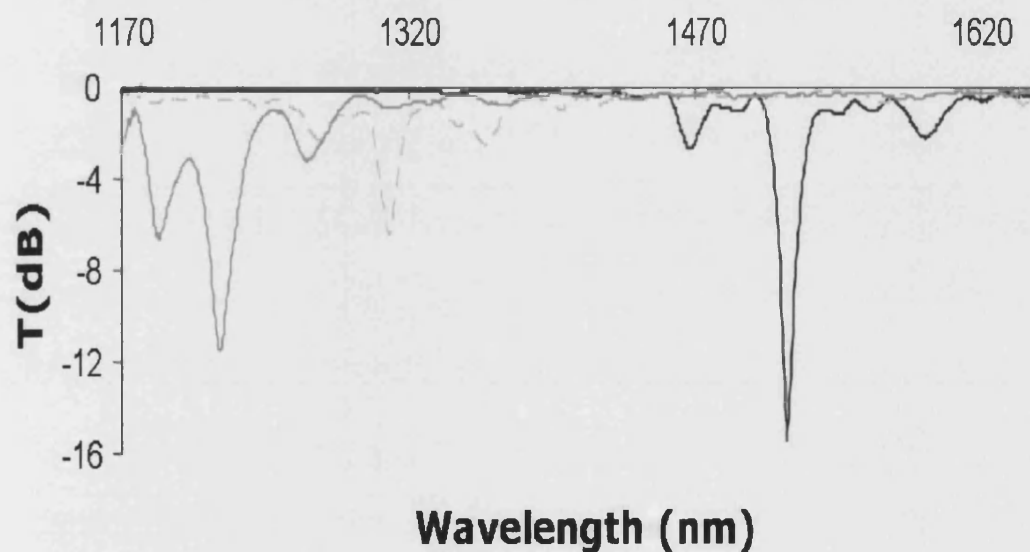


Fig. 3.4. Transmission spectra of (light grey solid line) LPG A, (light grey dashed line) LPG B, and (dark grey solid line) LPG C.

Once formed, a LPG could be erased by uniform exposure of the laser beam at higher power, completely consolidating the film. Using the flexibility of the experimental set-up a LPG could be erased in separate stages. Periods of the grating were erased by different scans, reducing gradually the number of periods until none was left. At this point the deposited film was fully consolidated, effectively giving an

ordinary taper waist of slightly greater diameter. The results of this experiment are shown in Fig. 3.5 for a LPG with 60 periods of 400  $\mu\text{m}$ . (A sol of pH 2.31 was used, deposited over 7 reversals. The LPG was formed by 8 scans of the laser at 4 W.) The losses for erased gratings were found to be less than 0.1 dB in some cases. As expected [Erdogan 97], the reduction in the grating length had a direct effect on the coupling constant and the bandwidth of the resonance.

After the first LPG is made it is erased and the sol-gel coating process is repeated on top. Then this one was erased and another LPG was written on top and this process is repeated three times for the same taper waist as shown in Fig. 3.6.

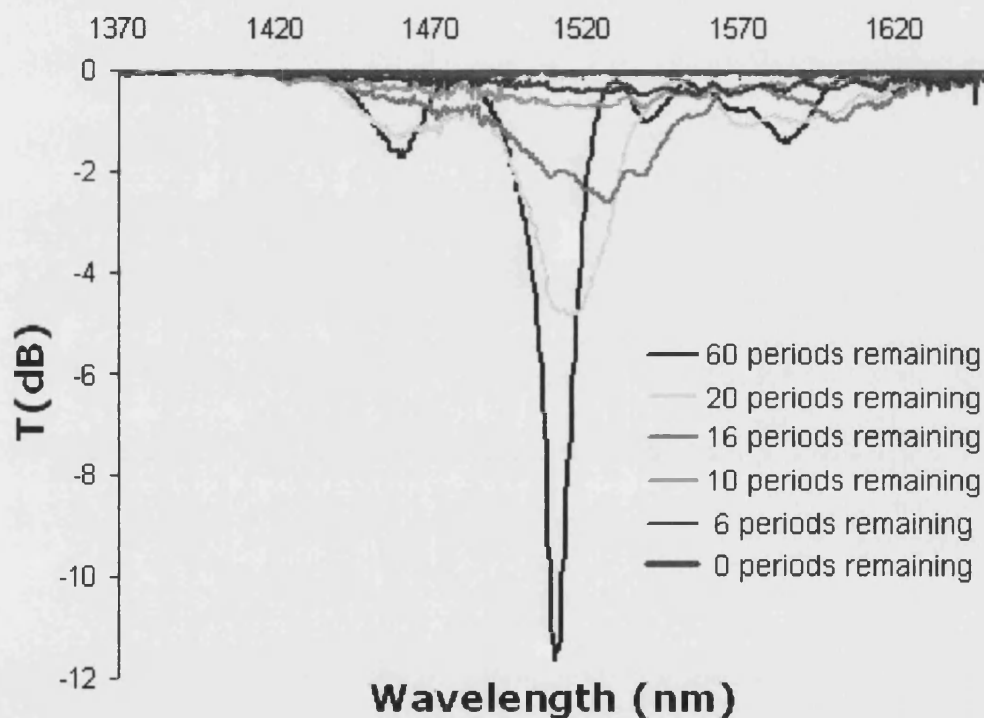


Fig. 3.5. Transmission spectra of sol-gel LPG with number of periods erased in successive scans of the  $\text{CO}_2$  laser beam until the grating pattern is totally erased.

The same number of syringe reversals, 9 reversals, was used to deposit the first two sol-gel coatings for the first two LPGs. The third layer was made by 7 reversals. The first two LPGs had a very similar spectral shape and strength, showing stronger coupling

than the last one made with a thinner layer. The shift in wavelength was due to the difference in diameter of the taper waist. This difference in diameter was due to the thickness of the sol-gel coating and can be deduced from the wavelength shift.

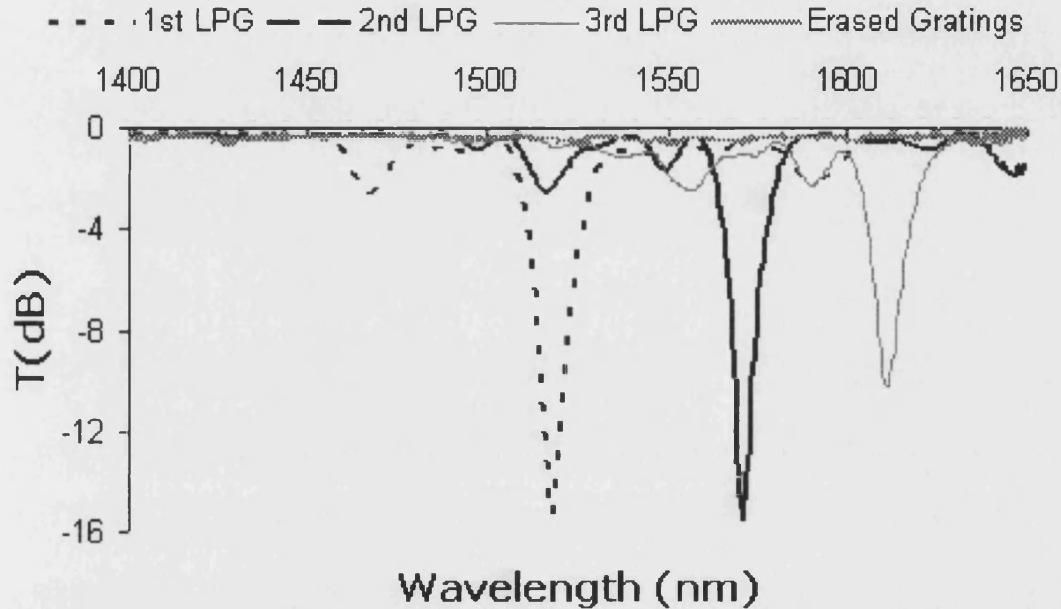


Fig. 3.6. Transmission spectra of three different LPGs written and erased on top of each other in the same taper waist. Final erasure of the third LPG leaves a background loss of less than 0.4 dB.

The normalised parameter  $U$  is defined by [Snyder 83]

$$U = a\sqrt{(k^2 n_{co}^2 - \beta^2)} \quad \text{Equation (3.2)}$$

where  $k = 2\pi/\lambda$ ,  $a$  is the core radius and  $\beta$  is the propagation constant. If the core is large compared to the wavelength then

$$\beta \approx kn_{co} - \frac{U^2}{2kn_{co}a^2} \quad \text{Equation (3.3)}$$

Hence Equation (3.1) relates the LPG period  $\Lambda$  to the  $u$  values for the 2 modes through

$$\Lambda = \frac{2\pi}{(\beta_1 - \beta_2)} \approx \frac{(8\pi n_{co} a^2)}{(U_2^2 - U_1^2)\lambda} = \text{constant} \quad \text{Equation (3.4)}$$

since  $(U_2^2 - U_1^2)$  remains more or less constant (since both modes are far from cut-off [Snyder 83])

$$\frac{a_1^2}{\lambda_1} = \frac{a_2^2}{\lambda_2} \quad \text{Equation (3.5)}$$

which specifies the change in radius (and hence the larger thickness) that a certain shift of coupling wavelength. Experimentally the coupling wavelengths for the 1<sup>st</sup>, 2<sup>nd</sup> and 3<sup>rd</sup> LPGs were 1518 nm, 1570.8 nm and 1611.6 nm respectively. For a taper diameter of 10  $\mu\text{m}$ , the thickness of the coatings were therefore 0.1 - 0.15  $\mu\text{m}$  for the first two coatings and 0.07 - 0.09  $\mu\text{m}$  for the third coating. The thickness of the coatings is close to linearly proportional to the number of reversals during the coating process.

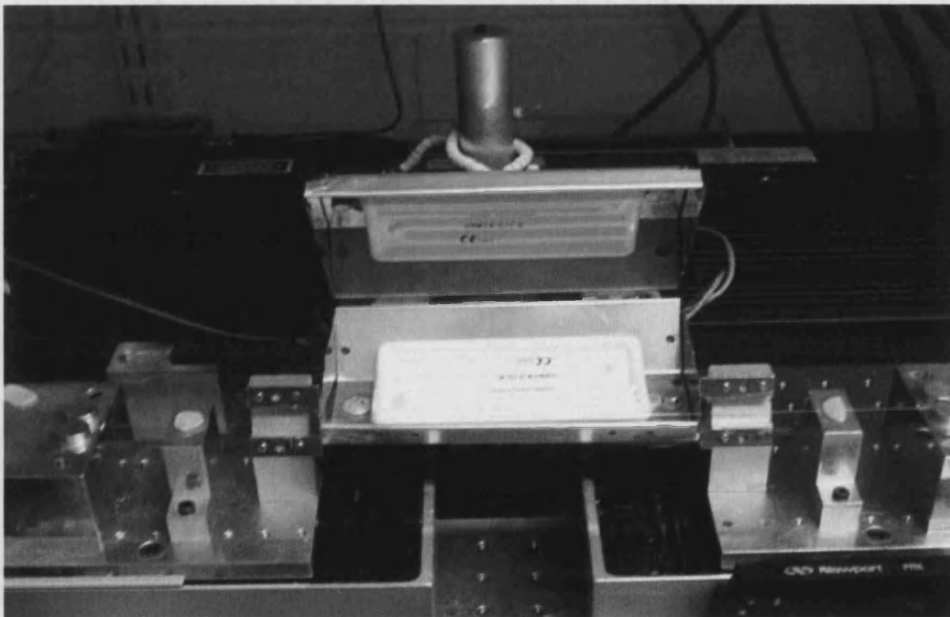


Fig. 3.7. Removable furnace integrated into the taper rig.

In order to test the thermal stability of the sol-gel LPGs, changes in the transmission spectrum were measured from room temperature to 900 °C in real time, using a “homemade” furnace (see Fig. 3.7) fabricated and integrated as a removable part of the taper rig.

A LPG of 60 periods of 400  $\mu\text{m}$  was made, with a pH 2.33 solution, 7 reversals and ten scans at 4 W laser power, for this experiment. The LPG was heated up to 890 °C in about one hour and then it was left to cool down for another hour. The transmission spectrum of the LPG was observed in real time. The resonance wavelength of the LPG is plotted as a function of the temperature in Fig. 3.8. The response from room temperature to 450 °C had a slope of 10 pm/°C and from 450 °C to 890 °C it had a slope of 21.5 pm/°C. Above 800 °C the depth of the notch in the LPG started to decrease, indicating that the film was starting to consolidate, but there was still 90% (-10dB) coupling at 900 °C. This behaviour agrees with the Fig. 3.2 giving by Taylor et al [Taylor 92].

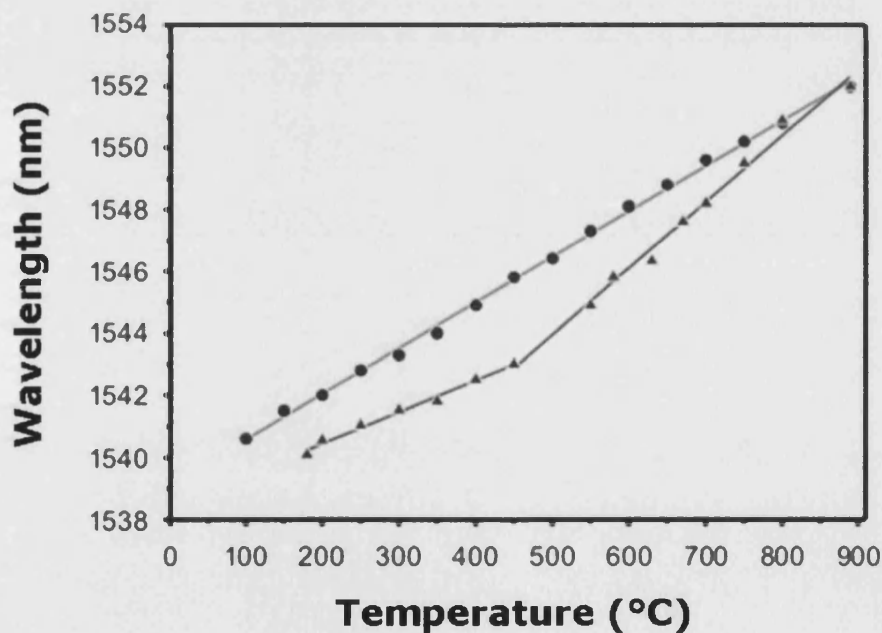


Fig. 3.8. Variation of coupling wavelength with temperature: (solid triangles) with increasing temperature; (closed circles) with decreasing temperature.

The annealing suffered during the heating process stabilizes the layer and the LPG response when the grating was cooling down was almost a perfect line with a slope of 15 pm/°C. By known values of the coefficient of linear expansion and the temperature dependence of the index of fused silica [Bansal 86, Ghosh 94], an approximate value of about 12 pm/°C is estimated (dominated simply by the temperature dependence of the index) in a good agreement with my measurements. In absolute terms this temperature sensitivity is among the lowest reported, which I attribute to the fact that the taper and the film are made from the same material and so they avoid thermally induced stress.

### 3.2. Tapered Fibres Embedded in Aerogel

Aerogels are a class of ceramic materials fabricated from a sol-gel by carefully evacuating the solvent to leave a porous submicron scale polymer network which is 90-99% air by volume [Pajonk 98, Pierre 02]. The first aerogels were produced in the late 1920s by Samuel Kistler, who found a way to remove the fluid from a wet silica gel, leaving behind its solid structure. In the early 1930s, Kistler continued his experiments with aerogels, studying some of their thermal and catalytic properties. Interest in aerogels was renewed in the 1980s.

The hollow pores and solid particles within the aerogel have dimensions that are small compared to the wavelengths of visible and IR light, so it behaves optically as a homogeneous medium (albeit with enhanced Rayleigh scattering). These remarkable materials are reported to have nonlinear indices  $n_2$  five orders of magnitude greater than that of solid silica [Seo 03]. There has been little work on the applications of aerogels within fibre optics. Some patents refer to its use as a low-index cladding to provide a high numerical aperture in multimode fibres [Sprehn 98]; this work does not appear to have been published in the scientific literature, and in any case has not had much impact. Blocks of aerogel have been used as a rigid low-index substrate to support submicron tapered fibres [Tong 05], but the fibres were simply laid onto the aerogel rather than being embedded within it.

### 3.2.1. Synthesis of Aerogel

This work has been collaboration with Dr. L. Kuchta and Dr. K. Jesenák at Comenius University in Bratislava, and Ing. J. Doupovec at Slovak Academy of Sciences in Bratislava. The aerogel process part of the experiment was carried out in Dr. Kuchta's laboratories during a visit to Comenius University.

The monolithicity of aerogels depends strongly on the catalyst used for each precursor [Wagh 99]. The pore size distribution for TMOS aerogels was found to be narrow and uniform. These smaller pores and particles result in better optical transmission, 93% for TMOS aerogels [Wagh 99]. The shortest gelation time (convenient for the experiment) is achieved by using strong bases like KOH and ammonia [Rao 94]. The solvent chosen for this experiment is methanol. The reason for this is the choice of TMOS as precursor.

The synthesis of silica aerogel consists of 3 general processes; preparation of the gel (as described in Subsection 3.1.1), aging of the gel and drying of the gel. The gels are usually classified according to the dispersion medium used, e.g., aquagel, alcogel and aerogel (for water, alcohol, and air, respectively). Common aging procedures of the alcogel typically involve soaking the gel in alcohol to control the evaporation of the solvent. This aging process strengthens the gel, so that shrinkage during the drying step is kept to a minimum. The aging time could take up to a week.

In the drying process the liquid within the alcogel is removed, leaving only the linked silica network. This drying process is the most challenging step in the aerogel synthesis, because simple evaporation allows surface tension forces at the interfaces between liquid and vapour to collapse the porous structure. To avoid this problem the drying of the solvent is carried out under supercritical conditions. Supercritical drying goes around the phase line boundary (from liquid to gas) on the high-temperature/high-pressure side passing through the supercritical region, where the distinction between gas and liquid ceases to apply. Then supercritical drying ensures the solvent only exists in a single (supercritical) phase while it is being removed, thus eliminating the meniscus [Pajonk 98, Pierre 02].



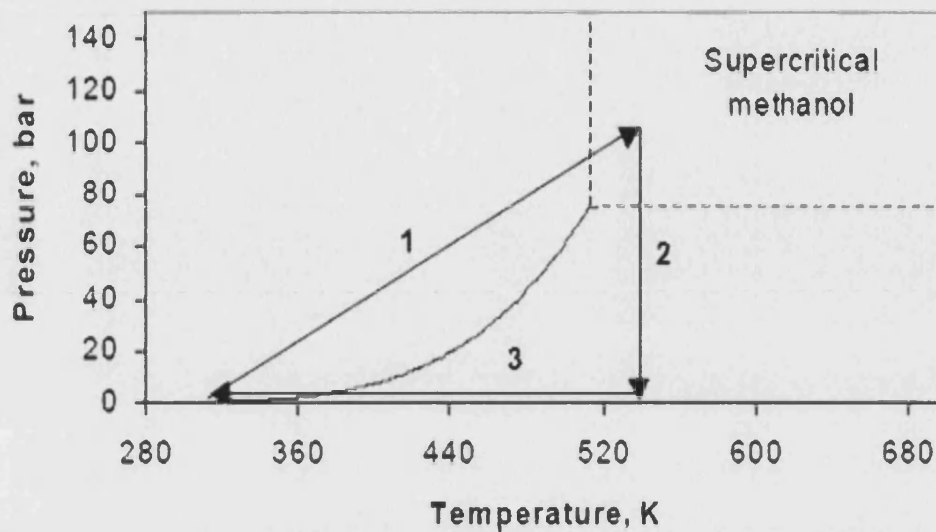


Fig. 3.9. Supercritical drying of methanol.

For the supercritical drying process the alcogel is placed in an autoclave which has been filled with the alcohol solvent. The process may last anywhere from 6 hours to 6 days. The supercritical drying for aerogel process based on methanol as a solvent is schematically represented in Fig. 3.9. The alcogel, together with a sufficient amount of methanol is placed in an autoclave, and the temperature and pressure are slowly raised (step 1 in Fig. 3.9) until they reach values above the critical point of methanol. The conditions are then kept constant for a time. This ensures that the autoclave is completely filled with the supercritical fluid, and therefore ensures the absence of liquid-gas interfaces in the pores during drying. The fluid is then slowly vented at constant temperature, resulting in a pressure drop (step 2 in Fig. 3.9). When ambient pressure is reached, the vessel is cooled to room temperature (step 3 in Fig. 3.9). Thus, the phase boundary between liquid and gas has not been crossed during the drying process except at the very end while cooling down.

### 3.2.2. Experimental Work

The aim of this experiment is to explore the feasibility of implementing the state of the art aerogel technology to optical fibres. Remarkably low refractive indices (for a solid material) of 1.002 to 1.05 [Pajonk 98] mean that air can be replaced by aerogel with little effect on the light. The idea is to surround a completed taper (including transitions) by aerogel material, and then study the optical transmission losses due to the aerogel material.

Several tapers with an outer diameter of 20  $\mu\text{m}$  were fabricated using SMF-28 in our facilities and I took them to Bratislava. The choice of the diameter was a matter of practicability. The tapers should be small enough to guide the light at the cladding-air boundary, but at the same time they should be big enough to survive handling and transport.

The sol for this experiment was prepared by mixing methanol and TMOS 1:1 in volume, then this solution is mixed with an ammonia solution (pH 9-10) 4:1 (MeOH/TMOS : Ammonia solution) in volume. This concentration was found empirically to make the gelation time very short. As soon as gelation was achieved the alcogel was covered by methanol to prevent excessive evaporation of the solvent before supercritical drying. The gelation time for our sample was between 5 and 8 minutes. This was long enough to handle and cast the sol but short enough for the process to be monitored in order to cover the alcogel at the right time.

A mould made from Teflon (see Fig. 3.10) was designed to hold the alcogel. Teflon can withstand the high temperature and pressure in the autoclave. The dimensions of this mould took into account the size of the autoclave (Fig. 3.11) and the total length of the taper waist and transitions. The taper was held provisionally in a slight curve so that the entire length (including transitions) was covered by the alcogel.

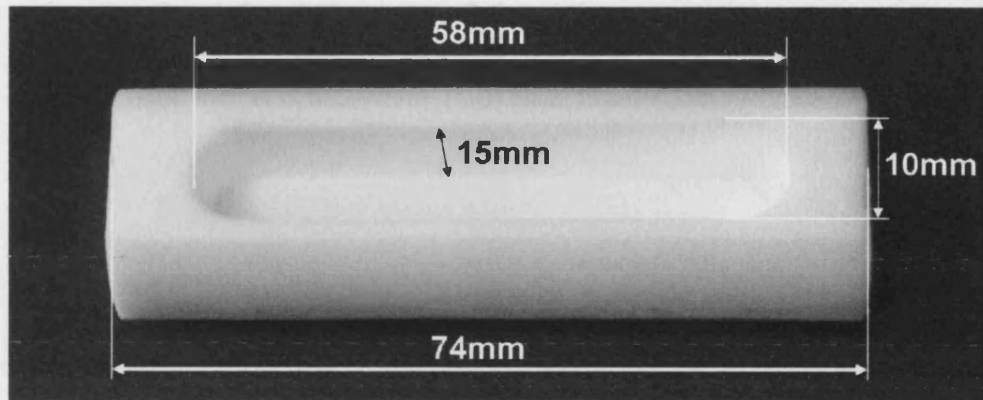


Fig. 3.10. Photograph of the sol-gel mould with dimensions.

Once the alcogel is formed, the taper already embedded in the material was released from the provisional holders. Then everything was placed inside a container immersed in methanol ready for the aging process. This aging process can take up to a week but in this case (due to time scale of my visit to Bratislava) it was reduced to one day and a half. After aging the sample was ready for supercritical drying in the one litre autoclave shown in Fig. 3.11.

The sample was placed inside the autoclave taking special care of the pigtails of the untapered fibre, and then the autoclave was filled to the top with methanol. The autoclave was closed and flushed several times with nitrogen gas to extract any remaining air inside the chamber. Then supercritical drying was started. First the pressure was increased to about 60 bar, then the temperature was raised every 15 minutes which further increased the pressure. Once the pressure reached about 110-120 bar it was held more or less constant by manually releasing pressure while the temperature was raised further to about 260 °C. After holding these conditions for a few minutes the pressure was dropped slowly until reaching atmospheric pressure, and the autoclave was left to cool down to room temperature before taking the samples out. The supercritical drying process took around 9 hours. The samples were carefully packed and transported back to Bath for optical transmission testing.

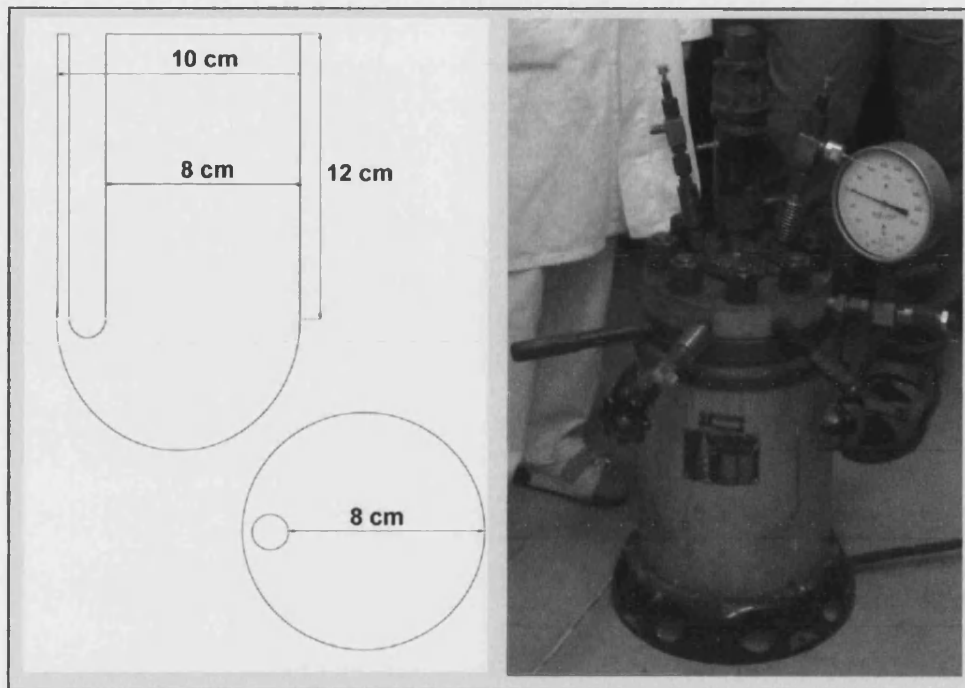


Fig. 3.11. Autoclave and sketch of the one litre volume inside.

Some preliminary results for the optical transmission properties were obtained by launching 633 nm light from a He-Ne laser into the untapered fibre, Fig. 3.12. In the figure, it can be seen that the scattering from the taper waist is not significant. Scattering exits at the input and output transitions, but there is no apparent increase of scattering within the aerogel block. Hence the aerogel does not cause scattering from the taper waist. Since the SMF-28 is multimode at this wavelength I conjecture that the scattered light is due to higher-order core modes being cut off by the taper transitions. The scattered light at the output is probably from higher-order cladding modes excited by the bending produced during the embedding process.

The optical transmission was measured at 1550 nm so that the SMF-28 core was single-mode and small enough in the taper waist that the light fills the fibre there. The light was coupled into the fibre and a reading of the optical power was taken at the other end. A cut back method was used to determine the losses. The transmission loss for the embedded taper in aerogel was 0.75 dB at 1550 nm which is probably mainly due to the bend rather than the aerogel.

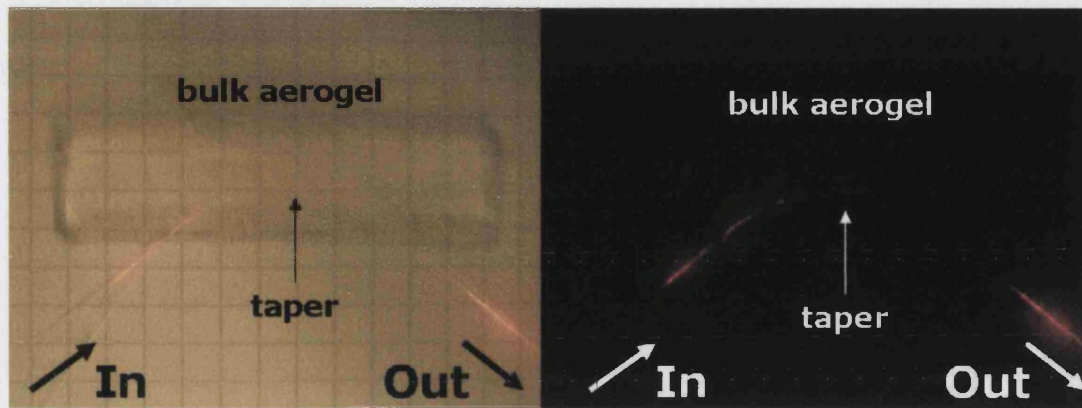


Fig. 3.12. 20  $\mu\text{m}$  tapered fibre embedded in bulk aerogel with He-Ne laser propagating through the fibre: (left) lights on, (right) lights off. The background is 5 mm squared paper.

The bulk aerogel material is quite brittle and it breaks easily. Also when it breaks produces really clean cuts as observed in Fig. 3.13. Unexpectedly the tapered fibres were not broken with the fracture of the aerogel so they can be pulled through the aerogel material. From this I understood that the links between the taper and the aerogel are very weak.

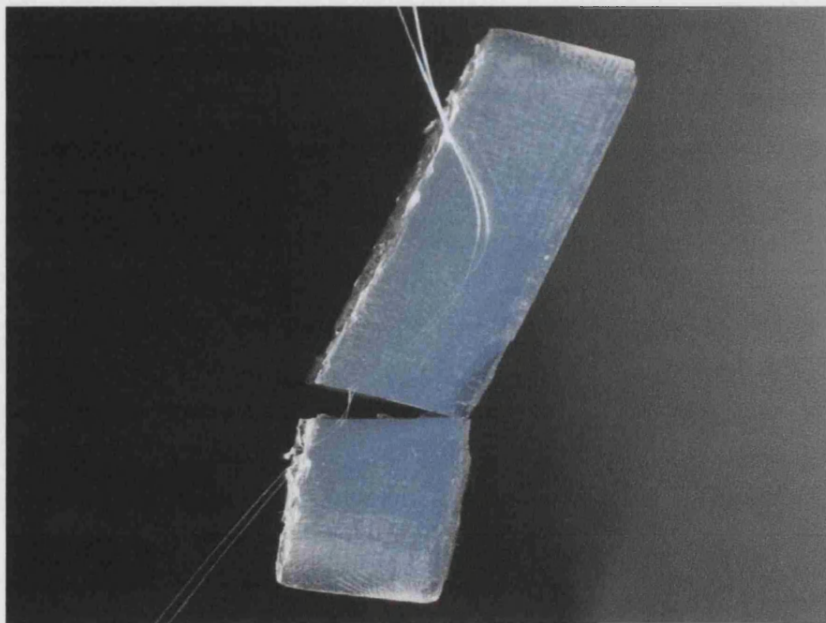


Fig. 3.13. Photograph showing a broken sample hanging from the two 20  $\mu\text{m}$  tapered fibre embedded in it.

### 3.3. Conclusions

Applications of sol-gel techniques to tapered fibres have been demonstrated. Taper waists have been coated with sol-gel films for the first time. This has led to a completely new method for making LPGs based on the three well-known techniques of tapering, sol-gel, and laser irradiation heating. The formation of aerogel blocks around tapered fibres has been achieved for the first time giving a promising proof of concept. This could be a building block for many exciting applications due to the peculiar physical and optical properties of this solid material, which I discuss in Chapter 9.

---

# Chapter 4

## Submicron Fibre Waveguides

In this chapter I report the fabrication and optical properties of submicron fibre waveguides. Submicron-diameter fibre waveguides have very interesting dispersion properties which are responsible for remarkable nonlinear properties in the visible regime. Submicron fibre waveguides were made by two alternative methods. Firstly, conventional fibres were tapered to reduce the *entire fibre* to submicron size (drawdown ratio up to 250:1). Secondly, PCFs were tapered to reduce the *fibre's core* to submicron size (drawdown ratio just up to 6:1). The transitions simplified input and output coupling in both cases. Standard tapering techniques are effective for making submicron taper waists, as well as submicron-pitch PCFs. I investigated the broadening of ns pulses emitted at 532 nm by a frequency-doubled microchip laser. Single-mode supercontinuum (SC) light spanning (yet largely confined to) the visible spectrum down to 400 nm were generated in as little as 20 mm of submicron fibre waveguide.

### 4.1. Dispersion in Submicron Fibre Waveguides

The generation of spectrally-broad single-mode SC light in small core PCFs [Ranka 00] or tapered conventional fibre [Birks 00] is well documented (as previously described in Chapter 2). In both cases, light is confined to a silica waveguide surrounded substantially or entirely by air. Low dispersion is the key to efficient broadening, as it enables single-mode phase-matching of the nonlinear processes that broaden the spectrum. All previously reported nonlinear work in PCFs and tapered fibres have been

focused in core/taper diameters around  $2\ \mu\text{m}$  or slightly less, where the ZDW is in the near infrared. However, calculations have shown that the ZDW shifts to visible wavelengths for waveguide diameters smaller than  $1\ \mu\text{m}$ .

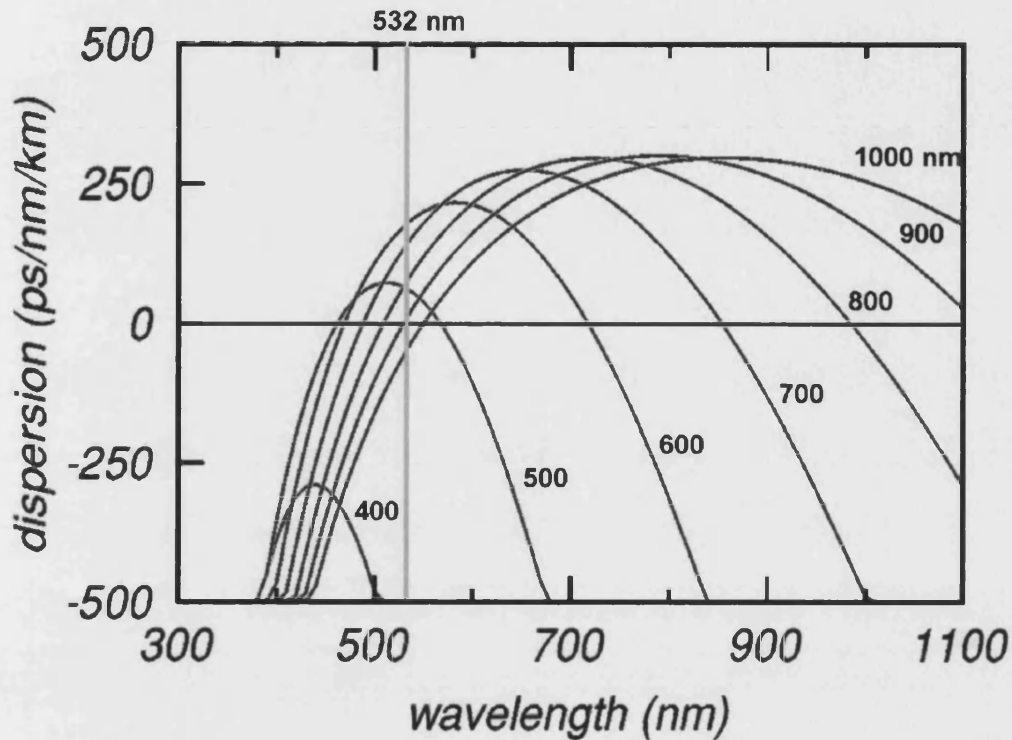


Fig. 4.1. Evolution of the calculated dispersion spectrum of taper waists (a strand of silica surrounded by air) as the diameter (labelled) decreases. The straight lines mark zero dispersion and 532 nm wavelength.

Tong et al [Tong 04], theoretically, studied the notable features of such submicron fibre waveguides. Fig. 4.1 shows the calculated dispersion spectra of taper waists for different diameters based in the model of a silica strand surrounded by air. The first ZDW appears at  $\sim 532\ \text{nm}$  for taper waists of around  $900\ \text{nm}$  diameter. At around  $500\ \text{nm}$  taper diameter, the dispersion has a flattened-at-zero response around  $532\ \text{nm}$ . For this diameter the first and the second ZDW are  $\sim 455$  and  $565\ \text{nm}$  respectively. These characteristics are well-suited to SC generation when pumped with a frequency doubled Nd:YAG laser at  $532\ \text{nm}$  (vertical grey line in Fig. 4.1).



## 4.2. Submicron Tapered SMFs

The fabrication of submicron-diameter taper waists was recently publicised by Tong et al [Tong 03], though it was first reported some years ago [Bures 99]. Unlike Bures et al., Tong et al. used a two-stage process involving a heated sapphire tip. In the next subsection I show that this extra step is unnecessary and I report the fabrication of submicron-diameter taper waists showing much lower loss than Tong et al. (over two orders of magnitude less per mm). In Subsection 4.2.2 I demonstrate visible SC generation in such taper waists when pumped with a frequency doubled Nd:YAG microchip laser [Leon-Saval 04a, Leon-Saval 04b].

### 4.2.1. Fabrication and Loss of Submicron SMF Tapered Fibres

It is clear that the low-loss fabrication of such waveguides relies in the quality of the taper rig as well as the tapering approach (as explained in Chapter 2). I believe that the key feature of our taper rig that enable such thin tapers to be made are the variable length adaptation [Birks 92] of the flame brush technique and also the nature of the flame.

Control of waist diameter is a key parameter for nonlinear experiments. The predictability of the variable flame-brush technique [Birks 92] was improved by explicitly modelling what happens when a flame passes at speed  $u$  along a fibre stretched at rate  $v$ . Conservation of volume leads to the ratio by which the diameter  $d_n$  of the waist is reduced by a single pass of the flame:

$$\frac{d_{n+1}}{d_n} = \left[ \frac{1 - v/2u}{1 + v/2u} \right]^{1/2} \quad \text{Equation (4.1)}$$

With this refinement, waists of specified diameter could be produced despite the high drawdown ratios involved (up to 450:1). For example, Fig. 4.2 is an SEM image of a waist of nominal diameter 620 nm made from SMF-28. The measured diameter of the taper waist from the SEM was 634 nm matching the predicted value to within the 3 % ( $\pm 19$  nm) accuracy of the SEM.

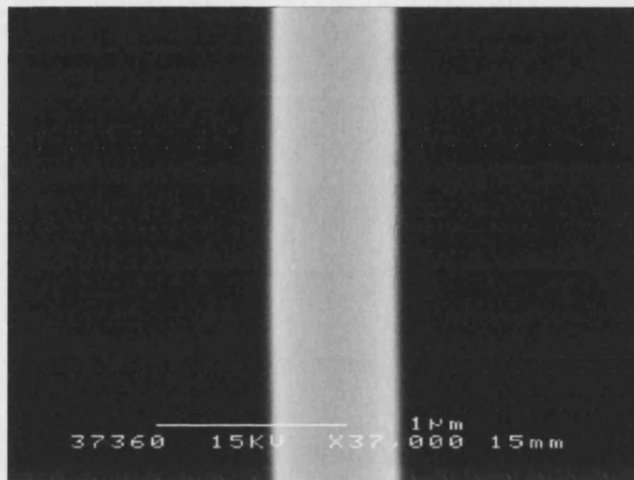


Fig. 4.2. SEM image of a taper waist with a nominal diameter of 620 nm, as predicted by Eq. 4.1.

Loss for such submicron-diameter tapers was measured by simply recording transmission before, during and after tapering in real time. For single-mode measurements at wavelengths where the SMF-28 is multimode, a section of fibre was tapered (in situ; no splices needed) to make it locally single-mode. Any light in higher modes spreads into the cladding and is absorbed by index-matching gel placed around the fibre [Ozeki 75]. A low drawdown ratio of about 3:1 was enough to ensure only fundamental-mode excitation at wavelengths as short as 532 nm in submicron waists subsequently made downstream of this mode filter.

Table 4.1: Typical loss per unit length, for taper waists with the specified diameter and length, compared with the results of Tong et al.

<i>diameter (nm)</i>	<i>length (mm)</i>	<i>wavelength (nm)</i>	<i>loss (dB/mm)</i>	<i>loss from [Tong 03] (dB/mm)</i>
950	90	1550	0.0014	0.21
890	90	1550	0.0017	0.29
360	30	633	0.0083	0.21
280	30	633	0.011	0.38

The losses of typical samples made using SMF-28 fibre are given in Table 4.1, showing up to two orders of magnitude lower loss despite including the losses of the transitions. This shows that the two-stage process proposed by Tong et al. is not necessary. Indeed, their higher losses, and the fact that they end up with just half of the taper, shows that the two-stage process is worse in many ways. Brambilla et al. [Brambilla 04] (after this work was reported in February at OFC 04) also confirmed that conventional tapering is indeed better for the fabrication of such submicron tapered waists, although they obtained 10x worse losses than ours and did not explore the nonlinear properties of such structures.

#### 4.2.2. Nonlinearity in Submicron Tapered SMFs

Visible SC light was generated using a frequency doubled Nd:YAG microchip laser in submicron taper waists. The laser emission wavelength was 532 nm and the Q-switched pulses were 0.6 ns long with a repetition rate of 6.33 KHz and less of 1 KW peak power coupled into the fibre. Light from the laser was coupled into the fibre via a variable attenuator and the output at the other end of the fibre was monitored using an optical power meter. The fibre was then tapered to submicron diameter. In all cases described below the loss was less than 0.2 dB with taper waists length of 20 or 90 mm. The input power was then increased and the output spectrum measured using an Ando AQ6315B optical spectrum analyser.

The dispersion is zero or flattened at 532 nm in waists with diameters around 900 or 500 nm respectively, Fig. 4.1. This facilitates SC generation despite the short length and low peak power. Typical output spectra are plotted in Fig. 4.3, for two different diameters, 920 and 510 nm. The SC spectrum fills the visible range but extends little beyond it. However, only 20 mm of 510 nm fibre (and half the power) was needed to fill the visible spectrum, compared with 90 mm of 920-nm fibre.

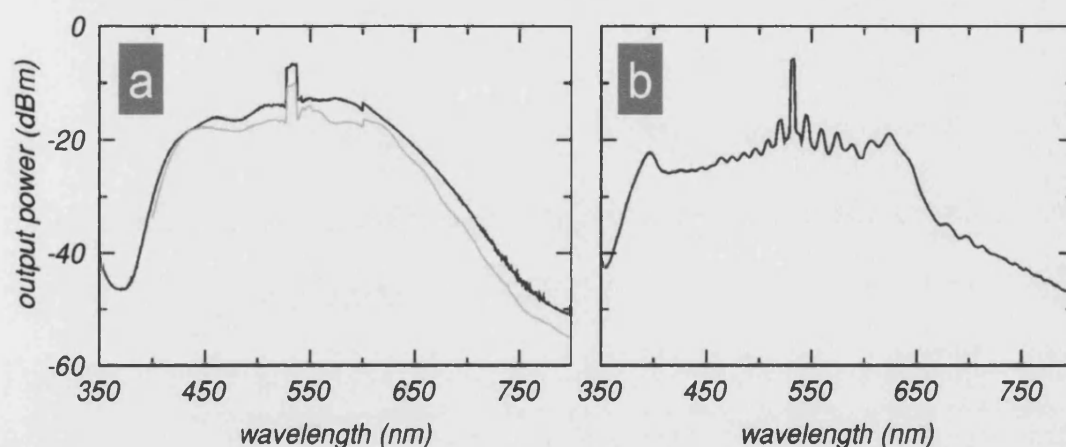


Fig. 4.3. SC spectra generated by taper waists for diameter, length and average laser power of (a) 920 nm, 90 mm and around 3 mW, and (b) 510 nm, 20 mm and around 1.5 mW respectively. The grey curve in (a) is for a sample made from Nufern 630-HP fibre instead of Corning SMF-28.

SC spectra from two samples of 920 nm diameter, otherwise identical except one is made from Nufern 630-HP fibre (cutoff wavelength 545 nm) instead of SMF-28, are plotted in Fig. 4.3(a). Despite the difference between the fibre's cores, and particularly that the Nufern fibre is single-mode near the pump wavelength, the spectra are virtually indistinguishable. This is further confirmation that the processes are single-mode and the mode filter approach (described earlier on in this section) used for these experiments works. Nevertheless the operation of the mode-filter was verified by inspecting the output far-field pattern at low power on the 920 nm taper waist made from the SMF-28, Fig. 4.4(a). The output at around 2.5 mW average laser power was white despite the persistence of unconverted pump light [Fig. 4.4(b)]. It remained in the

fundamental mode; no multimode coupling was observed. The white SC output was passed through 10 nm bandpass filters and the far-field patterns were imaged. Those patterns show no evidence of higher-order modes, Fig. 4.4(c)-(e), in contrast to the work by Provino et al. [Provino 01] where the broadening of the spectrum is based on high-order modes.

Fig. 4.4(f) maps the evolution of the spectrum with power. SC generation has apparently not saturated: broader spectra could be expected for higher powers or a longer waist. This is analogous to the results of Wadsworth et al. [Wadsworth 04a] in 1-m of 5  $\mu\text{m}$  core PCF, in contrast to 20-m of PCF where SC generation had saturated and increased power or length made little difference.

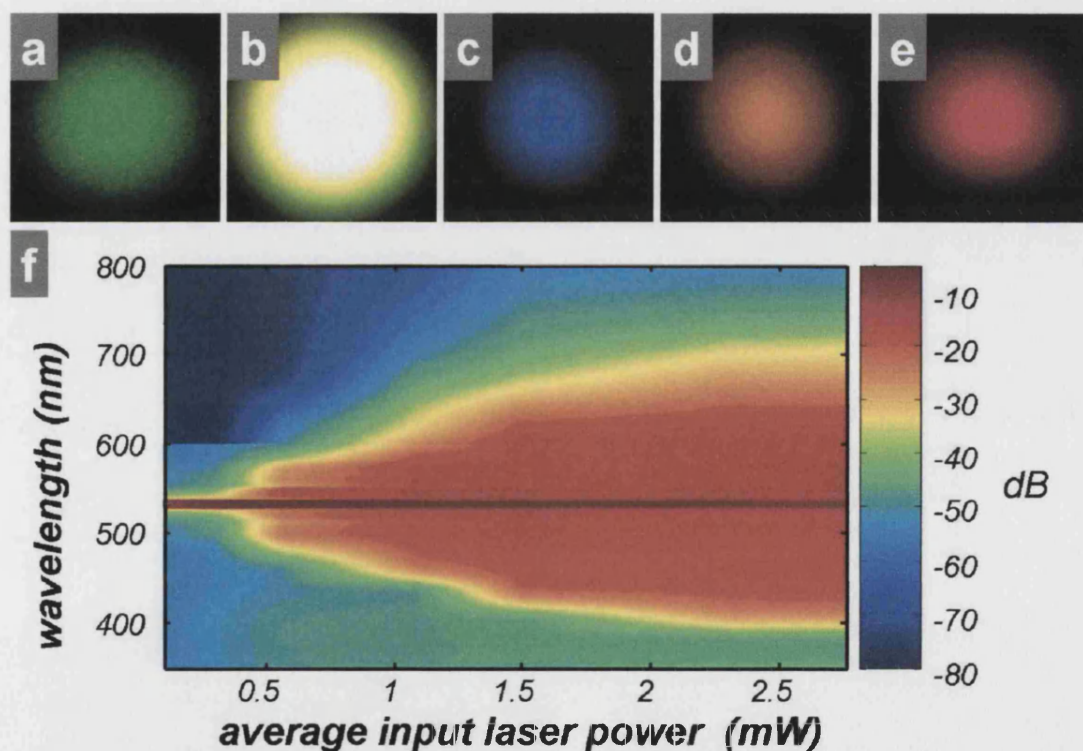


Fig. 4.4. Output far-field patterns from a 920 nm diameter tapered fibre made from SMF-28 for (a) low and (b) maximum power. The pattern in (b) was passed through 10-nm bandpass filters at (c) 450, (d) 589 and (e) 633 nm. (f) The variation of the SC spectra with average pump power.

### 4.3. Submicron-Core PCFs

A highly nonlinear small PCF core is like a narrow taper waist. Light is confined to a silica waveguide surrounded substantially by air, and their dispersion and nonlinear properties are similar [Birks 00, Ranka 00]. However tapered fibres have received less attention for SC generation than PCFs, probably because they are short and need to be carefully packaged. Nevertheless input and output coupling in tapers is simple for any waist diameter, whereas for PCFs it becomes ever more difficult as core size decreases because there is no transition to a larger input core. Also high air-filling fraction PCFs with submicron pitch are hard to make, because of air-hole collapse, especially since the air-filling fraction must be high for light to be well-confined to the core. To combine some of the advantages of both waveguide structures (tapered and PCF fibres), our tapering rig was used in order to make sections of PCF with submicron cores from relatively large-cores high air-filling fraction PCFs. Then visible SC light was generated using a frequency doubled Nd:YAG microchip laser in the submicron PCF cores [Leon-Saval 04a, Leon-Saval 04b].

#### 4.3.1. Fabrication of Submicron-Core PCFs by Tapering

PCFs of submicron pitch are hard to make because the holes are likely to collapse completely under surface tension (or explode if pressurised). However, tapering is better at preserving holey structure than fibre drawing on a tower. To minimise hole collapse, an ideal process would pull the preform at peak stress (ie, the breaking stress of the glass). Conventional fibre drawing is far from this ideal: the force along the neck-down region is the same, so the stress in its wider parts is reduced, Fig. 4.5. In contrast, tapering applies constant stress governed by viscosity and elongation rate [Tajima 94], so if that stress is maximised then tapering does approach the ideal. It can be shown that hole distortion is less in tapering than drawing (if both are optimised) by a factor equal to the drawdown ratio  $\rho$  ( $\rho > 1$ ) [Birks 05a].

Hence by tapering "fast-and-cold", ie with relatively high elongation rate and low flame temperature for high drawing stress, the microstructure in 90-mm lengths of the

PCF could be preserved while reducing the core diameter to as little as a few hundreds nm. Note the contrast between treatments of conventional fibres and PCFs, which were tapered so that the whole of the former but just the core of the latter was reduced to submicron size: the outer diameter of the tapered PCF waist was as big as 30  $\mu\text{m}$ .

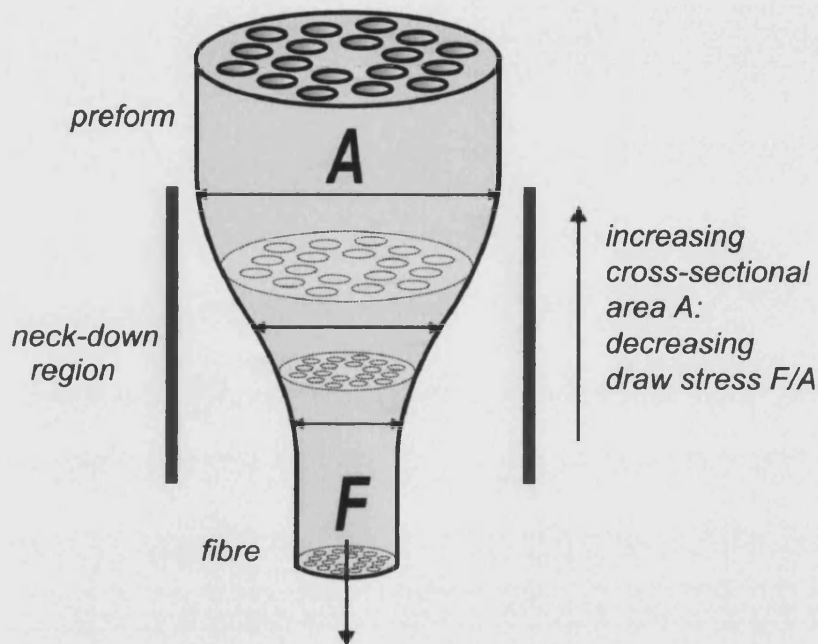


Fig. 4.5. Conventional fibre drawing: the drawing force  $F$  is uniform along the neck-down region in the furnace, so wider parts are being drawn at low stress even if the fibre leaves the furnace at breaking stress.

The fibre used for this experiment was a highly nonlinear 3.1  $\mu\text{m}$  core PCF supplied by BlazePhotonics [NL-33-880]. Although the PCF did not have the conventional guiding core of Liu et al's special tapered PCF [Liu 01], coupling to a 3.1  $\mu\text{m}$  core is straightforward. The taper transitions form low-loss interfaces to the submicron core by satisfying the same adiabaticity criteria as in conventional tapered fibre. SEM images for the original fibre and the taper waists with core diameters of 700 nm and 500 nm are shown in Fig. 4.6.

Loss measurements were less reliable than for conventional fibre, as a mode-filter would need similar dimensions to the submicron sample itself. However, around 0.5 dB tapering loss was measured after optimising coupling to the fundamental mode,

giving a transition loss of 0.25 dB. I believe much of this represents the losses of remaining higher-order modes through the transition due to the different adiabaticity criteria for the different modes.

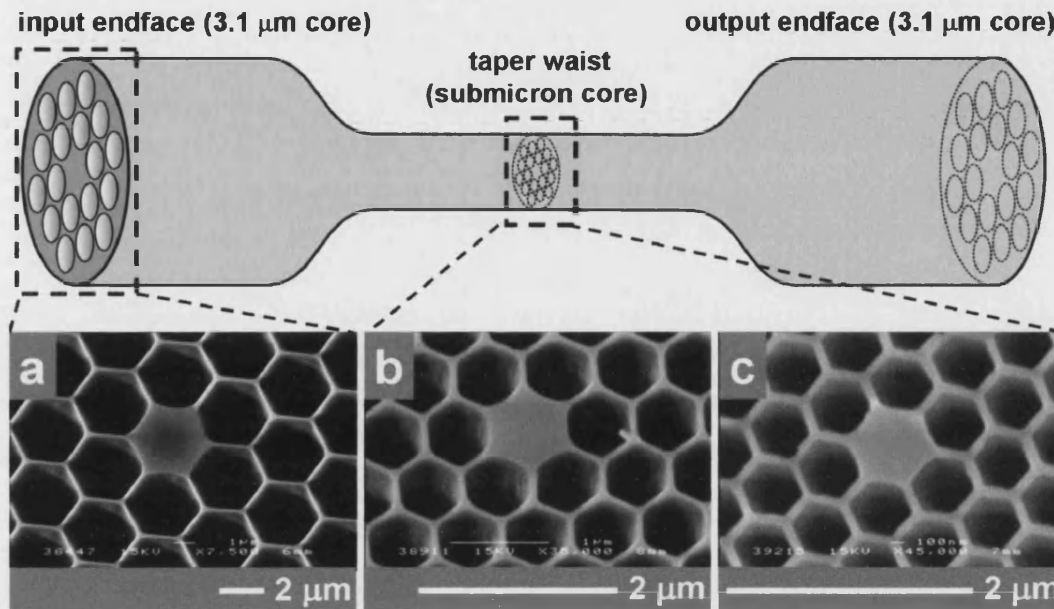


Fig. 4.6. SEM images of PCF cores of diameter 3.1 (untapered), 0.7 and 0.5  $\mu\text{m}$  (left to right; different scales).

#### 4.3.2. Nonlinearity in Submicron-Core PCFs

The dispersion spectra of the tapered PCF waists were not calculated, but should resemble those of conventional taper waists of comparable size [Fig. 4.1]. Typical SC spectra obtained in experiments analogous to those with tapered SMF are shown in Fig. 4.7. The 532 nm laser light was coupled into the untapered 3.1  $\mu\text{m}$  core PCF and the spectrum was recorded (in the same way that for the conventional SMFs) for the two different taper waists (90 mm long) with cores of 700 and 500 nm (Fig. 4.7).

The spectra are similar to those of the conventional tapers, though the one for the 500 nm diameter core spreads further into the infrared. The reason for this could be that the actual interaction length for this submicron PCF core was 90 mm instead the 20 mm of the submicron tapered SMF. In the other hand the 700 nm core PCF with



the same interaction length than the tapered SMF of 920 nm share a very similar SC spectrum in shape and power.

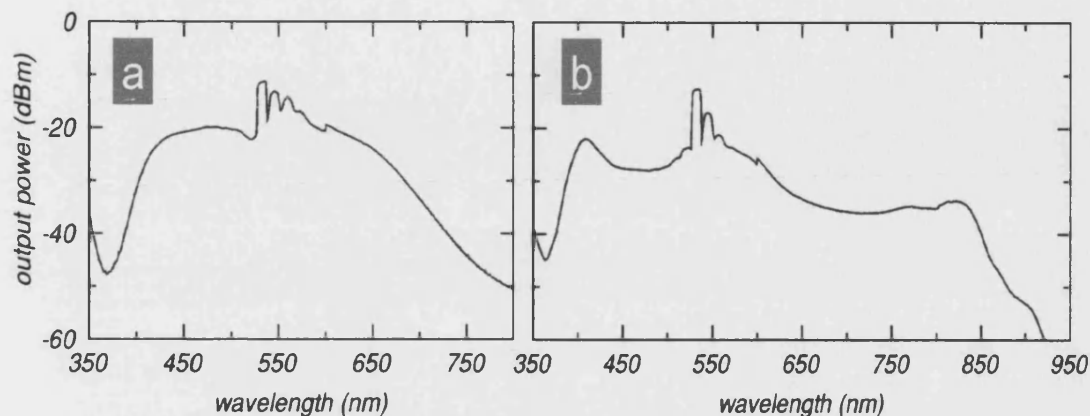


Fig. 4.7. Supercontinuum spectra generated by PCF cores of diameter (a) 700 nm and (b) 500 nm. Both were 90 mm long and carried an average power of around 1.7 mW.

#### 4.4. Discussion and Conclusion

A dispersion regime well-matched to frequency-doubled microchip lasers has been explored. Previous reports of SC generation with 532 nm light (eg [Provino 01]) relied on higher-order modes in bigger cores for nonlinear phase-matching, whereas in submicron waveguides phase-matching is possible in the fundamental mode. The physics of the nonlinear broadening is expected to be as discussed in [Wadsworth 04a] but applied to shorter wavelengths. The resulting single-mode SC filled the visible spectrum while extending little beyond it. This is significant for visible applications, as any infrared light generated would be wasted. The resulting compact visible source could find applications in optical coherence tomography, spectroscopy and optical device measurement.

Important developments in the fabrication of the submicron waveguides themselves are also described. For taper waists, use of a sapphire tip was presented as an enabling innovation in the well-publicised work by Tong et al [Tong 03] but is

nevertheless a cumbersome extra process step that yielded only half the complete taper structure. One transition was missing, and further steps had to be taken to couple light in and out. However, the extra step is unnecessary. Conventional tapering is actually superior, yielding complete structures with transitions at both ends and uniform waists up to 100 mm long or as little as 300 nm in diameter. Made by machine with less human intervention, losses per mm can be over one and some cases up to two orders of magnitude lower than [Tong 03].

Tapering was used to make PCFs of submicron core diameter and pitch, and I described the guidance of light in such structures. Our CLEO 04 postdeadline paper [see publication list] was the first report of SC generation in air-silica fibre waveguides of submicron diameter, and indeed of any form of optical guidance along PCFs with submicron pitch. The narrowest taper waist or PCF core for which SC generation has been studied until that date was 1  $\mu\text{m}$ . Significantly, the only other reports of submicron pitch PCF structures (published after this work) being more or less well preserved after drawing were also obtained by tapering [Foster 04, Lizé 04]. This supports the argument that tapering is inherently better at preserving nanostructure in PCFs. It also corroborated the interest for such remarkable waveguides and their properties.

The disadvantage of tapering is that only short lengths are produced. However, some applications only need cm lengths, and for these tapering should be the best way to make nanostructured PCFs.

---

# Chapter 5

## Hole Inflation in PCFs

Previous work on tapering of PCFs was based on avoiding the hole collapse. Nevertheless the holes of the PCF structure always tend to get smaller relative to the pitch  $\Lambda$ . The hole shrinkage has been minimised to preserve the hole structure, even in very small-pitch PCFs (as shown in Chapter 4) by reducing the heating time and temperature ('fast and cold' tapering). However, in this and other reports of PCF tapering [Foster 04, Nguyen 05] both the core size and the air filling fraction were reduced from their initial values (or kept fixed) by the tapering process.

A much greater range of devices would be possible if the air filling fraction of a PCF (or indeed the absolute hole size) could be increased during tapering, but little attempt has been made to do this. By pressurising the holes during tapering, a modest expansion was achieved to form a mode converter [Birks 02], in which the ratio  $d/\Lambda$  of hole diameter to pitch increased from 0.45 to 0.66 while the pitch was reduced from 8 to 1.7  $\mu\text{m}$ . Reference has also been made to the blocking off of holes to maintain sufficient pressure and so resist hole collapse under surface tension [Magi 04]. However, in both cases the character of the PCF structure was unchanged, with near-circular holes and a relatively low air filling fraction.

In this chapter, I will describe controlled and essentially unlimited hole inflation in PCF from  $d/\Lambda = 0.4$  to very large holes with air filling fraction  $> 90\%$  by heating the fibre at the same time as applying pressure to the holes. The inflated fibres were then tapered fast and cold to preserve the new structure whilst reducing the core diameter to 1-2  $\mu\text{m}$  [Wadsworth 05]. This allows interfacing between widely different types of PCF.

Supercontinuum generation in a "cobweb" PCF with a small core and a very high air filling fraction, interfaced to an endlessly single-mode (ESM) PCF with a large core and a relatively low air filling fraction, was demonstrated as an example application of this type of device. I also used differential hole pressurisation and heat treatment to radically change the core shape along a piece of non-birefringent PCF, forming a low-loss transition to a highly-birefringent core with a sub-millimetre beatlength.

### 5.1. Hole Collapse/Expansion and Surface Tension

While tapering a PCF the surface tension in the holes acts as an effective pressure. For a cylindrical hole in a liquid the excess hydrostatic pressure  $P_{st}$  required to resist collapse is related to the surface tension  $\gamma$  of the liquid by [Tabor 69]

$$P_{st} = 2\gamma/d \quad \text{Equation (5.1)}$$

where  $d$  is the hole diameter. For a given hole diameter and excess internal gas pressure  $P$ , the hole will either expand or shrink depending on whether  $P$  is greater or less than  $P_{st}$ . Although the viscosity of silica glass does change rapidly with temperature close to the softening point of 1700 °C, the surface tension varies little with temperature [Kingery 59]. Whether a hole in fused silica shrinks or expands therefore depends only on the diameter and the internal pressure: the temperature of the glass and the magnitude of the pressure difference  $P - P_{st}$  only determine the rate of hole expansion or collapse. Given the commonly-quoted value of  $\gamma = 0.3 \text{ J/m}^2$  for silica [Kingery 59], Eq. (5.1) is conveniently expressed in terms of pressure in bar and hole diameter in  $\mu\text{m}$ :

$$P_{st}(\text{bar}) = 6/d(\mu\text{m}) \quad \text{Equation (5.2)}$$

so an excess pressure of 6 bar is needed to keep a 1- $\mu\text{m}$  hole in (unstable) equilibrium.

## 5.2. Adiabaticity in Hole Size Transitions

For the structural transitions to have low optical loss, the guided mode must transform adiabatically through the transition. In practice this means that any changes in mode size or shape in the structural transition must be over a length scale long compared to the diffraction of the guided mode [Love 87]. In this work transitions of both hole size and core diameter are considered, starting with ESM PCFs with core diameters of 5 or 12  $\mu\text{m}$ , i.e. large compared to the wavelength. For such fibres the mode is well confined to the core at visible and near-infrared wavelengths. If the hole diameter is increased by inflating the fibre without stretching it, core size almost unchanged; the fundamental mode will still fill the core so the mode field diameter (MFD) will not change much. For example the MFD is plotted against  $d/\Lambda$  for a PCF with a fixed solid core diameter of 5  $\mu\text{m}$  in Fig. 5.1. The core diameter was defined as the distance between the inner edges of the inner ring of air holes

$$d_{\text{core}} = 2\Lambda - d = \Lambda\left(2 - \frac{d}{\Lambda}\right) \quad \text{Equation (5.3)}$$

Field profiles are calculated using a full-vector plane-wave model for round holes [Johnson 01] and the MFD is calculated as described in Chapter 1.

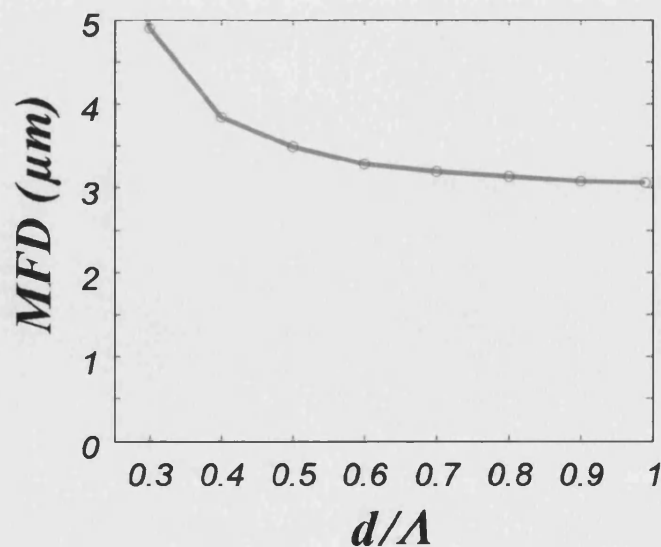


Fig. 5.1. Calculated MFD at a wavelength of 1  $\mu\text{m}$  for PCFs with a 5  $\mu\text{m}$  diameter solid core and varying  $d/\Lambda$ .

The small change in MFD (shown in Fig. 5.1) with hole diameter suggests that adiabaticity will be easy to fulfil for this type of hole expansion. Normally the core size would also be changed by tapering, but adiabaticity considerations should be the same as in “standard” (unpressurised) PCF tapering.

### 5.3. Hole Inflation and Tapering Technique

Two conditions must be met for hole expansion in PCF. Firstly the internal pressure must exceed that set by eq. (5.2), and secondly the fibre must be heated long enough and hot enough to allow the expansion to take place. A gas cell with a fibre chuck and optical window [Fig. 5.2(a)] is used to pressurise the fibre with dry nitrogen whilst still allowing optical access for monitoring of the fibre transmission during processing. To process a length of fibre in a controlled manner the standard flame-brush tapering rig was used. The fibre was stretched slightly to keep it taut while heated, to an extent that would reduce the transverse scale of the fibre by 8% if  $d/\Lambda$  was unchanged. Transitions from unprocessed fibre to inflated fibre were made by heating a shorter length of fibre with each successive sweep of the burner.

The tapering parameters required for hole inflation are actually the opposite of those needed to taper with little hole collapse. To prevent hole collapse under surface tension without pressure I taper ‘fast and cold’, with a cold flame to minimise the rate of hole collapse, and stretching as quickly as possible to minimise the processing time. In contrast, for hole inflation the tapering process must be ‘slow and hot’, using a hot flame for rapid hole inflation and stretching slowly to increase the processing time. In order to increase the rate of hole expansion I aimed to increase the temperature of the oxygen-butane flame by increasing the ratio of oxygen in the mix. Unfortunately increasing the oxygen ratio also moves the hot zone of the flame closer to the burner aperture (an array of 3 holes 1 mm in diameter drilled onto a stainless steel pipe), and with a metal burner the proximity of the metal cools the flame. In order to eliminate this cooling I made a new burner made from silica glass.

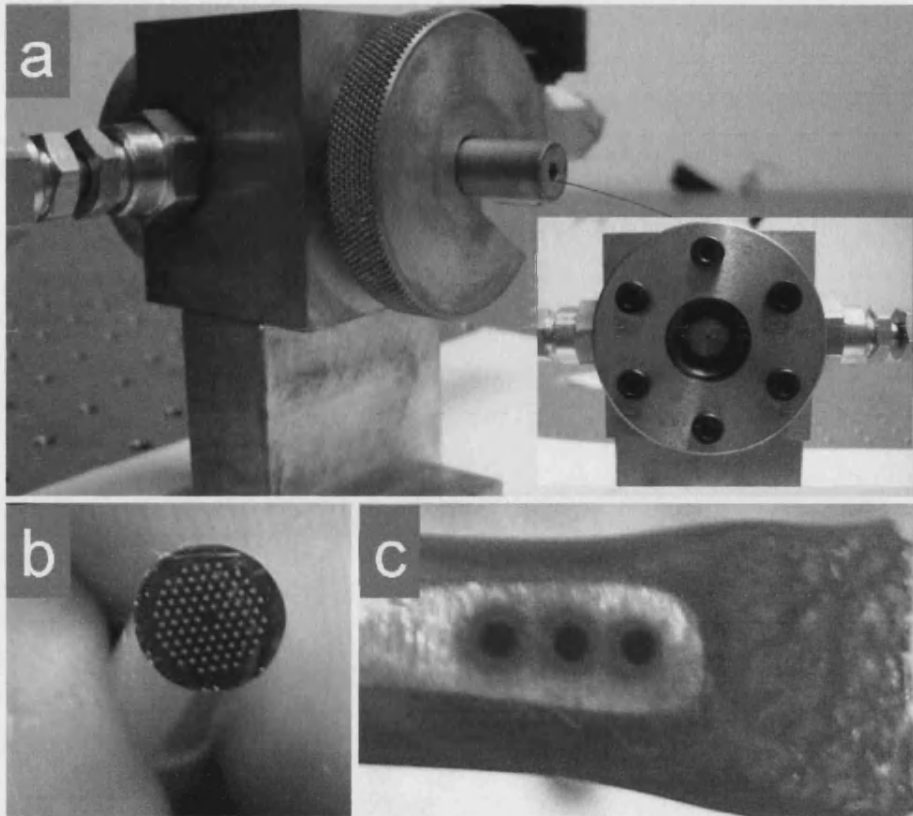


Fig. 5.2. Photographs of (a) the gas cell used to pressurise the holes of the fibres and allow optical input and output from the core, (inset) frontal view of the optical window; (b) silica burner with 108 holes of 125 $\mu\text{m}$  diameter and (c) typical steel burner used in our taper rig. Photographs (b) and (c) are roughly at the same scale.

This burner (a piece of an ESM PCF preform) was 2.8 mm in diameter and had an array of 108 holes, each 125  $\mu\text{m}$  in diameter [Fig. 5.2(b)]. The small holes allow larger oxygen content in the flame and also make the flame uniform over a larger total flame size. Unlike steel the silica has a low thermal conductivity, which prevents the heat of the flame dissipating into the burner. The uniform 2.8 mm diameter flame increases the effective processing time for each portion of the fibre under the moving flame.

After making sections of fibre with inflated air holes, the fibres could be placed back in the tapering rig and tapered in a conventional ‘fast and cold’ process. This can reduce the core diameter of the PCF to small sizes as required. The entire process is shown schematically in Fig. 5.3. Since this second stage is just the standard tapering process that I have previously applied to PCF (Chapter 4), it is already established that they should be adiabatic.

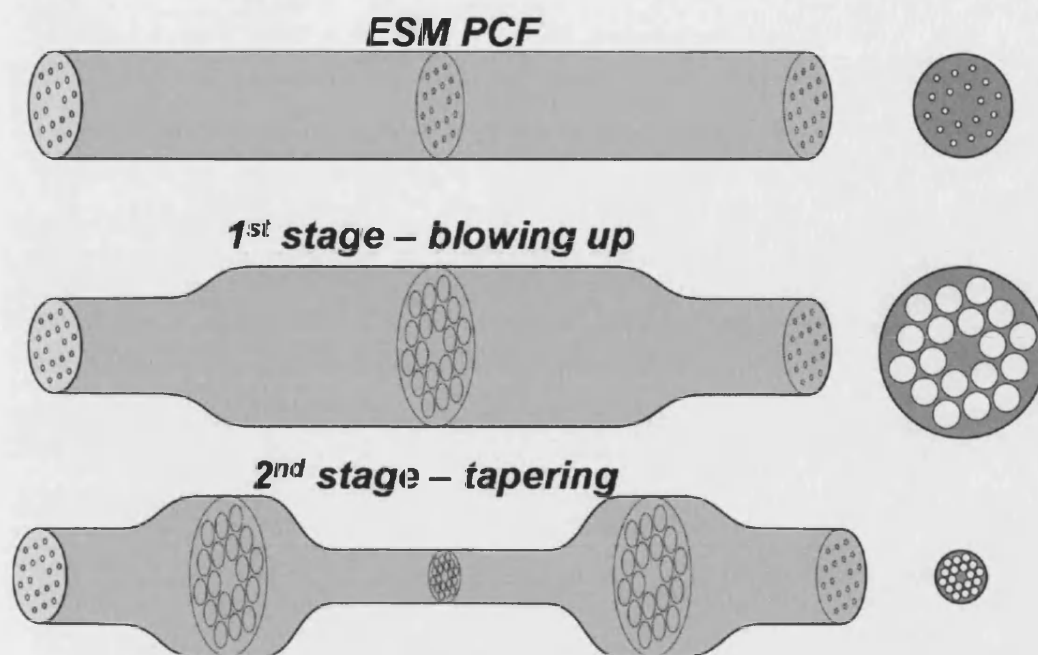


Fig. 5.3. Schematic drawing of fibre inflation and tapering process to produce small core highly nonlinear PCFs with large air holes, connected to both ends to ESM PCF pigtails with small air holes.

## 5.4. Experiment

### 5.4.1. Hole Inflation Without Tapering

The fibre is placed in the tapering rig and slightly stretched while heating it and pressurising the holes. The flame travels in the same way as in the standard tapering process but the travelling distance shortens with every sweep. Since the inflation of the holes has a monotonic relation with the heating time, this produces a length of inflated waist and two transitions where the hole size increases gradually. The inflated section was 70 mm long with 30 mm transitions, with processing time of 280 sec. The flame made 13 sweeps with different length translations according to the “flame & brush” technique [Birks 92]. The total effective heating time for each portion of fibre waist was estimated to be 9 sec. With constant flame conditions and tapering and burner speeds, the inflation of the holes was controlled by using different nitrogen pressures.



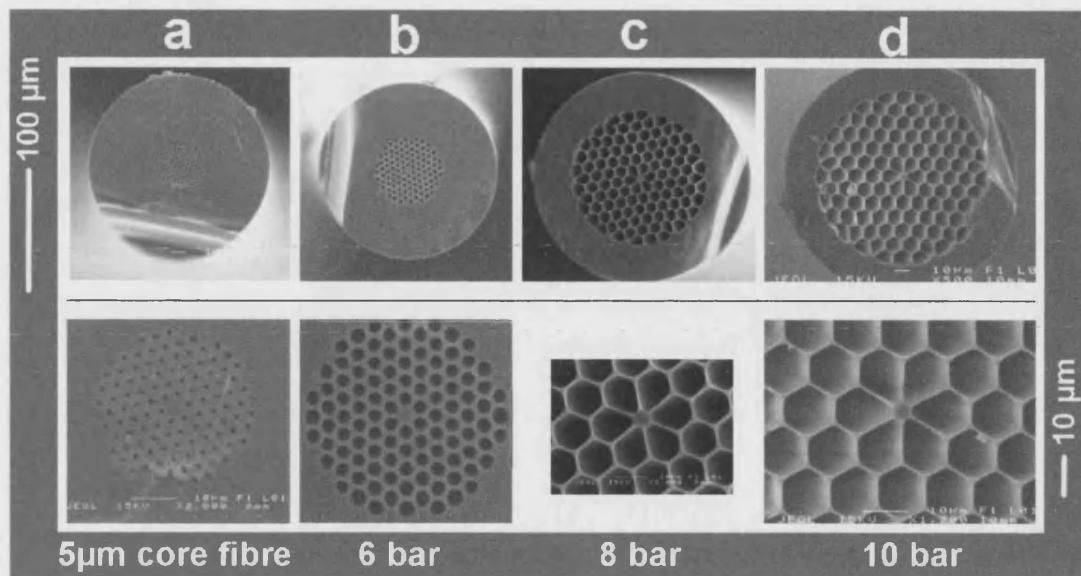


Fig. 5.4. SEMs of (a) the original 5  $\mu\text{m}$  core ESM PCF (b)-(d) the same PCF inflated at pressures of 6, 8 and 10 bar respectively.

Fig. 5.4 shows SEMs of a 5- $\mu\text{m}$ -core ESM PCF inflated at pressures from 6 to 10 bar under otherwise identical conditions. The initial fibre had  $\Lambda = 3.2 \mu\text{m}$ ,  $d/\Lambda = 0.43$  and outer diameter  $\text{OD} = 125 \mu\text{m}$ , making it splice-compatible to conventional step-index fibre designed for 1060 nm light. The hole diameter was  $3.2 \times 0.43 = 1.4 \mu\text{m}$ , so from eq. (5.2) a pressure of 4.3 bar was required to counter surface tension. The more highly-inflated fibres have the "cobweb" structures of some highly-nonlinear PCFs [Wadsworth 02], with a core suspended from thin webs and almost entirely surrounded by air, although the core diameter was of course much greater at this stage.

Parameters measured from the SEMs are given in table 5.1. For highly inflated fibres (8 and 10 bar) the hole size  $d$  in  $d/\Lambda$  is the distance across the flats of the rounded hexagonal holes. The initial core diameter (the solid region between the inside edges of the central ring of holes) was 5.0  $\mu\text{m}$ . During the processing the fibre was stretched slightly (as mentioned above), which in the absence of hole collapse or expansion would have proportionately changed the fibre's dimensions to those given under the heading "scaled fibre", the final core diameter being reduced by 8 % to 4.6  $\mu\text{m}$ . The core diameters for all three inflated fibres were slightly smaller than this,

indicating that there was some flow of glass from the core into the webs holding the core. The increased air filling fraction in the fibres also increased their outside diameter. The scaled fibre should have an OD of 115  $\mu\text{m}$  and contain 120 holes of  $1.4 \times 0.92 = 1.29 \mu\text{m}$  diameter.

Table 5.1: Dimensions of the inflated PCFs shown in Fig. 5.4. The scaled fibre values are obtained by multiplying the initial fibre values by the same factor of 0.92, to represent the effect of the slight tapering if the holes did not deform.

	<i>Initial Fibre</i>	<i>Scaled Fibre</i>	<i>6 bar</i>	<i>8 bar</i>	<i>10 bar</i>
<b>OD</b>	125	115	121	144	163
<b><math>d_{core}</math></b>	5.0	4.6	4.0	4.0	3.7
<b><math>d</math></b>	1.4	1.29	2.9	8.0	10.5
<b><math>\Lambda</math></b>	3.2	2.9	3.8	8.3	10.8
<b><math>d/\Lambda</math></b>	0.43	0.43	0.74	0.96	0.98
<b><i>Air filling fraction</i></b>	0.16	0.16	0.50	0.91	0.95
<b><i>Loss (dB)</i></b>	--	--	0.08	0.10	0.05

The total area of glass in the fibre cross-section will be the same for all the inflated fibres. A greater proportion of air in an inflated fibre will then necessarily increase the fibre OD in a predictable way. Monitoring fibre OD is standard in fibre drawing towers, and if implemented on an inflation rig would give a clear online indication of the hole size attained. Optical losses from 0.05 to 0.3 dB for 1550 nm light were measured during the inflation process. Losses at shorter wavelengths are expected to be even lower as the guided mode will be more strongly confined to the core and will therefore be less effected by changes in hole size.

A 12- $\mu\text{m}$ -core ESM PCF was also processed in the same way. This fibre had  $\Lambda = 8 \mu\text{m}$ ,  $d/\Lambda = 0.46$  and OD = 125  $\mu\text{m}$ . The mode field diameter matches standard SMF-28 at 1550 nm, allowing low-loss splices to conventional fibre systems.

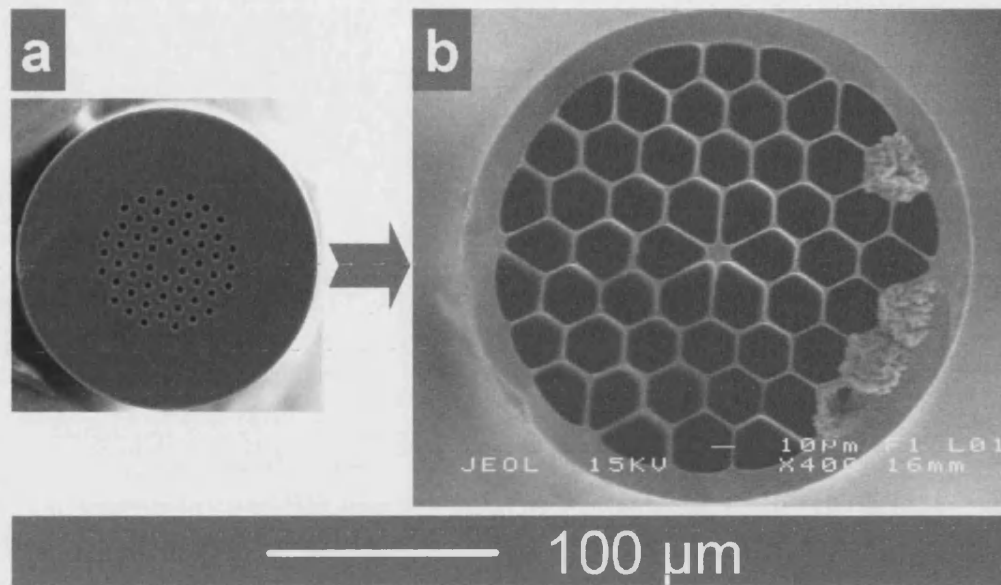


Fig. 5.5. SEMs of (a) the original 12  $\mu\text{m}$  core ESM PCF (b) the same PCF inflated at pressure of 10 bar.

SEMs of this fibre before and after inflation are shown in Fig. 5.5. The maximum OD obtained during experiments exceeded 400  $\mu\text{m}$  in some occasions, more than 3 times that of the un-inflated fibre.

#### 5.4.2. Hole Inflation and Tapering to Small-Core PCFs

Once a large-hole PCF has been made in this way, I then conventionally tapered the inflated section in a standard 'fast and cold' process to yield 100 mm long waists with core diameters of 1.1, 1.6 and 1.9  $\mu\text{m}$ . The fibres were pressurised at 10 bar during this process so there is some further hole inflation, although the fibre is not processed hot enough or slowly enough to allow the holes to deform greatly. SEMs of these fibres are shown in Fig. 5.6. The scale reduction during tapering is shown by the bottom row of Fig. 5.6 which shows the tapered fibre at the same scale as the initial and inflated fibres.

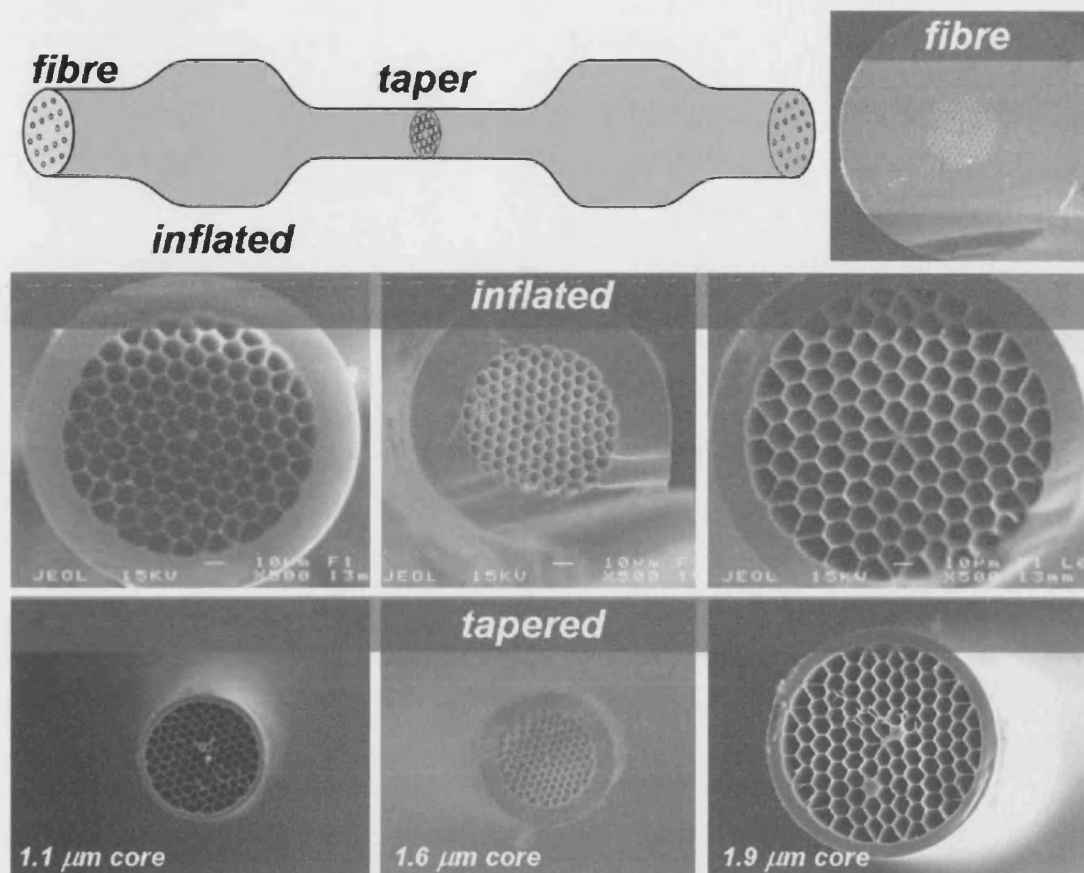


Fig. 5.6. SEM images of the inflated and tapered fibres. (top) initial 5  $\mu\text{m}$  core ESM PCF, (middle) inflated PCF and (bottom) tapered inflated PCF. All pictures to the same scale. Left to Right; Final taper core diameters 1.1, 1.6, 1.9  $\mu\text{m}$  respectively.

Parameters of the inflated and tapered fibres are given in table 2. Note that although the area of glass in the cross-section of the tapered fibre with 1.9  $\mu\text{m}$  core has been reduced by a factor of 3.7 by tapering, the final diameter is almost the same as the initial diameter. Therefore the absolute hole diameters in the tapered sections are all larger than in the initial fibre (holes in tapered fibre with 1.1  $\mu\text{m}$  core would be as small as 0.37  $\mu\text{m}$  without inflation or collapse). The measured optical losses at 1550 nm for this second tapering stage ranged from 0.05 to 0.3 dB. The insertion loss of the entire structure (from initial ESM PCF to inflated PCF to small-core PCF, and back) was less than 0.4 dB for the 1.9 and 1.6  $\mu\text{m}$  core samples, but was high for 1.1  $\mu\text{m}$  core samples. For a 1.1  $\mu\text{m}$  core diameter, the core is smaller than the measurement wavelength, so guidance may be expected to be weak. I note that the loss from mode mismatch if the

untreated fibre was simply butted or spliced to 2  $\mu\text{m}$  core high air filling fraction PCF would be at least 5 dB per junction.

Table 5.2: Parameters for the inflated and tapered fibres shown in Fig. 5.6.

Fig. 5.6		Total Elongation	OD ( $\mu\text{m}$ )	$d_{\text{core}}$ ( $\mu\text{m}$ )	$d$ ( $\mu\text{m}$ )	$\Lambda$ ( $\mu\text{m}$ )	Loss (dB)
1.1 $\mu\text{m}$ taper	Inflated fibre	1.18 (125-115 $\mu\text{m}$ )	165	3.5	10.4	10.8	0.27
	taper	14.3 (125-33 $\mu\text{m}$ )	65	1.1	4.9	5.1	--
1.6 $\mu\text{m}$ taper	Inflated fibre	1.18 (125-115 $\mu\text{m}$ )	132	3.6	6.3	6.6	0.075
	taper	5.2 (125-55 $\mu\text{m}$ )	69	1.6	3.7	3.9	0.30
1.9 $\mu\text{m}$ taper	Inflated fibre	1.18 (125-115 $\mu\text{m}$ )	192	3.6	12.6	12.7	0.28
	taper	3.7 (125-65 $\mu\text{m}$ )	119	1.9	8.5	8.6	0.06

### 5.4.3. Nonlinear Application

The structures described in the previous section have final waist sections similar to highly nonlinear PCFs and fibre tapers used for supercontinuum generation [Ranka 00, Birks 00, Coen 01], but with some advantages over both. The waist is a PCF so the dispersion can be tuned by using different air hole sizes as well as by altering the core diameter (as shown in Chapter 4). In this device the input and output pigtailed are single-mode fibres with a relatively large core diameter, and the waist is a PCF so the guided mode is enclosed and protected. A similar effect was achieved in a pioneering experiment by Chandalia et al. [Chandalia 01] where an otherwise conventional step-index fibre had large holes in the cladding, which were used to confine the light when the fibre was tapered. Ours structures have the additional advantage that the PCF pigtailed are close to being endlessly single mode, so they guide the whole continuum

output in a robust single mode, whereas a conventional step-index core is unlikely to be single-mode and low loss over an octave or more in frequency.

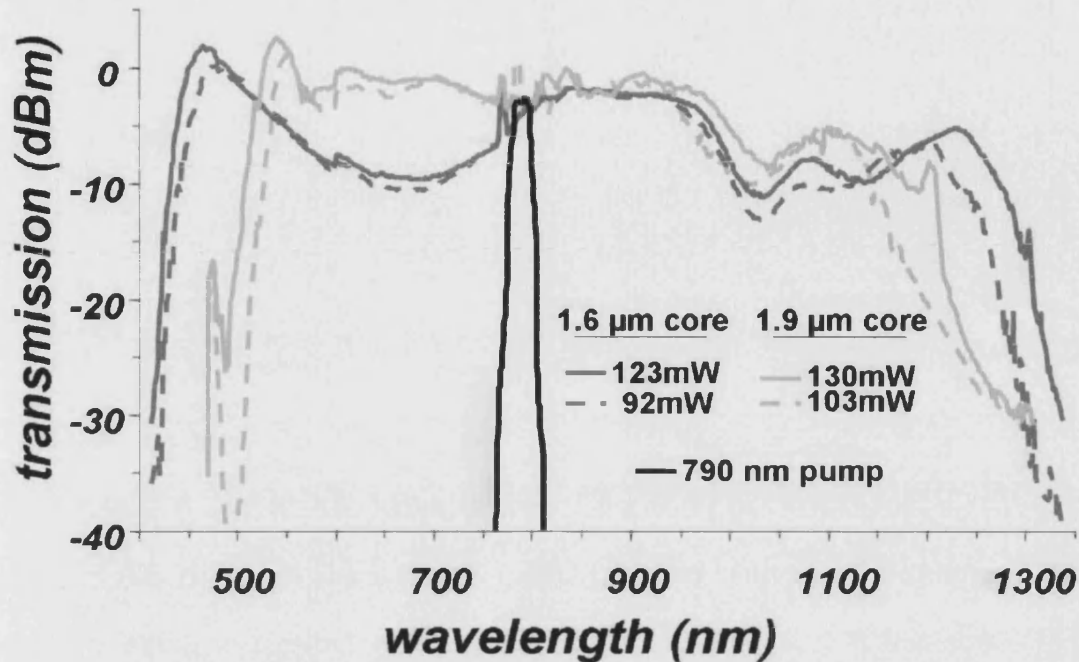


Fig. 5.7. Supercontinuum spectra for inflated fibres. For the tapered core diameter of 1.6  $\mu\text{m}$  and coupled power of 123 and 92 mW, and the tapered core diameter of 1.9  $\mu\text{m}$  and coupled power of 130 and 103 mW.

Fig. 5.7 shows the SC spectra produced by devices with a 1.6 and 1.9  $\mu\text{m}$  core diameters in the waist when pumped with a fs Ti:sapphire laser (790 nm, pulse duration 200 fs, repetition rate 75 MHz) with 100 mW average power coupled into the fibre. The input pigtail was cut to 6 cm length to avoid pulse broadening by the chromatic dispersion of the fibre before the tapered section. The output SC is naturally in the fundamental fibre mode. The extent of the SC is as expected from previous experiments with similar active structures [Ranka 00, Birks 00, Wadsworth 02].

### 5.5. Core Shape Transitions

Here I describe an adaptation of the inflation technique whereby one or more of the holes at the end of the fibre is blocked before pressure is applied [Witkowska 05].

Where the fibre is heated any unpressurised hole will collapse as its neighbours expand, leaving a region of solid silica in the fibre's cross-section. This idea is demonstrated by blocking one of the holes next to the core of an endlessly single-mode PCF. Collapse of this hole adds solid material to the side of the fibre's core to give it a pronounced elliptical aspect ratio and hence form-birefringence, which can be enhanced by tapering the core down in size.

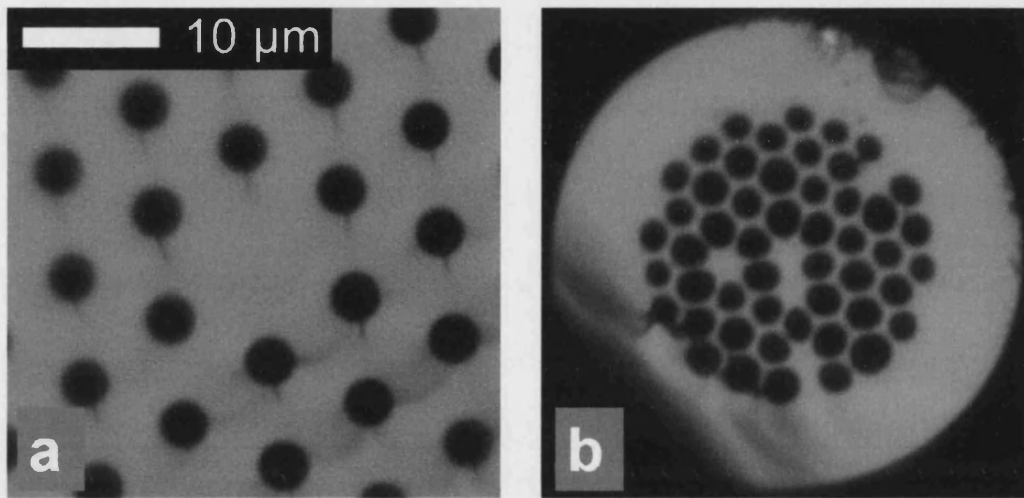


Fig. 5.8. The PCF (a) before and (b) after inflation and tapering with one hole blocked next to the core.

The 12  $\mu\text{m}$  endlessly single-mode PCF fibre used for this experiment had a non-birefringent "circular" core. At one end of the fibre, one of the holes next to the core was sealed with glue. The glue was dispensed with a microscopically-positioned tip, and cured with UV light. The fibre was pressurized at 5.3 bar and the inflation of the fibre was made at the same time than tapering by a ratio of 4:1. All the holes were pressurised, except the one sealed at both ends blocked with glue, which remained at atmospheric pressure.

The tapered waist was then cleaved, leaving a 3 cm transition between around 1 m of the original (input) fibre at one end and 9 cm of inflated-and-tapered (output) fibre at the other end. Fig. 5.8 shows optical micrographs of the cleaved waist, together with the original fibre to the same scale as the tapered fibre. The pressurised holes inflated as

described in previous sections, but the unpressurised hole collapsed completely instead. The "circular" core at the centre of the original fibre of Fig. 5.8(a) has reduced in size by the tapering and become "elliptical" by the addition of solid material from the collapse of the adjacent hole. The dimensions of the core are now roughly  $4.6 \times 2.1 \mu\text{m}$ , an aspect ratio exceeding 2:1. (It can be seen that 3 other holes also collapsed, unintentionally, forming new cores in the fibre. However, they were well-enough isolated to have no observable effect on propagation in the central core. Water condensation on the fibre end face before the experiment was observed, it being a particularly humid day in a lab without air conditioning, and this probably caused the holes to be blocked).

### 5.5.1. Optical Measurements

Fig. 5.9(a) and (b) are near-field images of the output for 1430 nm light at the input, showing a fundamental mode pattern even though the core is almost certainly multimode. There is no detectable light anywhere except in the central core. In particular, there is no light in the parasitic cores. The transition loss of the structure was measured by the cut-back technique to be  $<0.4$  dB at 1550 nm wavelength.

To characterise the birefringence of the output fibre, polarisation beating with wavelength was recorded by launching polarised light from a broadband source into the input fibre, and passing the output light to an optical spectrum analyser via a polariser at 45 degrees to the optical axes of the fibre. Fig. 5.9(c) is the output spectrum.

The spectral beat period  $\Delta\lambda$  is related to the beatlength  $L_B$  and the fibre length  $L$  by [Ortigosa-Blanch 00]

$$L_B = \frac{\Delta\lambda}{\lambda} L \left[ \frac{\lambda}{L_B} \frac{dL_B}{d\lambda} \right] \quad \text{Equation (5.4)}$$



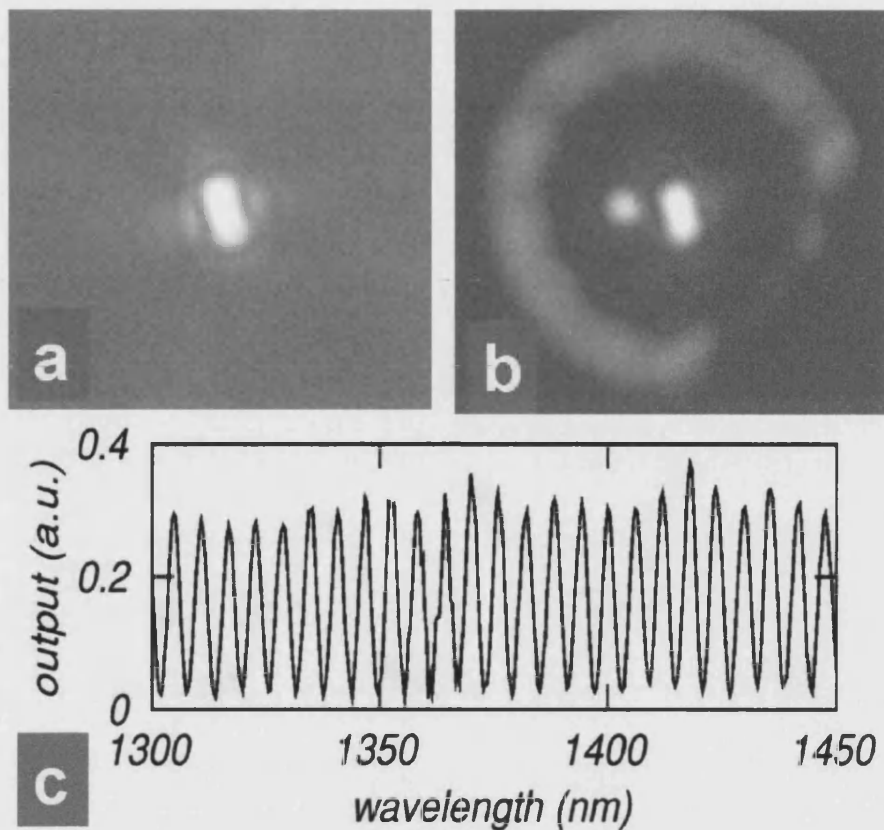


Fig. 5.9. Near-field images at the output (a) with the input fibre present, and (b) with the input fibre removed and a defocused launch so that the cladding features were illuminated for comparison. (c) Measured polarisation beating.

The factor in brackets is of order unity [Ortigosa-Blanch 00], so since the output fibre was 9 cm long and  $\Lambda\lambda = 5.95$  nm from Fig. 5.9(c), the equation gives an estimate for the beatlength of approximately 390  $\mu\text{m}$ . This compares well with the value of 280  $\mu\text{m}$  calculated for a  $4.6 \times 2.1$   $\mu\text{m}$  rectangular silica core in air [Snyder 86]. (This value is highly sensitive to the dimensions, which can be only imperfectly known from the optical micrograph of the fibre.) Repeating the measurement with the input fibre alone confirmed that it did not contribute significantly to the birefringence. The simple periodic form of Fig. 5.9(c) indicates that the output was in a single mode. If more than one mode had been excited to a significant extent, its different birefringence would result in a more complicated beating spectrum.

## 5.6. Conclusion

For the first time, the thermal post-processing of a stock single-mode PCF to form a transition to a cobweb-type PCF structure with a smaller core but larger air filling fraction have been demonstrated [Wadsworth 05]. In the first stage of the process, the fibre is processed 'slow and hot' while the holes are pressurised at several bar to inflate the holes without reducing the cross-sectional area of glass by much. In the second stage, the inflated section is tapered conventionally 'fast and cold' to reduce the core size without significantly changing the structure. The insertion loss of complete structures is less than 0.4 dB, and the simplicity of the input and output coupling in a supercontinuum generation experiment have been demonstrated. A 3 cm low-loss taper transition in a PCF was made, where the core shape changes from "circular" (6-fold rotational symmetry) and non-birefringent to "elliptical" (2-fold rotation symmetry or less) with an aspect ratio exceeding 2:1 and a very short birefringence beat length of about half a millimetre. The insertion loss of <0.4 dB was low, and the transition was made from widely-available stock PCF by a simple tapering technique.

---

# Chapter 6

## Interfacing SMFs to PCFs: The “Ferrule” Idea

Recent work focuses on the need to interface PCFs with standard single-mode fibres as well as with light sources. In previous chapters I have described the interfacing between large core PCFs and small core PCFs. Since large ESM PCFs can be mode matched to SMFs for splicing (eg. 12  $\mu\text{m}$  core ESM PCF and Corning SMF-28), a relatively low loss transition can be achieved between those fibres. However the need for splicing, the limitation in length and the restriction to certain types of PCFs limits the scope of those interfacing techniques. Here I illustrate a technique for interfacing SMFs to PCFs with low loss and no need for splicing. It can be used, in principle, to interface index-guiding silica PCFs of almost any design, if they can be drawn from preforms. During the fabrication of the PCF preform it is straightforward to introduce a new design in the structure, simply by replacing tubes with rods or vice versa in the stack. By adapting the fabrication technique a low-loss adiabatic transition between SMFs and PCFs will be demonstrated [Leon-Saval 05a].

### 6.1. Ferrule Transition Idea

In contrast to the interfacing method described in Chapter 5, this is not a post processing technique but an enhancement of the PCF fabrication process. The idea is to make a PCF preform (which is called a ferrule) in which the core has been omitted leaving a void where a standard SMF will be threaded. The SMF will replace the core of a normal PCF preform. A PCF can be drawn from one end of the ferrule. The core of the PCF is formed by the tapered down SMF. The neck down region in the furnace is a transition between the SMF and the PCF (see Fig. 6.1).

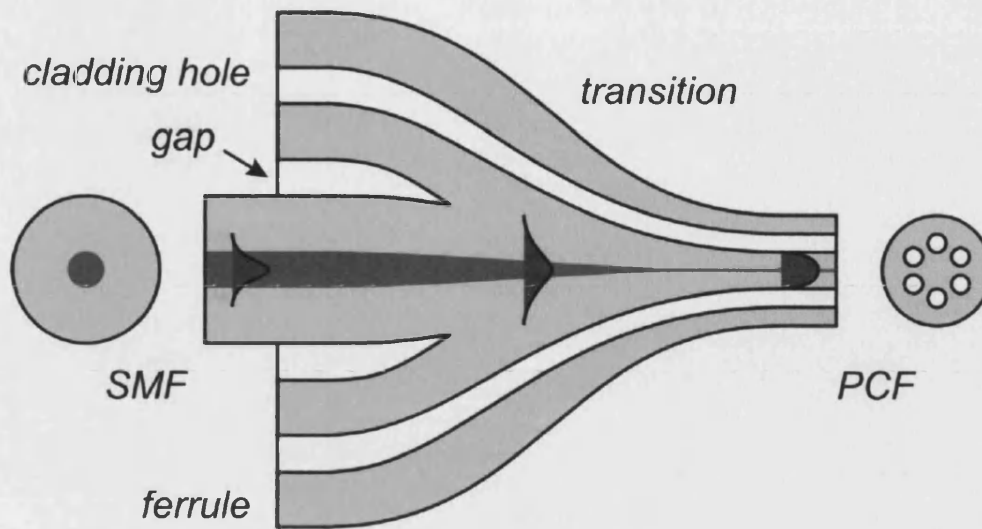


Fig. 6.1. Longitudinal section, showing how the mode spreads out from the tapered SMF core to become guided by the surrounding PCF core.

Optically this transition is like a conventionally tapered SMF [Jedrzejewski 86]. The SMF is tapered down inside the ferrule when drawn, the final PCF core being like an SMF taper waist but supported by a holey PCF cladding structure instead of being suspended in air. As light propagates into the transition the fundamental mode spreads out from the diminishing SMF core to become guided by the much-larger PCF core, without the need for splicing, as shown in Fig. 6.1. For the transition to be low loss it needs only to be gradual enough to be adiabatic. This is a well-understood and easily satisfied requirement [Love 86].

## 6.2. Experimental Technique

The process is adapted from the fabrication of PCFs from stacked tubes and rods and is depicted schematically in Fig. 6.2. A PCF preform is constructed in the usual way but, instead of placing a solid rod in a stack of silica tubes, the central site is left empty with neither a rod nor a tube (Fig. 6.2 (a)).

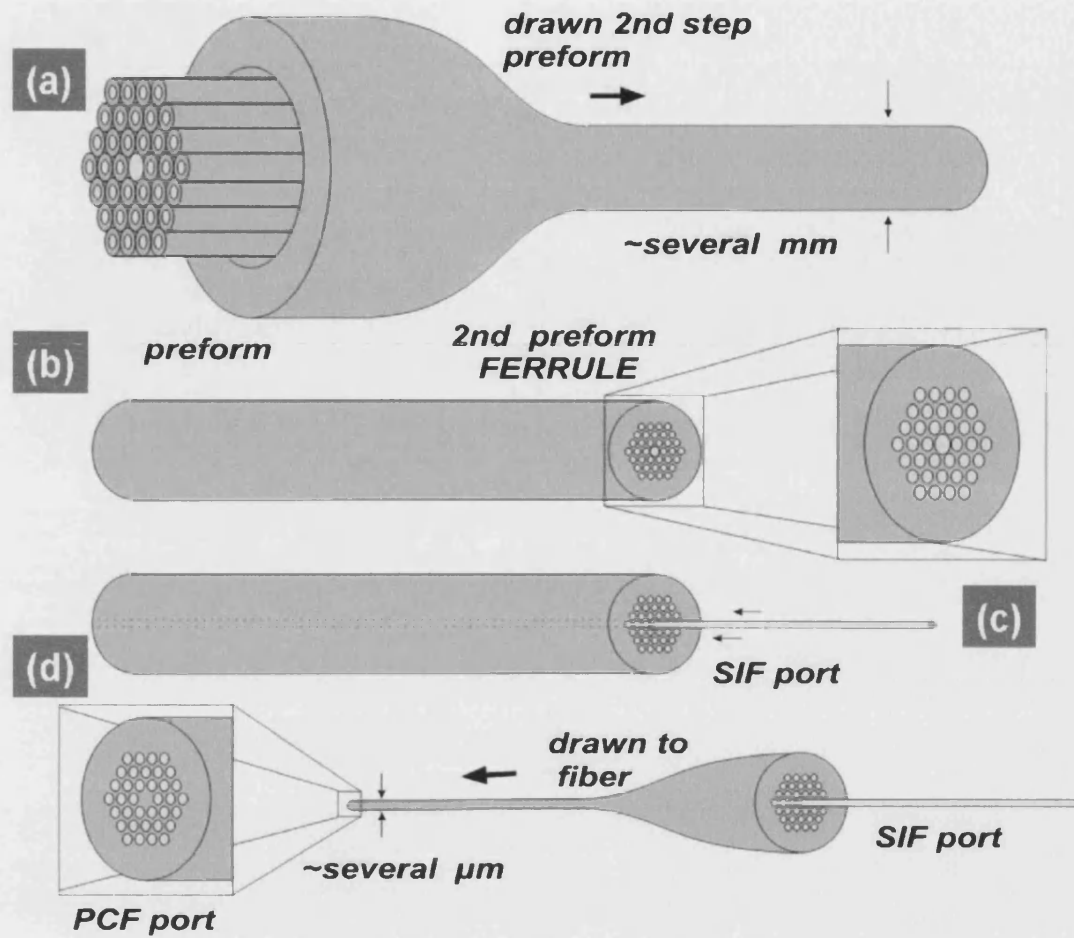


Fig. 6.2. Schematic diagram of the ferrule fabrication process.

The ferrule is drawn from the stack so that the central void is more than  $125\ \mu\text{m}$  across—big enough to fit an SMF inside [Fig. 6.2 (b)]. A length of SMF is threaded into this void [Fig. 6.2 (c)]. The coating of the fibre is stripped and the bare fibre is cleaned with acetone to eliminate remaining impurities. All the process is carried out in a clean environment inside a cabinet with a constant airflow in order to prevent contamination. Threading the SMF is the most difficult task in the whole process. The uncoated SMF is easy to break while pushing to overcome static and friction forces while threading it inside the void.

One end of the filled ferrule is then drawn in the usual way into a length of PCF which core incorporates the drawn-down SMF [Fig. 6.2(d)]. An important goal in this

drawing process is to collapse the gap between the SMF and the ferrule. All the cladding holes of the PCF ferrule structure are blocked with glue except the central void where the SMF is threaded. The gluing process is made under an optical microscope using the tip of a syringe needle to apply the glue. Then vacuum is applied to the gap between the SMF and the ferrule while drawing the whole structure down to fibre. Normally the  $d/\Lambda$  of the final PCF is considerably bigger than in the preform. This is because the blocked cladding holes are pressurised by the hot air trapped inside. The increase of the hole size along the transition is often beneficial for the transformation of the mode field diameter [Birks 02].

However, drawing is deliberately stopped after a few meters of PCF have been drawn, and the undrawn remainder of the ferrule and the neck-down region joining it to the PCF are preserved. As a result, the PCF is connected via a continuous transition to the SMF pigtail protruding from the undrawn end of the ferrule, as shown in Fig. 6.2 (d). As the drawing of the PCF is entirely conventional, its properties can be tailored as it is being drawn. For example, the shapes and sizes of the core and the holes can be adjusted via the drawing speed, furnace temperature, pressurization, evacuation, or any of the other techniques at the fabricator's disposal.

An important factor to take into account is the point where the SMF gets fused together with the ferrule structure. A transition made using a ferrule with  $d/\Lambda=0.20$  was sliced every mm or so and the cross-sections were photographed. Fig. 6.3 shows different cross-sections of a ferrule transition from a starting structure with an OD 2.86 mm and  $d/\Lambda=0.20$  (a) to a point in the transition with an OD 1.38 mm and  $d/\Lambda=0.35$  (d). This ferrule has a fabrication defect as the glue did not block four holes around the core and these holes tended to collapse unintentionally. However, the photos do illustrate when the SMF-ferrule gap disappears. The gap disappeared completely when the ferrule transition OD was around 1.38 mm and possibly slightly before.

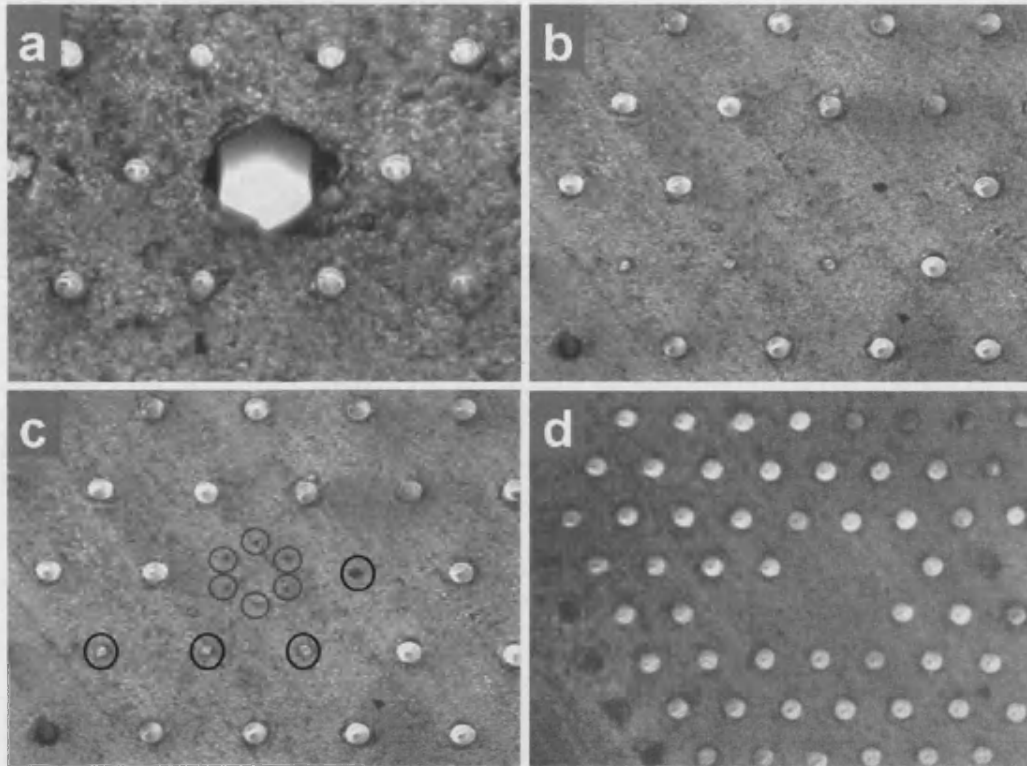


Fig. 6.3. Optical photographs of (a) starting structure OD=2.86 mm; (b) and (c) ferrule transition at a point with OD= 2.05 mm, without and with circles marking the gaps between the SMF and the preform (grey) and the unblocked holes (black) respectively; (d) at a point in the transition with OD=1.38 mm, showing the complete collapse of the gaps.

The outer diameter of the SMF at the joining point was estimated to be around 60  $\mu\text{m}$ . Since the SMF-28 core guides light until its outer diameter is about 20 to 50  $\mu\text{m}$  (depending on the wavelength), when the light escapes from the core the light 'sees' a PCF structure without the gap. Therefore the light never sees the gap between the SMF and ferrule structure.

### 6.2.1. Endlessly Single-Mode PCFs

I illustrated the method by interfacing a conventional fibre (Corning SMF-28) to an endlessly single-mode PCF [Leon-Saval 05a]. The ferrule shown in Fig. 6.4(a) was drawn from a stack of silica tubes as described earlier to consolidate the interstitial holes

between the tubes. A length of SMF-28 was stripped of its polymer coating, thoroughly cleaned, and threaded into the ferrule's large central void [Fig. 6.4(b)].

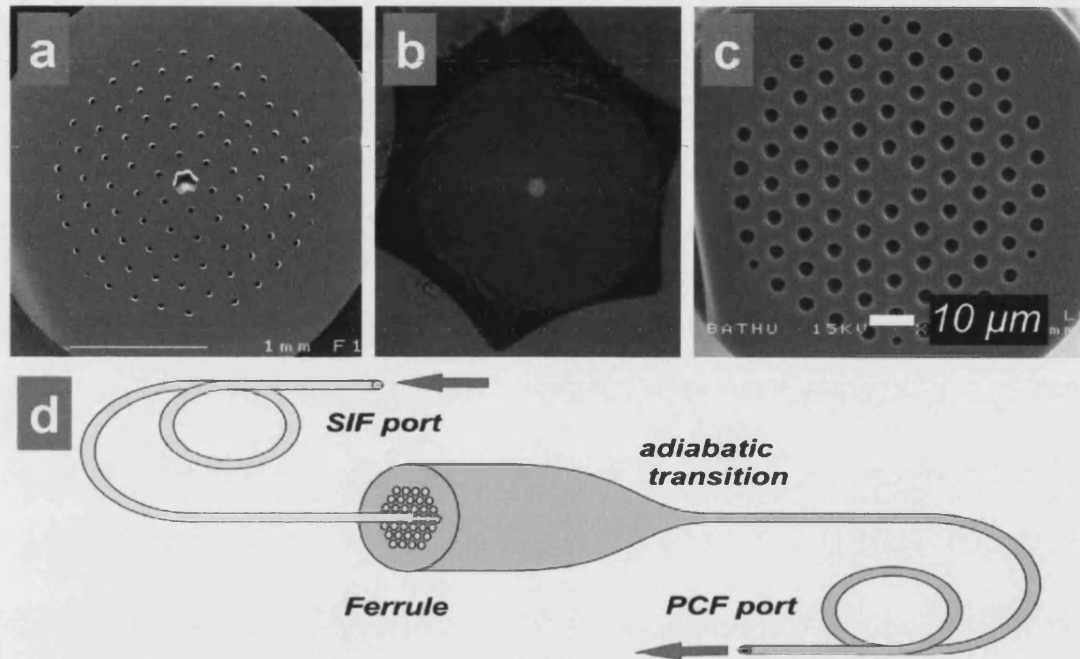


Fig. 6.4. (a) SEM of a 2.86 mm diameter ferrule. (b) Optical micrograph of the central void in such a ferrule containing a 125 μm diameter SMF-28. (c) SEM of the endlessly single-mode solid-core PCF drawn from the ferrule. (d) Schematic drawn of a ferrule interfacing device.

The filled ferrule was then drawn to fibre while the cladding holes were pressurized. The gap around the SMF was evacuated to ensure that the former stayed open whilst the latter collapsed, giving the 110 μm diameter PCF shown in Fig. 6.5(c). The solid core of the PCF was made from the entire cross section of the SMF and some material from the ferrule around the void. It was 10 μm across, surrounded by five rings of holes with a pitch  $\Lambda=7.5$  μm and relative diameter  $d/\Lambda=0.41$ . Data for the transmission loss was obtained by a direct cut-back measurement. The loss of the transition from SMF to PCF was 0.6 dB at the wavelength of 1550 nm.



### 6.2.2. Highly Nonlinear PCFs

Interfacing of highly nonlinear PCFs is more challenging by previous methods but just as simple by ours. In this ferrule the ordinary cladding holes were big enough ( $380\ \mu\text{m}$  across) for one of them to serve as the void without being made bigger than the others; see Figs. 6.5(a) and 6.5(b). Indeed the void was big enough to allow the SMF-28 to remain coated for a short distance into the ferrule at the undrawn end, making it much less likely to break where it emerged from the ferrule. The  $140\ \mu\text{m}$  diameter PCF drawn from the ferrule had a cobweb cladding structure supporting a core of  $2.8\ \mu\text{m}$  diameter [Fig. 6.5(c)]. The loss of the transition was less than  $0.8\ \text{dB}$  at  $633\ \text{nm}$  [Leon-Saval 05a].

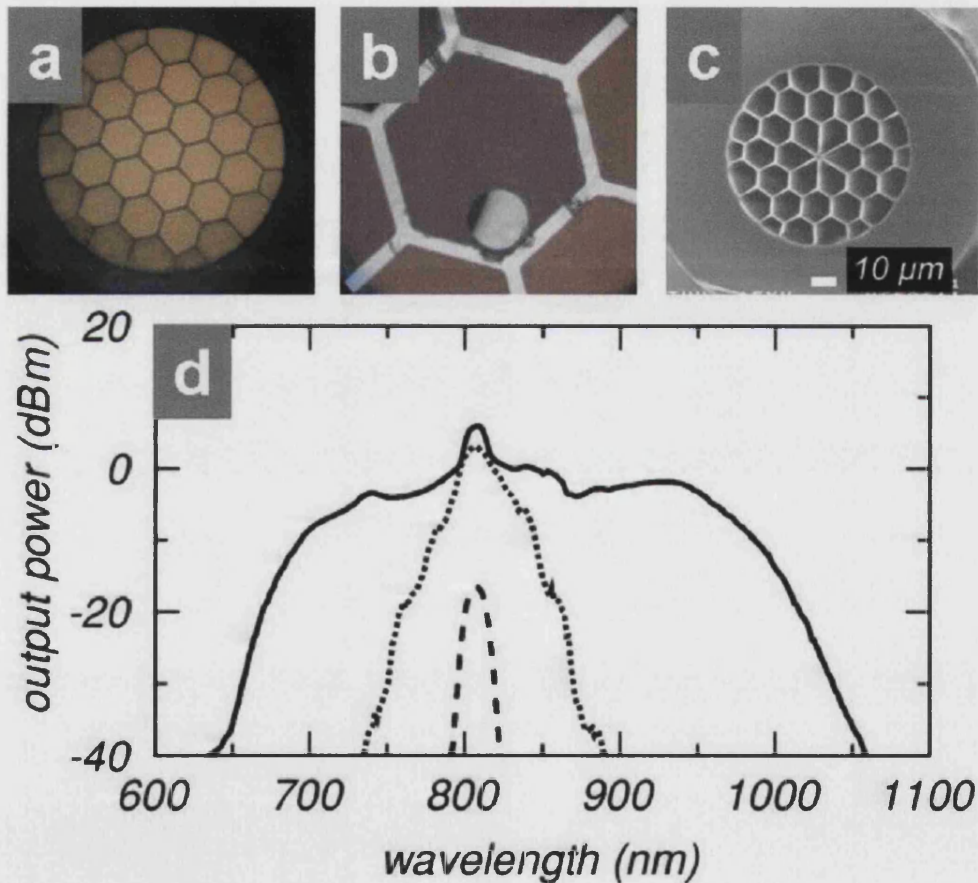


Fig. 6.6. (a) Optical photograph of a high air-filling-fraction ferrule. Each hole is  $380\ \mu\text{m}$  across flats. (b) Optical photograph of one of the holes containing a SMF. (c) SEM of a highly nonlinear PCF with a  $2.8\ \mu\text{m}$  core drawn from the ferrule. (d) Supercontinuum spectra at the output of the PCF when femtosecond pulses were coupled into the SMF-28. The average output powers were  $0.03$ ,  $5$ , and  $21\ \text{mW}$  (dashed, dotted, and solid curves, respectively) as estimated by integrating the curves.

Figure 6.6(d) shows broadened spectra measured at the output of 1 m of the PCF when 810 nm femtosecond pulses from a mode-locked Ti:sapphire laser were coupled into the SMF. Although dispersion in the input fibre (80 cm long) would have lengthened the pulses considerably and so reduced their peak power, a broad supercontinuum [Ranka 00] nevertheless developed as the pulse energy was increased.

Another ferrule transition was attempted in order to match commercially available highly nonlinear PCFs. This ferrule had five periods of cladding holes, a lower air-filling fraction, and the central void was 145  $\mu\text{m}$  across [Fig. 6.6(a)]. A length of SMF-28 is threaded inside and a 160  $\mu\text{m}$  diameter highly nonlinear PCF was drawn from one end of the ferrule [Fig. 6.6(b)].

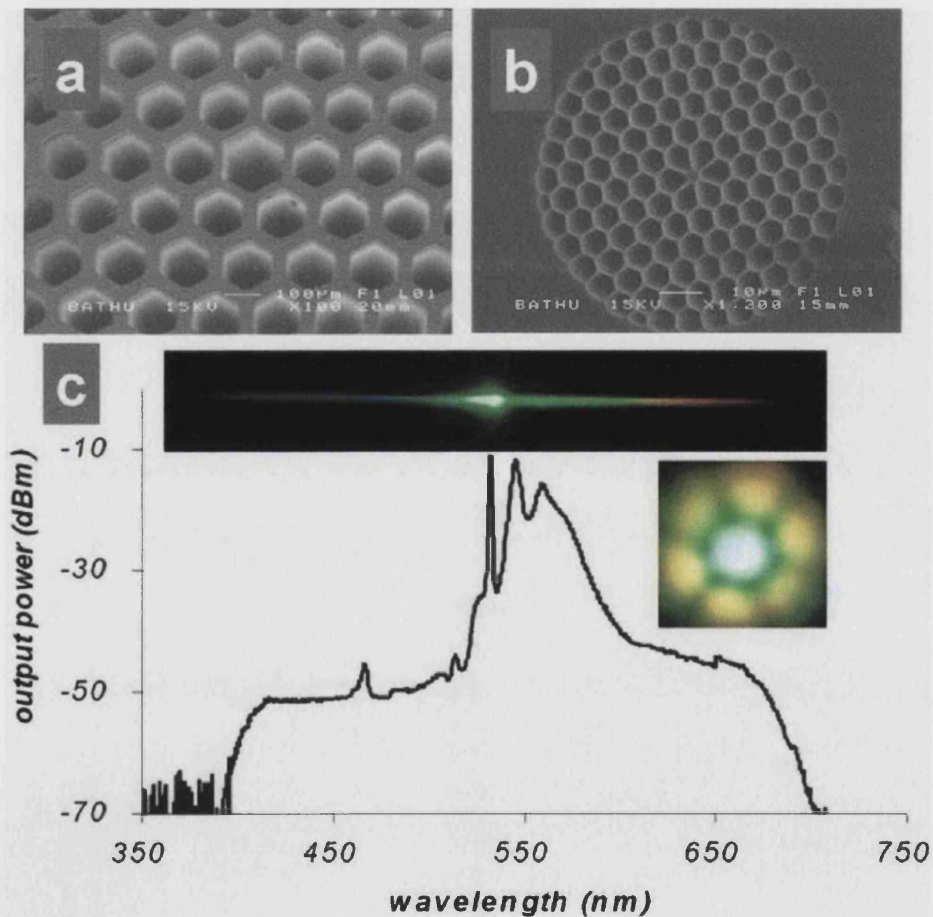


Fig. 6.7. (a) SEM of the ferrule. Central hole is 145  $\mu\text{m}$  across flats. (b) SEM of a highly nonlinear PCF with a 2.6  $\mu\text{m}$  core drawn from the ferrule. (c) SC spectra at the output of the PCF when 532 nm nanosecond pulses were coupled into the SMF-28. (c) insets: (bottom) measured far field image at the PCF output of the high-order modes SC, (top) SC spectra near field image dispersed by a grating and projected onto a piece of paper.

Fig. 6.7(c) shows visible broadened spectra measured at the output of 90 cm of the PCF when 532 nm nanosecond pulses from a doubled frequency Q-switched Nd:YAG laser was coupled into the SMF. I observed light of new wavelengths in high order modes being generated [Fig. 6.7 (bottom inset in c)]. The PCF was strongly multimode at visible and near infrared wavelengths. This leads to a number of high-order phase matching processes. The broadening of the spectrum can be explained by intermodally phase-matched nonlinear processes [Efimov 03].

### 6.3. Conclusion

A new method for interfacing SMFs and PCFs has been demonstrated. The 0.6-0.8 dB measured losses were not fundamental in origin and should be reducible by optimising the lengths and profiles of the transitions. This optimisation is an already well-known technique for tapered SMFs and PCFs. The method is versatile, being capable of interfacing most types of PCF and requiring no splices. By way of example, I have coupled light efficiently into an endlessly single-mode PCF and into highly nonlinear PCFs. In the next chapter I will exploit the versatility of this technique by interfacing between multiple SMFs and PCF.

---

# Chapter 7

## Using Ferrules to Interface More than One SMF to One PCF

In Chapter 6 I described the ferrule transitions to interface one SMF to a single core PCF. However the versatility of this technique allows it to be used to interface more than one SMF to a single PCF. Here in this chapter I will describe three very different ways of using ferrule transitions with more than one SMF.

### 7.1. Multicore PCF

In this section I will describe how a ferrule transition is used to interface an SMF to each core of a multicore fibre. A multicore fibre is simply a fibre with more than core within the fibre. Multicore fibres (conventional step-index or PCF) have been studied widely [Schiffner 80, Jensen 82, Mangan 00]. Such multicore fibres have many possible applications, but a problem arises when trying to address cores individually without cross-talk of light from one core to another. Although some solutions do exist (eg. if core are widely separated [Flockhart 03]), none of them is generally applicable. Here I describe how by making a ferrule with more than one void, each of which accepts an SMF, a transition between a multicore PCF and multiple SMFs (corresponding to each core of the PCF) can be formed [Leon-Saval 05a].

### 7.1.1. Experiment: Two-Core PCF

Two tubes were omitted from a stack to make a 5.45 mm diameter ferrule with two voids [Fig. 7.1(a)]. Each void was approximately 300  $\mu\text{m}$  across. An SMF was threaded into each void [Fig. 7.1(b)]. The voids were big enough for a couple of cm of coated SMF to fit inside to prevent it breaking when bending. The 110  $\mu\text{m}$  diameter two-core PCF of Fig. 7.1(c) was drawn from the ferrule. The PCF cores were 7  $\mu\text{m}$  in diameter and well separated by 34  $\mu\text{m}$ , though there is no fundamental reason why they could not be made close enough to be optically coupled if desired.

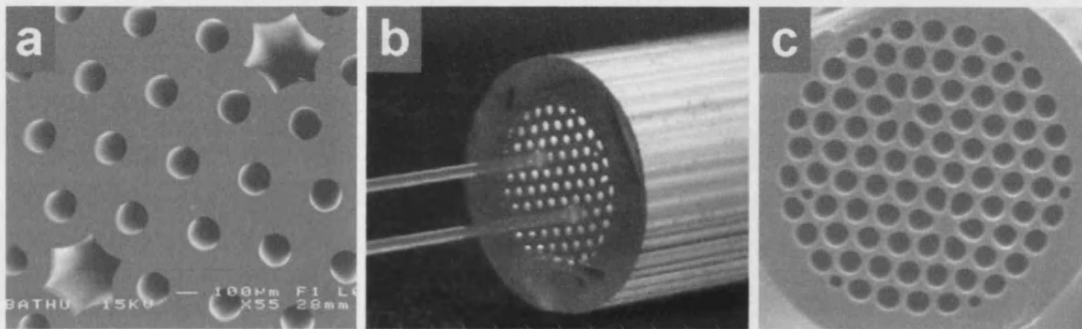


Fig. 7.1. (a) SEM of the voids (separated by 1.5 mm) in a two-core ferrule. (b) Photograph of the undrawn end of the ferrule containing two SMFs. (c) SEM of the drawn 110  $\mu\text{m}$  diameter two-core PCF.

Because each PCF core is linked via an adiabatic transition to a separate SMF pigtail, each PCF core can be individually addressed without cross talk to the other. Figure 7.2(a)–(c) shows the near field image at the output of the PCF when infrared light at 1550 nm is launched independently into the SMFs. As expected no cross talk was visible when light was launched into only one SMF, only the corresponding PCF core was illuminated [Fig. 7.2(b) and (c)]. To measure the cross talk a photodiode was scanned across the near field image whilst the light was launched into each core alone in turn. The results plotted in Figure 7.2(d) show that no light could be detected from the other core. The dynamic range of my measurements gave an upper bound of  $-34$  dB for the cross talk, simply by taking into account the minimum power detectable for the photodiode and the maximum power detected in each core. Any cross talk that would have occurred if the cores were a lot closer together would have been due to

directional coupling in the fibre rather than imperfect input coupling. The losses of the transitions (using a direct cut back measurement) to the cores were 0.6 and 0.8 dB at 1550 nm.

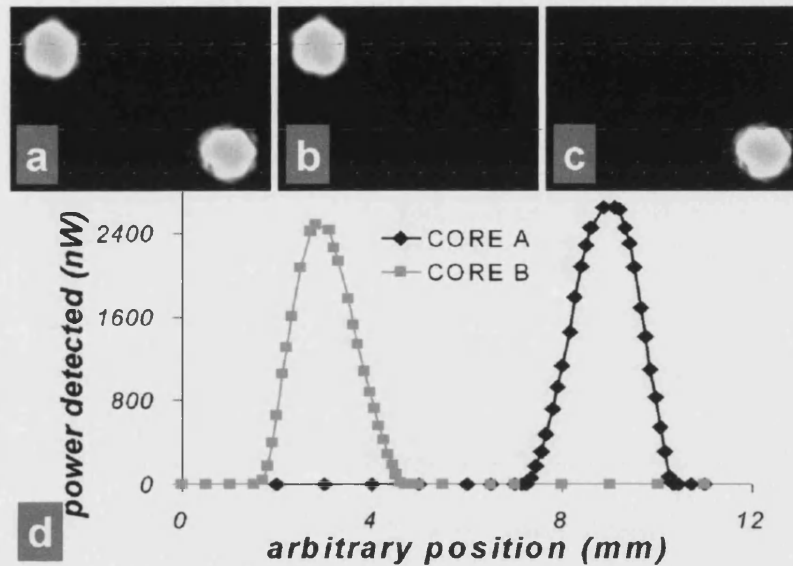


Fig. 7.2. (a)-(c) Near field images at the output of the PCF for light coupled into both SMFs then each SMF alone in turn. (d) Graph showing detected power of the near field at the output of the PCF whilst scanning a photodiode across the horizontal axis of the PCF cores (coupling the light into each SMF alone in turn).

To my belief this is the first method capable of coupling light without input cross talk into individual closely spaced cores of multicore fibres, and should allow multicore fibre devices to approach their theoretical performance for the first time.

## 7.2. Fibre Mode Convertor

This section describes a ferrule transition between two SMFs and a single PCF core, in which the resulting device acts as a mode convertor [Leon-Saval 05b]. A fibre mode convertor is a device that couples light from one mode to another in the fibre. One application for such a mode convertor is for dispersion compensation. Here, the input light in the fundamental mode of a fibre is coupled to a higher-order mode with strong

normal dispersion, which propagates some distance before being converted back to the fundamental mode at the output [Poole 94, Gnauck 00]. The most widely-used mode convertor is a long-period grating with a period matching the beat length between the modes of interest. The grating resonantly couples light between the two modes [Ramachandran 02].

A good mode convertor will couple the modes with a high extinction ratio, which is the ratio between the power converted to the desired output mode and the residual power remaining in the input mode. It will also be spectrally broadband, so that light is coupled with a high extinction ratio over a wide range of wavelengths. However, the strength of a long-period grating must be closely controlled to give complete coupling between the modes. If the grating is even slightly too strong or too weak the modes will be over- or undercoupled, in both cases increasing the residual power in the input mode and reducing the extinction ratio. The grating is also a resonant device, giving complete conversion only over a narrow band of wavelengths. In contrast this ferrule-based mode convertor is not a resonant device so it is wavelength independent and has high extinction ratio without the need for fine tuning.

### 7.2.1. Principle of Operation

The proposed fibre mode convertor is based on a ferrule transition between a pair of dissimilar SMFs at one end and a PCF core at the other [Fig. 7.3(a)]. Optically this behaves like a PCF-version of a “null” fused coupler [Birks 94, Birks 96].

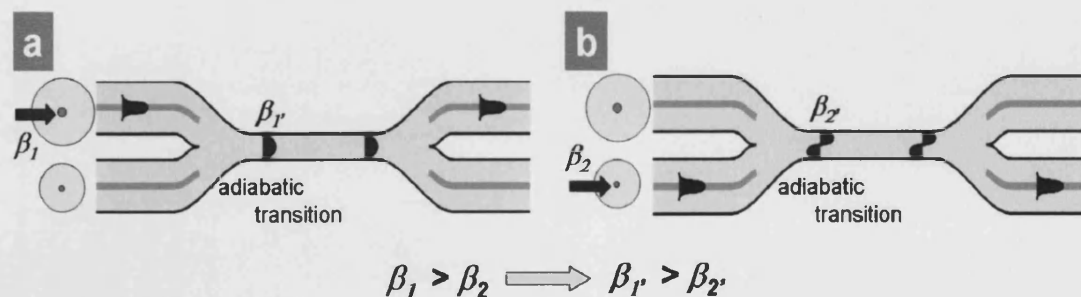


Fig. 7.3. Evolution of light through a “null” coupler when launched (a) into the larger fibre and (b) into the smaller fibre.

A null fused coupler is made by fusing together in parallel a pair of dissimilar fibres whilst tapering to form a common waist resembling that in a conventional taper. The fundamental mode of the larger fibre (with the higher propagation constant) evolves adiabatically into the fundamental mode of the composite waveguide of fused coupler waist [Fig. 7.3(a)]. The fundamental mode of the smaller fibre (with the smaller  $\beta$ ) evolves into the second mode of the waist [Fig. 7.3(b)].

The ferrule device is simply such a null coupler embedded in a PCF cladding and cleaved at its waist [Fig. 7.4(b)], so that light entering from the smaller fibre excites the second mode into the PCF. The mode convertor relies on adiabatic propagation rather than resonant coupling. The extinction ratio of the device is commensurate with the adiabaticity of the transition, and no fine tuning of the device is needed to achieve high extinction. Furthermore, the mode conversion is effective at all wavelengths (and indeed both polarizations).

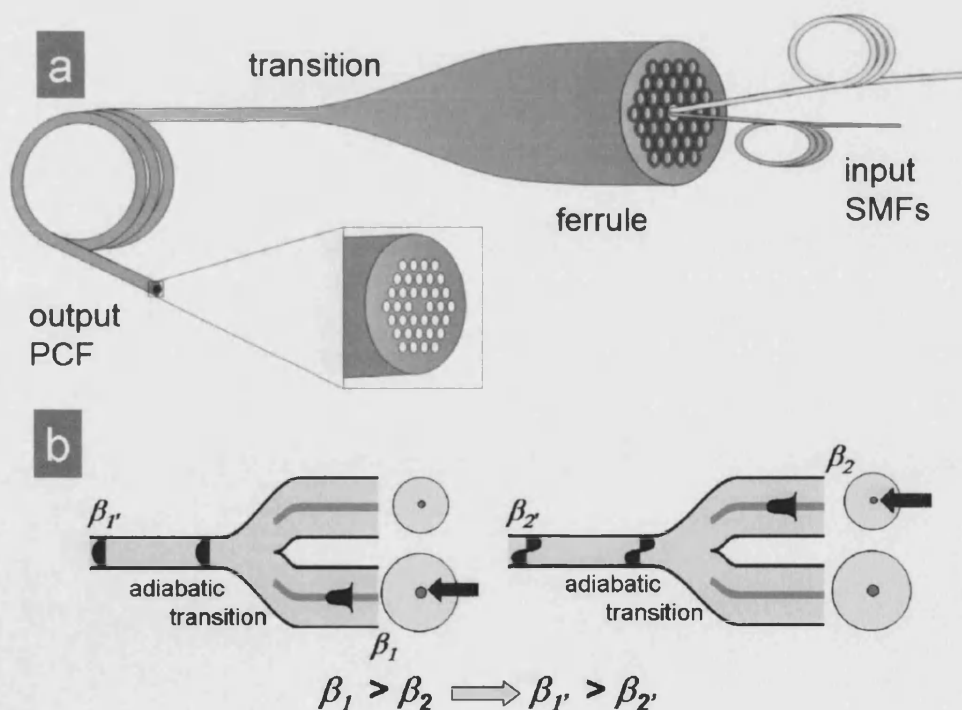


Fig. 7.4. (a) Schematic diagram of the construction of a ferrule transition between two dissimilar SMFs and a multimode PCF. (b) Schematic diagram showing the behaviour of the light propagating in a "null" coupler waist.



### 7.2.2. Experiment: $LP_{01}$ to $LP_{11}$ Mode Convertor

To make the mode convertor, a ferrule whose central void is big enough to accept two SMFs side-by-side was made [Fig. 7.4(a)]. The two SMFs were dissimilar; one (Corning SMF-28) has a 125- $\mu\text{m}$  outer diameter and a core with a cut-off wavelength of 1260 nm, while the other (Newport F-SBB) has an 80- $\mu\text{m}$  outer diameter and a core with a cut-off wavelength of 820 nm. The reason behind the choice of fibres is to make sure that the fundamental mode of the second fibre always has a lower propagation constant than that of the first fibre wherever they interact, whether it is guided as a core mode or a cladding mode. The core of the PCF drawn from this filled ferrule therefore will imitate the structure of a null coupler waist.

Fig. 7.5(a) is a SEM image of the 3.54 mm diameter ferrule, showing the large central void (around 350  $\mu\text{m}$  across) into which one of each of the SMFs was inserted. As the ferrule was drawn down to PCF the central void was evacuated while the cladding holes were pressurised, ensuring the latter stayed open while the former collapsed. Fig. 7.5(b) is a SEM image of the resulting 110  $\mu\text{m}$  diameter PCF. The final PCF had an elliptical core with axes of 10 and 8  $\mu\text{m}$ . The core was elliptical simply because was made from two SMFs side by side.

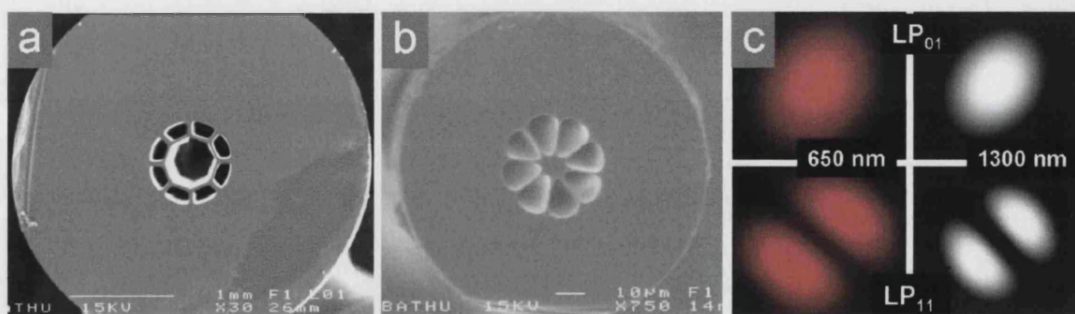


Fig. 7.5. SEMs of (a) the empty ferrule and (b) the final multimode PCF. (c) Measured far field patterns at the output PCF, for light of two wavelengths in the first (top) and the second (bottom) input SMFs.

Light from a microchip laser supercontinuum source [Wadsworth 04a] (using 10 nm band pass filters to select different wavelengths) was launched into each input SMF in turn and the far field emerging from the output PCF was imaged, Fig. 7.5(c), for

representative wavelengths of 650 nm and 1300 nm (as the PCF core was elliptical, with no more than two-fold rotation symmetry the second mode was LP-type instead of the set of vector modes that would be expected from a core with higher rotation symmetry [Birks 95a]). As expected, light entering the first SMF (with the greater propagation constant) excited a clear LP<sub>01</sub> mode in the PCF, whereas light entering the second SMF (with the lesser propagation constant) excited a clear LP<sub>11</sub> mode, irrespective of the wavelength of the input light. In particular, light entering the second SMF in its fundamental mode emerges from the PCF in its second mode, so the structure acts as a broadband mode convertor between these two modes. To determine the purity of the excited second mode, light from the supercontinuum source without band pass filters (with all wavelengths from 500 to 1750 nm [lower inset Fig. 7.6]) was launched into the second SMF. A two-lobed LP<sub>11</sub> pattern was observed in the far field at the output [upper inset Fig. 7.6]. An InGaAs photodiode sensitive to wavelengths from 750 to 1800 nm was scanned along the line joining the lobes of the pattern (marked as X-X' in the upper inset of Fig. 7.6) and the detected power is plotted as a function of position in Fig. 7.6.

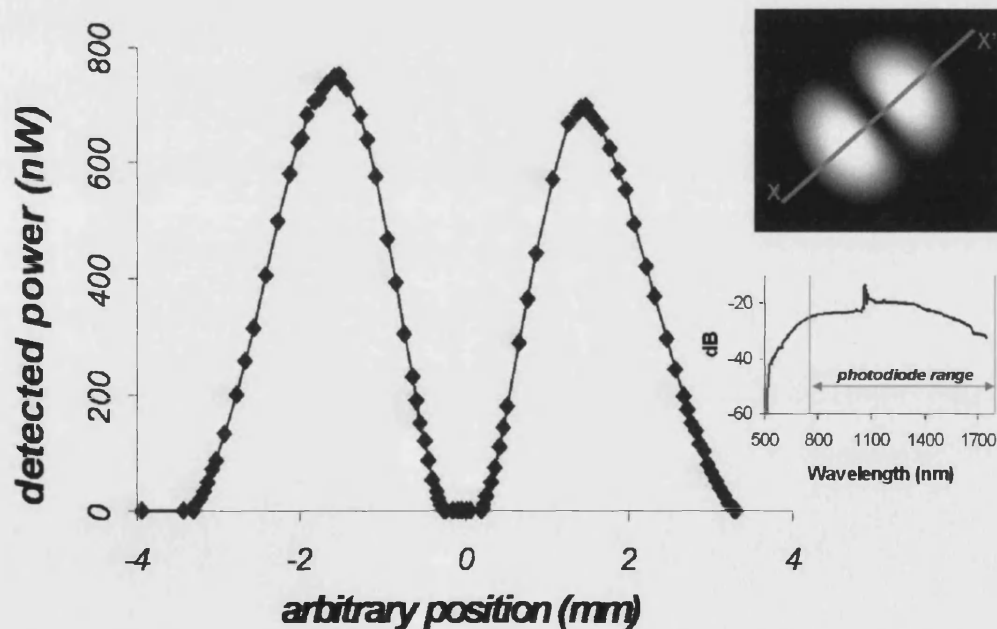


Fig. 7.6. Power detected by a photodiode scanned along the line X-X' across the LP<sub>11</sub> mode far field pattern (upper inset); (lower inset) the spectrum of the supercontinuum source and the photodiode response.

Any component in the  $LP_{01}$  mode at the output would be manifested as a non-zero detected power in the centre between the lobes. It was found that the power in the centre was too small to be detected by the photodiode. The ratio between the minimum detectable power and the peak power detected in the lobes is approximately  $10^3$ . After taking into account the factors involved when finding far-field patterns from the appropriate normalised mode fields, it was concluded that the extinction ratio of the mode convertor was on average better than 30 dB over the wavelength range of 750 - 1750 nm (this wavelength range is the overlap between the spectra of the supercontinuum source and the photodiode response).

Compared to LPG mode convertors [Ramachandran 02], the ferrule mode convertor approach is indeed a realistic and promising solution to high-extinction broadband mode convertors. It offers at least 30 dB over 1100 nm wavelength range compared to the 63 nm range at 20 dB of Ramachandran et al. It must be recognised that the extinction ratio is an average over many wavelengths, and there may be isolated wavelengths where it is worse. On the other hand, our results were limited by the dynamic range of the measurement; with a greater dynamic range may well have shown a far greater extinction ratio.

### 7.3. Multimode Fibre Device with Single-Mode Performance

In this section a ferrule transition between several SMFs and a MMF is described and it is used to demonstrate single-mode performance in a multimode fibre device [Leon-Saval 05c, Leon-Saval 05d, Birks 05b]. Many optical fibre devices exploit physical interactions that are mode-dependent. Although such devices can have high performance in SMF, the corresponding multimode fibre devices generally perform poorly. For example, simple SMF Bragg gratings are highly reflective over a narrow band of wavelengths, but a grating written directly in MMF reflects each mode at a different Bragg wavelength, giving a response that is spread over a range of wavelengths and depend on the mode spectrum excited in the MMF, as shown in Fig. 7.7 extracted from the paper of Su et al at OFC 05 [Mizunami 00, Su 05]. This has limited the range of high-performance devices implemented in MMF.

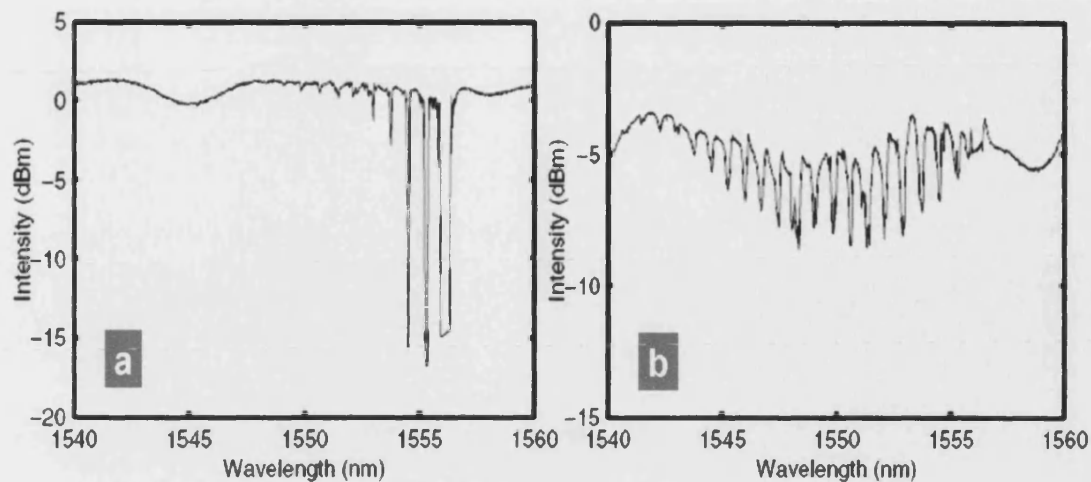


Fig. 7.7. [From Su 05] Transmission spectra of a uniform multimode fibre Bragg grating at different mode excitation conditions measured with 0.1nm resolution. (a) Transmission spectrum for low-order mode excitation and (b) transmission spectrum for highly multimode excitation.

We were approached by J. Bland-Hawthorn from the Anglo-Australian Observatory and M. Englund from Redfern Optical Components (ROC) in Australia. Their current work involves the filtering of narrow atmospheric emission bands from a telescope image. This would greatly enhance contrast in the infrared. However, each "pixel" of the image is incoherent and highly multimode, and can only be efficiently coupled to MMFs. This restriction to multimode fibres for light acquisition makes the filtering task non trivial. In the other hand, complex Bragg gratings can achieve the required filter response in SMF [Bland-Hawthorn 04]. Fig. 7.8 shows a typical response from their asymmetric Bragg gratings filtering the exact wavelengths of interest in an SMF. The ability to implement the SMF response in MMF could revolutionise ground-based observations of highly red-shifted astronomical sources.

We solved the above problem by using the ferrule technique to make a transition between several SMFs and an MMF. In Subsection 7.3.1 I describe the principle of operation of the transition and in Subsection 7.3.2 I explain how two such transitions can be used to make a MMF device with SMF performance that for this case will be Bragg grating performance.

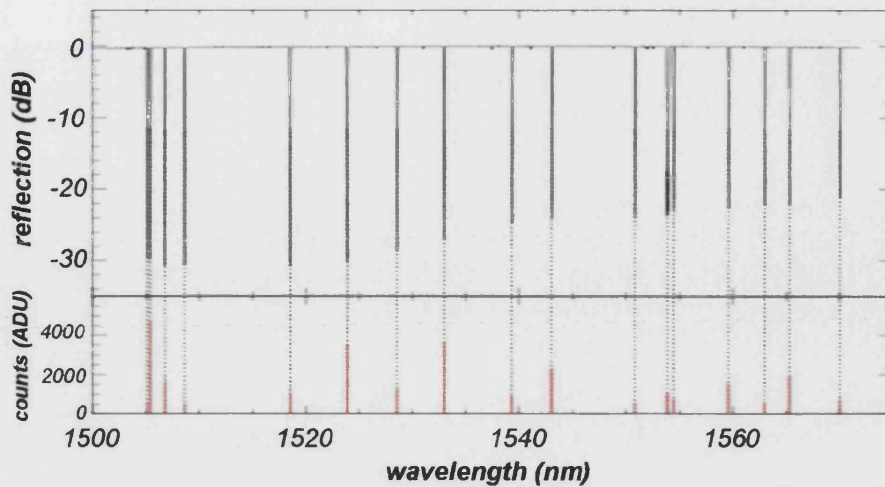


Fig. 7.8. [From Bland-Hawthorn 04] Comparison of reflection spectrum of an aperiodic fibre Bragg grating (top panel) with the targeted OH emission lines (bottom panel).

### 7.3.1. Transition Between an MMF and Several SMFs

The second law of thermodynamics prohibits the lossless coupling of light from an arbitrarily-excited MMF into one SMF, however low-loss coupling from an MMF core to another multimode system with at least as many degrees of freedom is possible. This idea was implemented using an array of isolated identical SMF cores as the degenerate multimode system. Its spatial modes are the supermodes of the array. Their number equals the number of cores and their propagation constants equal that of a core on its own [Ladouceur 90]. Light can be coupled between the array and an MMF via a gradual taper transition, Fig. 7.9. Conceptually it looks like half of a multiport fused coupler [Ladouceur 90, Mortimore 91, Arkwright 91]. If the transition is adiabatic then modes of the MMF core evolve into supermodes of the SMF array, and vice versa. If the number of MMF spatial modes matches the number of SMFs, the transition is a reversible low-loss splitter/combiner between the MMF and the SMFs. Otherwise there are MMF modes that do not evolve into SMF supermodes, or SMF supermodes that do not evolve into MMF modes, causing loss in the forward or reverse direction respectively for arbitrary excitation [Birks 05b]. This is important because inevitable unequal path lengths along the SMFs effectively scramble the supermodes.

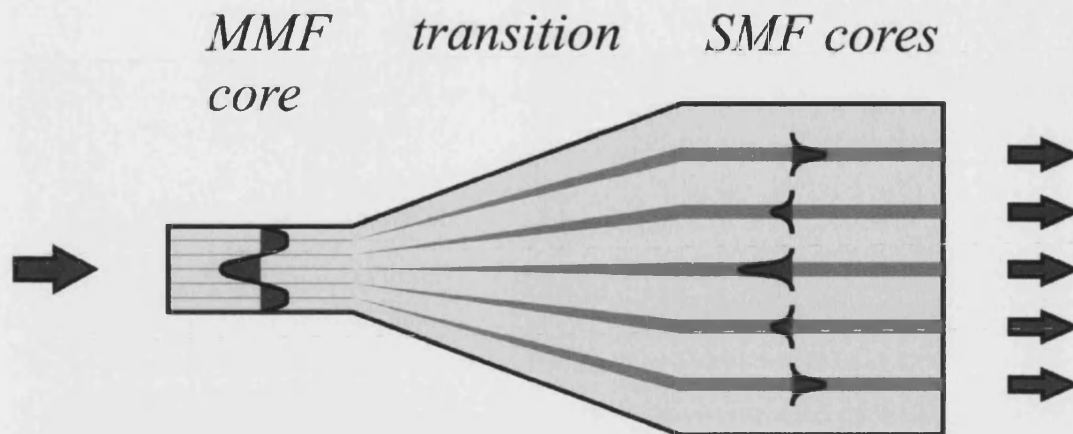


Fig. 7.9. A taper transition between a MMF and several SMFs. Each MMF mode evolves adiabatically into a supermode of weakly-coupled SMF cores and distributed between separate SMFs at the output.

Our experimental transitions interfaced an MMF core to 19 SMF cores. The SMF cores were separate SMFs and the MMF was a multimode "air-clad" PCF. A 2.8 mm diameter ferrule with an array of 380  $\mu\text{m}$  holes was made, Fig. 7.10(a). Conventional SMFs (diameter 125  $\mu\text{m}$ , cutoff wavelength 1250 nm) were inserted into 19 of the holes. Each SMF was coated for 3 cm inside the ferrule, to prevent accidental cleaving, but the rest of the fibre in the ferrule was uncoated.

The filled ferrule was drawn into a length of multimode PCF with a 145  $\mu\text{m}$  diameter and 35  $\mu\text{m}$  core, Fig. 7.10(c). By preserving the neck-down region in the furnace when drawing stopped, the MMF remained connected via a continuous transition to the SMF pigtailed protruding from the ferrule, Fig. 7.10(b) and (d). The MMF core incorporated material from the 19 SMFs, and was supported in an "air cladding" by a network of silica webs as shown in Fig. 7.10(c) [Espindola 99]. (The unusual snowflake shape of the core was due to distortion of adjacent holes, and could have been avoided using a ferrule with more holes).

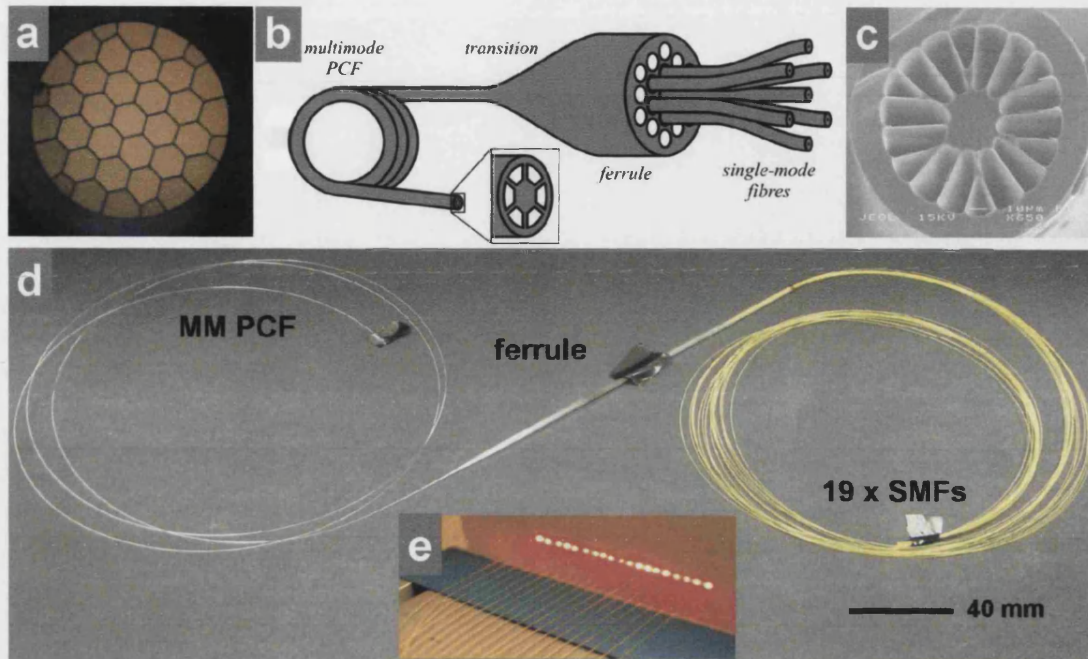


Fig. 7.10. (a) Optical micrograph of the ferrule. The holes were  $380\ \mu\text{m}$  across flats, and the solid outer jacket was  $260\ \mu\text{m}$  thick. (b) A MMF-SMF transition made by drawing ferrule cane filled with SMFs. (c) SEM image of the multimode PCF drawn from the filled ferrule after the central 19 holes were each filled with a piece of SMF. (d) Actual photo of the ferrule transition, (e) output of the 19 SMFs when launching He-Ne light into the multimode PCF.

The excess loss at  $1550\ \text{nm}$  wavelength from each of seven representative SMFs to the MMF core was measured by the cut back technique, and ranged between  $0.45$  and  $0.68\ \text{dB}$ . The loss in the reverse direction was not measured as it would depend on the mode spectrum launched. However the operation of the transition was visualized by launching light from a He-Ne laser into the MMF core and the output at the 19 SMFs was imaged [Fig. 7.10(e)]. It was observed that the light was indeed split more or less equally between the 19 SMFs.

### 7.3.2. SMF Bragg Grating Response in a Multimode Fibre Device

To make an MMF device supporting  $N$  modes that exhibits the same performance as an SMF device, the SMF ports of two of the transitions are connected together via  $N$  identical copies of the SMF device (one in each SMF port). For example, such a device

with Bragg gratings [Fig. 7.11] will reflect the same narrow band of wavelengths as each grating and transmit the rest; it will have MMF ports but the response of an SMF grating.

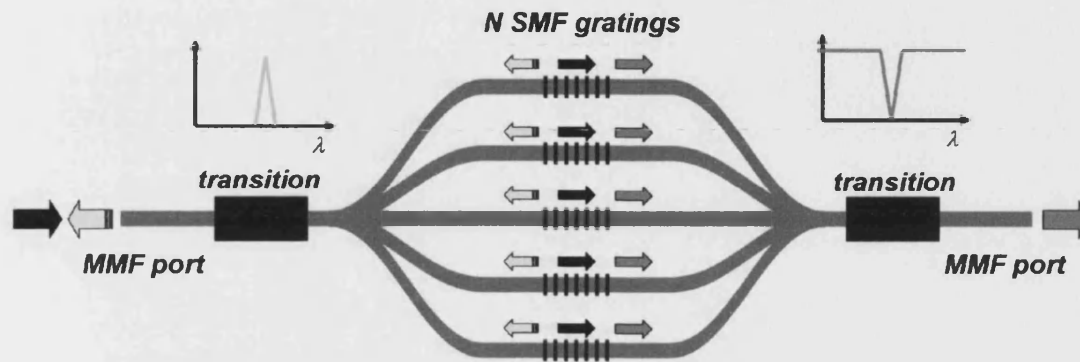


Fig. 7.11. Schematic diagram of a MMF grating device made by inserting  $N$  SMF gratings between the  $N$  SMF ports of two ferrule MMF-SMFs transitions.

19 nominally identical SMF Bragg gratings provided by ROC were fusion-spliced between two identical 1x19 transitions as depicted in Fig. 7.11. Light from an EDFA continuum source was launched via a conventional MMF into one MMF port. The output from the other MMF port was fed via another conventional MMF into an optical spectrum analyzer. The measured spectrum is plotted in Fig. 7.12(a), along with the average of the 19 SMF gratings. There were no other features outside the 2 nm range shown. The 0.07 nm ripples are weak Fabry-Perot fringes from the coupling optics and not a feature of the device. The zero on the vertical axis was adjusted for comparison with the SMF gratings, and does not represent zero loss.

The shape of the spectrum closely matched that of the SMF gratings, with a similar notch width and depth. In contrast, the response of a grating in an MMF with a numerical aperture of 0.2 would be spread over 15 nm [Su 05]. Heating 9 of the 19 gratings by 60 °C shifted the Bragg wavelength of those gratings and gave a spectrum with two 3-dB (50%) notches separated by 0.4 nm, also in Fig. 7.12(b). Their similar depths indicate the expected distribution of light between the two sets of SMFs.



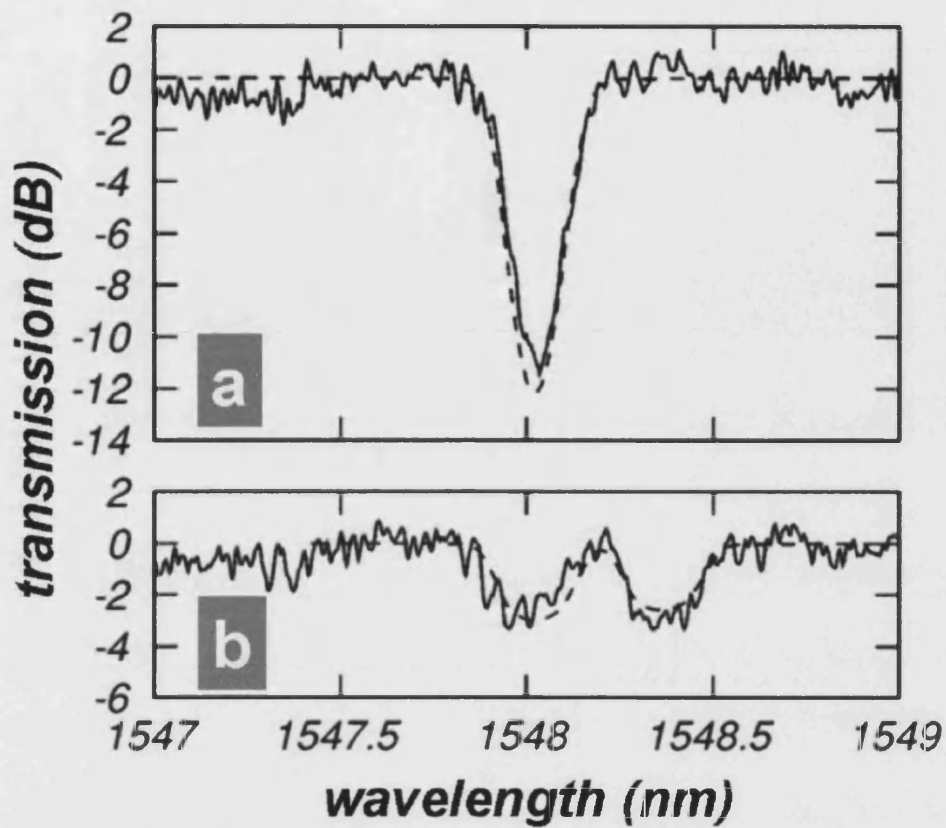


Fig. 7.12. (a) Transmission spectrum of the MMF grating device measured when all 19 gratings were at room temperature (solid line), together with the average (broken line) of the 19 SMF gratings as calculated from their data sheets. (b) as (a) but measured when 9 of the gratings were heated by 60 °C (solid line), together with the calculated average (broken line) with 9 of the gratings shifted in wavelength by the measured amount.

The measured transmission away from the grating notch was only 3.4%, but this high loss can be accounted for by the mode-number mismatch between the MMF and the SMF array. There was no attempt to match mode numbers in this proof-of-principle experiment. The number of MMF modes was estimated from SEM images like Fig. 7.10(c). The core is approximately a disc with a diameter of 34.5  $\mu\text{m}$ , and the supporting webs were 0.5  $\mu\text{m}$  thick. Hence the effective NA was 0.75 [Wadsworth 04b], and the fibre supported around 710 spatial modes [Snyder 83]. If these modes were equally excited at the input, the transmission of an otherwise ideal device would be 19/710, or 2.7%. There are large uncertainties in comparing these two transmission

values: the measured value included unknown coupling losses to the conventional MMFs at input and output; the grating and device SMFs were not identical, giving splice losses of about 0.8 dB; and the MMF modes would not have been equally excited. Nevertheless, the similarity between the measured transmission and that estimated by mode counting suggests that the device would be low-loss if the mode numbers were matched. Ferrule transitions between PCFs and SMFs exhibit losses of 0.6-0.8 dB (as presented in the previous chapter), which is similar to the losses of the devices from SMF to MMF, and analogous 1x19 fused couplers with losses of 0.3 dB have been reported [Arkwright 91]. Mode numbers can be matched by including enough SMFs to match a given number of MMF modes, or adjusting the MMF core diameter or NA to match a given number of SMFs: 50 SMFs would have matched the MMF if its NA was 0.2.

#### 7.4. Conclusion

Three completely different multi-fibre applications have been demonstrated using the versatile ferrule interfacing technique. A ferrule transition to a dual core PCF was demonstrated. This method was capable of coupling light without input cross talk (at least -34 dB) into individual closely spaced cores. A mode convertor from  $LP_{01}$  to  $LP_{11}$  with at least 30 dB extinction over a 1100 nm wavelength range has been demonstrated by interfacing between a single-core PCF and a couple of dissimilar fibres. MMF systems with single-mode performance have been demonstrated: 19 nominally identical Bragg gratings were fusion-spliced between two ferrule transitions from 1 MMF x 19 SMFs, and the Bragg grating response obtained was almost identical to the response of one of the individual gratings. The versatility of the ferrule interfacing technique has thus been demonstrated for very different applications.

---

# Chapter 8

## All Solid-Silica Photonic Bandgap Fibres

A photonic bandgap is a property of some two- or three-dimensionally periodic dielectric structures, whereby light of some frequencies at certain propagation constants are forbidden to propagate [Joannopoulos 95]. A photonic bandgap (PBG) fibre guides light because the core is surrounded by a cladding with a 2-D photonic bandgap [Birks 95b]. PBG fibres incorporating air [Cregan 99, Smith 03], fluids [Bise 02, White 02] and contrasting soft glasses [Luan 04] have been reported. In this chapter I demonstrate all solid-silica PBG fibres with a step index contrast of one percent by a new technique inspired by ferrule technology and using commercially-available single-mode and multimode fibres.

It is a common perception that very large refractive index contrasts are needed for bandgaps to occur. For example, a relative index step of over 160% is needed for light propagating perpendicular to an array of rods [Villeneuve 92]. However, a fixed but non-zero wavevector component parallel to such 2-D structure permits bandgaps for much smaller contrasts [Birks 95b]. So far, previously reported 2-D bandgap fibres still have substantial index steps of 16% or more [Luan 04], although theoretical studies have shown that 2-D bandgaps can appear for arbitrarily small index steps [Riishede 04, Birks 04]. It is therefore significant to experimentally demonstrate 2-D photonic bandgaps in solid optical fibres with index steps as low as only 1%.

### 8.1. Fabrication

In this section I will describe the fabrication of all solid-silica PBG fibres. These fibres have a silica background with slightly higher index rod inclusions of germanium doped silica. A central missing high index rod is the defect that creates the core, forming a PBG fibre with a silica core [Argyros 05a]. A ferrule preform with an outer diameter of 2 mm was used. Made from pure fused silica, it incorporated an array of air holes big enough (approx. 180  $\mu\text{m}$ ) to fit a conventional optical fibre inside, Fig. 8.1(a). Commercial step-index multimode fibres were inserted into each hole except the central one. Commercial single-mode fibre was inserted into the central hole, Fig. 8.1(b). The filled preform was then drawn to fibre in the conventional way to reduce the multimode cores from 50  $\mu\text{m}$  to 2  $\mu\text{m}$  in diameter. The air-gaps between the fibres

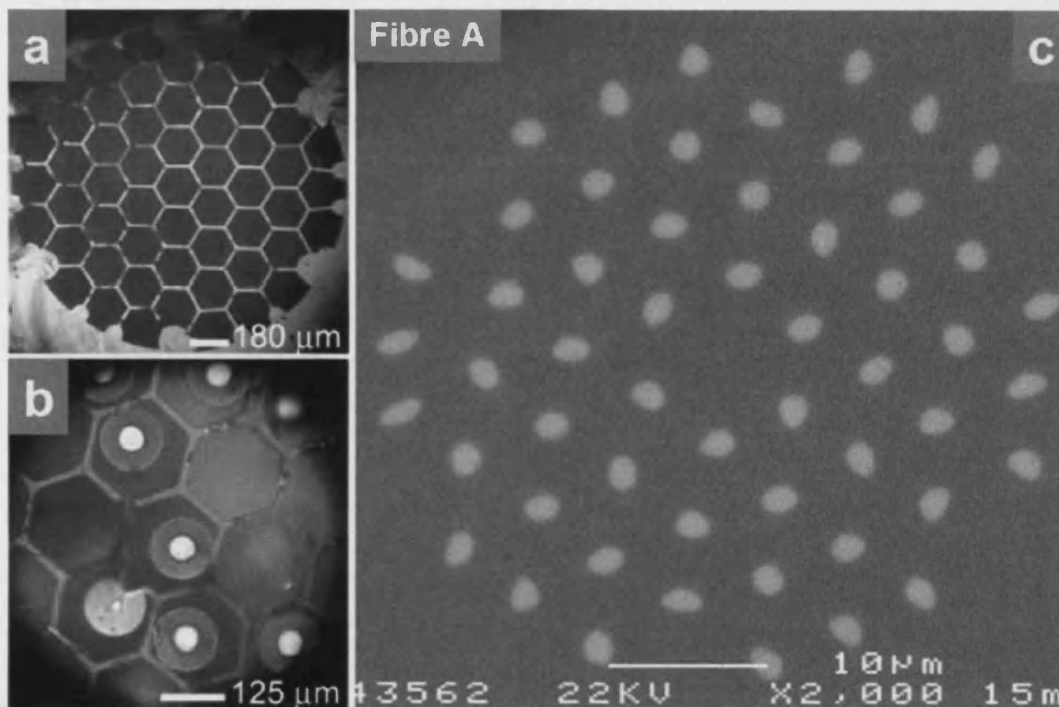


Fig. 8.1. (a) Optical micrograph of the end-face of the empty ferrule preform. (b) Optical micrograph of part of the partly-filled preform, showing some multimode fibres whose large cores will form rods in the bandgap fibre's cladding, and the one single-mode fibre (lower left) that will form the effectively-undoped core of the bandgap fibre. (c) Scanning electron micrograph of the end-face of fibre A drawn from a filled preform. The residual single-mode core is barely visible within the low-index bandgap-guiding core in the centre. The high-index rods appear light in the backscattered-electron image because Ge is a stronger scatterer of electrons than Si (a carbon coating was used under the SEM, as it is more transparent than gold).

and the ferrule perform were evacuated while the fibre was drawn, giving an all-solid structure Fig. 8.1(c). The result is a bandgap fibre with isolated rods of raised-index Ge-doped silica embedded in a background of lower-index pure silica. The pure silica region around the central lattice site lacks such a rod (since the single-mode fibre had a much smaller core than the multimode fibre to begin with) and is the defect that acts as the new fibre's low-index bandgap-guiding core.

Four different all solid-silica PBG fibres were made [Fig. 8.1 (c) and Fig. 8.2]. These fibres were made by using different ferrules and different SMFs and MMFs. The fibres were labelled Fibre A, B, C and D and some of their parameters are shown in Table 8.1. The fibres were drawn to various diameters, with the high-index rods becoming 2-3  $\mu\text{m}$  in diameter.

Table 8.1: Index table of all the fabricated solid-silica PBG fibres.

	$\Lambda$ ( $\mu\text{m}$ )	$d/\Lambda$	number of rings of rods	SMFs forming the core	rod NA	number of rings of holes in the ferrule	MMF used to form the rods
<b>Fibre A</b>	6	0.34	3	1 (SMF-28)	0.21	4	Corning Corguide
<b>Fibre B</b>	7.5	0.34	3	1 (SMF-28)	0.21	4	Corning Corguide
<b>Fibre C</b>	10	0.34	6	1 (SMF/3.5 $\mu\text{m}$ )	0.21	7	Corning Corguide
<b>Fibre D</b>	6	0.36	5	7 (SMF/3.5 $\mu\text{m}$ )	0.275	9	Thorlabs GIF625

Two different commercially available MMFs were used for the cladding of the fibres. Fibres A, B and C incorporated Corning Corguide, 50  $\mu\text{m}$  core diameter, 125  $\mu\text{m}$  outer diameter, NA = 0.21. This fibre had a double-cladding structure, which when drawn down becomes equivalent to a step index core with an NA = 0.18. In the other hand, for the cladding of fibre D, Thorlabs GIF625 was used: 62.5  $\mu\text{m}$  core diameter, 125  $\mu\text{m}$  outer diameter, graded index, NA = 0.275.

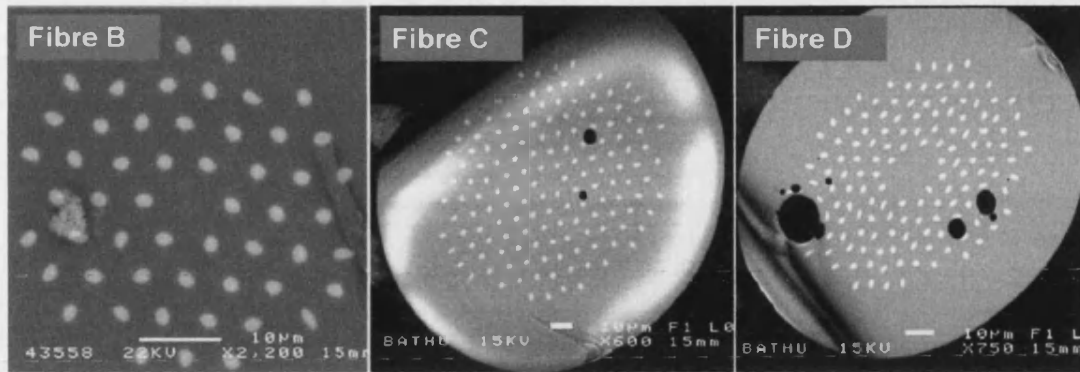


Fig. 8.2. SEM micrographs of samples of fibres (left to right) B, C and D. The black regions in C and D are (random) air bubbles that, apart from possibly contributing to the loss, did not appear to affect the guidance properties of the fibres. They were due to air trapped during the evacuation of the air-gaps between the PCF preform and the fibres.

Different SMFs were also used for the core of the fibres. Core of fibres A and B are formed by Corning SMF-28. A different SMF with a  $3.5\ \mu\text{m}$  core diameter,  $125\ \mu\text{m}$  outer diameter and  $\text{NA} = 0.11$  was used in the core of fibres C and D. To evaluate the importance of the residual single-mode core in the bandgap fibres I considered the guidance  $V$  parameter [Snyder 83, Black 87] for the biggest of the residual single-mode cores, which is in Fibre B and is about  $435\ \text{nm}$  in diameter. If this was embedded in an infinite pure-silica cladding, its  $V$  parameter would be around 0.34 at  $560\ \text{nm}$  wavelength. In other words, the residual single-mode cores on their own were not effectively waveguides at all [Black 87] and could be ignored: the bandgap fibre's cores were indeed effectively pure silica and could not guide light by total internal reflection.

Our bandgap fibres resemble previous ones [Bise 02, Luan 04] but with a much smaller index contrast. The relative index step in Fibre A calculated from the numerical aperture quoted in the multimode fibre's specifications was 1.05%, 16 times smaller than the next smallest reported [Luan 04] and well within the scalar "weak guidance" approximation [Snyder 83]. This means it behaves as a bandgap fibre with an arbitrarily small index step.

## 8.2. Optical Characterisation

White supercontinuum light (approx. 480 to 1700 nm) generated in a photonic crystal fibre using a Nd:YAG microchip laser [Wadsworth 04a] was used to illuminate the input end-faces of the fibres and spectrally filtered images (using 10 nm pass band filters) of the output end-faces were recorded. The nodes can act as conventional index-guiding waveguides but I am interested in guidance in the low-index core, which can confine light only by a photonic bandgap and not total internal reflection.

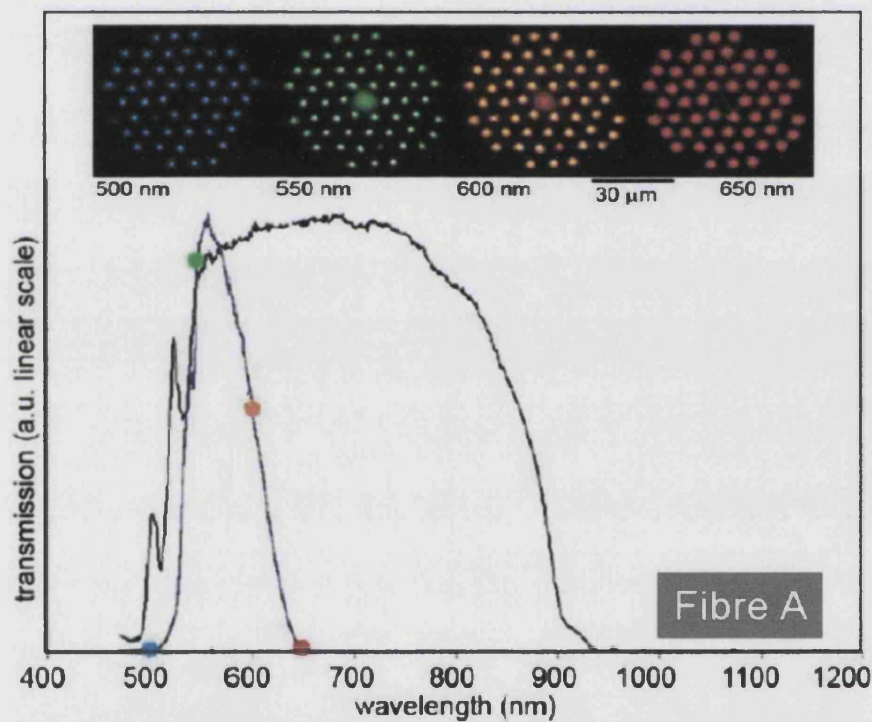


Fig. 8.3. Transmission spectra of fibre A ( $\Lambda=6 \mu\text{m}$ ) (black curve) for 0.2 m and (blue curve) for 10 m. The wavelengths of the images in the inset are marked as coloured circles on the corresponding curve. (inset) Output near-field images from 10 m of fibre A at indicated wavelengths for wide illumination (hence the nodes are lit up). A bandgap-guided mode is present in the central core for green and orange light.

Fig. 8.3 is the measured transmission spectrum of fibre A's core for 10 m and 0.2 m lengths. The spectra were obtained by placing a pinhole in the output image plane to

select the light from core alone, which was then coupled to an optical spectrum analyser. The difference between the transmission spectra of the 0.2 and 10 m pieces of fibre is due to losses and some fluctuations during the drawing of the fibre. These variations along the fibre produce shifts in the bandgap; so the net transmission spectrum along the total length is narrower.

Medium-term fluctuations in the supercontinuum source prevented accurate direct cutback measurements of attenuation at the minimum-loss wavelength of 560 nm. Instead the attenuation of fibre A was measured at 633 nm with a helium-neon laser and extrapolated to 560 nm using the transmission curve of Fig. 8.3, making conservative assumptions to deduce a minimum attenuation of  $\approx 1.3$  dB/m, comparable to that of commercially available air-guiding bandgap fibres at that wavelength. Other important loss mechanism depend on the index contrast and the presence of dopants in the core [Lines 99], but since confinement loss can be made arbitrarily small by including more rods in the cladding, it is intriguing to consider that the attenuation of such fibres could potentially be very low indeed.

Both fibres A and B ( $\Lambda=6$  and  $7.5$   $\mu\text{m}$  respectively) appeared to be single-moded in the core. These fibres were guiding in the first (lowest-frequency) bandgap of the cladding at the wavelengths shown in Figs. 8.3. For fibre B, and also fibres C and D, guidance in the second bandgap was also observed at short wavelengths. In fact the wavelength positions of the bandgap edges can be predicted quite accurately without recourse to sophisticated modelling, since according to the ARROW picture they lie where the modes of the index-guiding nodes are cut-off [Laegsgaard 04]. Resonance in the ARROW picture corresponds to a match in effective index between the bandgap-guiding core and one or more supermodes of the cladding, causing leakage of light from the core and hence loss. Since the bandgap-guiding core is made from the same material that surrounds the rods, resonance occurs around the cutoffs of the higher-order modes of an isolated rod. Low-loss guidance is therefore expected in the bandgaps between the rod mode cutoffs, where no supermode matches the bandgap-guiding core in effective index.



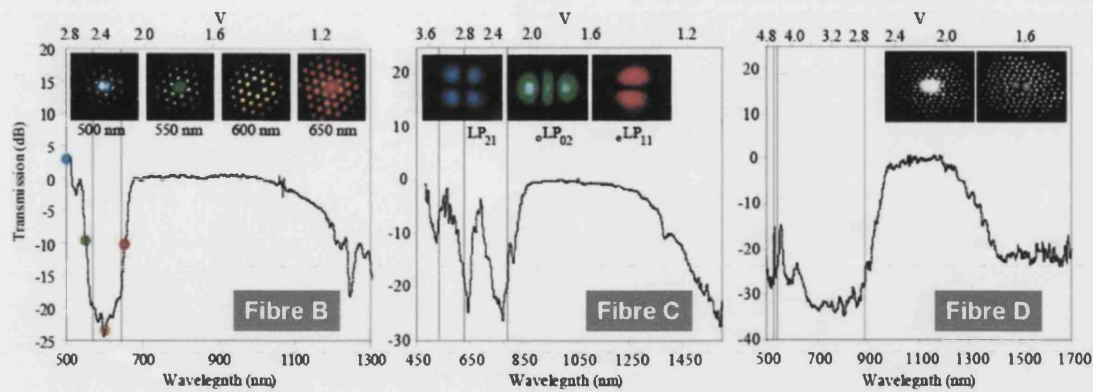


Fig. 8.4. (Fibre B) Transmission in the first two bandgaps of fibre B ( $\Lambda = 7.5 \mu\text{m}$ , length 0.15 m) for illumination of the core alone. Insets are filtered images of the fibre endface for wide illumination. (Fibre C) Transmission in the first 4 bandgaps of a sample of fibre C ( $\Lambda = 10 \mu\text{m}$ , length 0.4 m). Insets are modes excited in the rods by focusing light into the core at the high-loss wavelengths for a sample of fibre C. (Fibre D) Transmission of fibre D ( $\Lambda = 6 \mu\text{m}$ , length 0.4 m). Insets show the two modes supported by the core ( $\text{LP}_{01}$  and  $\text{oLP}_{11}$ ) at  $\lambda = 1064 \text{ nm}$ . The high-order mode cutoffs are indicated, corresponding to high-loss wavelengths. Spectra have been normalised to give 0 dB transmission in the first bandgap.

The transmission spectrum for fibre B is plotted in Fig. 8.4(Fibre B) and shows the first bandgap, and part of the second at shorter wavelengths. (The measured range was limited by the source spectrum). Near-field images of the output endface for wide illumination (of the core and the rods) at the input are inset, showing the bandgap-guiding core to be single-mode in the first bandgap, multimode in the second, and not guiding at all in between. High loss corresponded to  $V \approx 2.4$ , i.e. the cutoff of the odd and even  $\text{LP}_{11}$  modes, as expected.

The transmission spectrum for a sample of fibre C is plotted in Fig. 8.4(Fibre C) and shows the first four bandgaps. The bandgap guided core mode has a presence in the rods, the field taking on the shape of the rod mode to which it is closest in effective index - i.e. the one which is closest to being resonant. This is essentially the result of inefficient directional coupling between mismatched waveguides. If input light is tightly focused into the core to excite only the bandgap-guided core mode, for wavelengths in a bandgap only the rods closest to the core are illuminated. In contrast, for wavelengths outside the bandgaps no light remains in the core and all the rods are illuminated. This is the mechanism by which light leaks out of the core when the rods are resonant:

focusing into the core excites a supermode of the rods. The rod modes making up the supermodes were observed directly by tight focusing into the core of fibre C and are shown in the insets of Fig. 8.4(Fibre C). These rod modes determine which bandgap is which [Argyros 05b].

The transmission of fibre D with is shown in Fig. 8.4(Fibre D), as are near-field images at the output. The larger core enabled this fibre to support two modes in the first bandgap. The first bandgap but not the second is still present, illustrating the insensitivity of this bandgap to the poor quality of the fibre.

### 8.3. Conclusion

The simplicity of fabricating bandgap fibres using readily available conventional fibres to provide the raised-index material has been demonstrated. Although a photonic crystal fibre preform was used to hold the constituent fibres in place it performed no other function; there was no need to maintain air holes in the all-solid fibres. Fibre drawing equipment is reasonably common and, unlike previous bandgap fibres, this technique can form metre (and potentially kilometre) lengths of bandgap material without the usual stringent steps to control the process. The fibre design is clearly tolerant to imperfections, since the distortion of circular multimode cores into the randomly-oriented elliptical nodes seen in Fig. 8.1 and 8.2 did not stop the fibres guiding light. The fibre is therefore a convenient and effective source of photonic bandgap material in quantity, and I expect at least the dispersion and spectral attenuation properties to find applications.

---

# Chapter 9

## Conclusions

### 9.1. Summary

During my PhD studies I focused on the exploration of different applications and devices based on optical fibre transitions. I have demonstrated some new types of transitions, and shown that they are a powerful tool for the fabrication of many different devices.

**Evanescent field in tapered optical fibres:** Evanescent field interactions between tapered conventional fibres and porous sol-gel derived silica were studied.

- A new method for LPG fabrication was reported based on the combination of the three well-known techniques of tapering, sol-gel processing, and laser irradiation heating. LPGs with up to 15 dB spectral notches and background losses of 0.2 dB (away from the resonance peak) have been demonstrated.
- The formation of aerogel blocks around tapered fibres has been achieved for the first time giving a promising proof of concept. 20  $\mu\text{m}$  diameter tapers including transitions were embedded in aerogel with overall losses of 0.75 dB at 1550 nm. This proof of concept could be a building block for many exciting applications due to the peculiar physical and optical properties of this material.

**Tapering of PCFs and conventional optical fibres:** During my research I have worked in the improvement of tapering PCFs and conventional fibres.

- I have reported the lowest losses so far in the fabrication of submicron scale conventional tapered fibres. In just centimetres of these submicron waveguides, nanosecond pulses from a low-power frequency doubled 532-nm microchip laser generated a single-mode supercontinuum broad enough to fill the visible spectrum without spreading far beyond it.
- Supercontinuum generation in submicron-core PCFs, and indeed in any form of optical guidance along PCFs with submicron pitch, have been reported for the first time.
- A new post-processing technique for PCFs has been demonstrated. In this technique the holes of PCF cladding were inflated by pressurising the holes whilst heating/tapering the fibre. This method has enabled the interfacing of large-core single-mode PCFs to high air-filling fraction PCFs with small cores, with losses as low as 0.3 to 0.4 dB. Differential hole pressurisation and heat treatment were used to radically change the core shape along a piece of non-birefringent photonic crystal fibre, forming a low-loss (<0.4 dB) transition to a highly-birefringent core with a sub-millimetre beatlength.

**Universal technique for interfacing PCFs and standard optical fibres:** I have developed the “ferrule” technique for the interfacing of PCFs and standard SMFs. This is an adaptation of the process by which a PCF is made from a stack of tubes and rods. The result was a PCF in which its core incorporates an entire drawn-down SMF. The PCF connected via an adiabatic transition to the remaining PCF preform, from which a length of SMF protruded. Light propagating in the SMF core spreads out from the core and becomes guided by the PCF structure along the transition. The complete transition was low-loss and it was formed without any splices.

- This method enabled the coupling of light between SMF and endlessly single-mode PCFs as well as highly nonlinear PCFs, with losses as low as 0.6 dB.
- Another challenging interfacing problem that this method readily solved is the multicore PCF. I believe this to be the first method for coupling light without input crosstalk into the individual cores of any type of multicore fibre. Less than -34dB input crosstalk was achieved in SMF to multicore PCF transitions.
- By combining the ferrule technique with the concept of “null” fused couplers, I have demonstrated a fibre mode convertor. This non-resonant device coupled light from  $LP_{01}$  to  $LP_{11}$  modes with an extinction ratio better than 30 dB at all wavelengths from 750-1750 nm.
- I have demonstrated transitions from 1 multimode fibre to 19 single-mode fibres using the ferrule technique. 19 nominally identical SMF Bragg gratings were fusion-spliced between two such transitions. The MMF device showed a spectral response identical to that expected from a SMF Bragg grating, demonstrating single-mode Bragg grating performance in a multimode fibre device for the first time.

**All-Solid Silica Core Photonic Bandgap Fibres:** Bandgap fibres were demonstrated with index contrasts of 1 %, using Ge-doped silica rods in a pure silica background. This was the first report of such a low index contrast photonic bandgap fibres. Although not involving fibre transitions, these fibres were made using a new technique based in the ferrule idea.

## 9.2. Future Work Directions

The work carried out during this thesis can be extended in many directions. In this subsection I will present an outline of the different ways in which this work can be continued.

Silica aerogels (and other forms of porous silica glass) as a cladding material around tapered optical fibres can be investigated. The aerogel is materially compatible with silica fibres, but has a refractive index as low as that of air. Three ways have been identified to exploit it. Firstly, it can be used simply as a rigid substitute for air as a cladding material: "solid air". It will act as a fixed spacer between it and other structures, and could be useful for packaging couplers. Secondly, the refractive index of the material can be adjusted by changing its porosity. This causes a useful modification in the chromatic dispersion of the waveguide, giving a valuable extra degree of freedom in the design of fibre-compatible nonlinear devices for frequency generation and conversion. Finally, there have been reports that silica aerogel is a highly nonlinear optical material in its own right. In any case, doping the aerogel provides a new way to optically interact with a range of nonlinear and other functional optical materials.

The disadvantage of tapering optical fibres is that only short lengths (around 15 cm) are produced with the existing taper rig. However, my recent work has been focused in the fabrication of a new taper rig which would be able to produce between 1-2 meters of this type of tapered waveguides. Such taper rig could be used for the fabrication of metre scale lengths of submicron-core PCFs with an easy input/output by taper transitions. This will provide longer interaction lengths for SC generation, soliton effects, pulse compression, and other interesting nonlinear properties. As explained in Chapter 4, the superiority of tapering over the drawing fibre technique will also allow fabricating lengths of hollow core PCF with much smaller pitch. This will make possible such fibres that guide UV light.

The inflation technique will allow the fabrication of all-fibre systems in which large-core single-mode PCFs (easily spliceable to SMFs) are connected to small-core high air-filling fraction PCFs with low loss. Low-loss core shape transitions could provide interesting possibilities. For example, a transition from a standard single-mode PCF to a

rectangular shape core will give efficient coupling from a diode laser without the need for bulk optics.

Only silica glass has been considered during this thesis. But I firmly believe that an interesting direction to follow will be to investigate the post processing of soft glasses optical fibres. Such soft glass fibres exhibit much higher nonlinearities, and for example submicron fibre waveguides made from those fibres could produce spectacular nonlinear effects.

The ferrule interfacing technique has been proven to be a very versatile method. The research in the different devices achieved by this technique can be extended in many ways. For example, the SMFs to multicore interfacing device could be used in multicore sensing applications where the elimination of the input/output crosstalk is a key element for the practicability of the system. The mode convertor technology could develop a  $LP_{01}$  to  $LP_{02}$  mode convertor. This mode is proposed for dispersion compensation in telecommunications technology. Also a submicron-core mode convertor would allow exploring dispersion properties of higher order modes for nonlinear interactions. The possibility of having MMF systems with SMF performance could find a large number of different applications. The immediate direction to follow in this area would be the further development of the Bragg grating response for the MMF device. The aim would be to produce a low-loss system in which the number of SMFs would match the number of modes in the MMF.

The work carried out in all solid-silica photonic bandgap fibres can be extended towards; for example, the study of multicore bandgap fibres. These fibres exhibit interesting coupling properties between the cores [Bird 05], such as very long beatlength between close-spaced cores. Another interesting direction to follow will be the research in bending losses in such fibres; for example, how the light in the core couples to the high index inclusions in the bending direction. Ultimately, these fibres could be made with attenuations as low as those of the best conventional SMFs.

# Figures and Tables

## Chapter 1

### Conventional Step-Index Silica Optical Fibres

Fig. 1.1. Schematic diagram of a conventional step-index fibre. (p. 2)

Fig. 1.2. Schematic drawn of the most significant parts of a fibre drawing tower. (p. 3)

Fig. 1.3. Illustration of the behaviour of a light ray incident on the boundary between two media with refractive indices  $n_1$  and  $n_2$  where  $n_2 < n_1$ . In general, a transmitted and a reflected beam are produced. It is also shown that the propagation constant  $\beta$  is the projection of the wave vector  $kn_1$  onto the horizontal axis. (p. 4)

Fig. 1.4. (a) Illustration of the behaviour of a light ray travelling within a finite dielectric medium of width  $a$  and with a higher refractive index  $n_1$ , surrounded by an infinite dielectric medium with a lower refractive index  $n_2$ . (b) Schematic representation of the transverse phase change over a round trip. (p. 5)

Fig. 1.5. Illustration of the mode field intensity distribution of the fundamental mode of a optical fibre. The Gaussian-like tails of the intensity profile spread into the cladding forming the evanescent field. (p. 7)

Fig. 1.6. [From Li 85] Measured variation of the dispersion parameter  $D$  with wavelength for a single-mode fibre. (p. 9)

Fig. 1.7. Illustration of mode mismatch as cause for loss when interfacing between two optical fibres with very different MFDs. (p. 11)

## Chapter 2

### Photonic Crystal Fibres and Tapered Fibres

Fig. 2.1. Schematic drawing of a coated index-guiding PCF, where the white regions are air and the light grey regions are silica. The effective refractive index profile and the parameters used to define a PCF are also shown. (p. 12)



**Fig. 2.2.** Schematic drawing of the PCF fabrication process by the stacking and draw technique.

(p. 14)

**Fig. 2.3.** SEM photographs of (a) and (b) single-mode PCFs; (c) and (d) cobweb PCFs with a high air-filling fraction; (e) high NA PCF; and (f) highly birefringent PCF. Fibres (a) to (d) were manufactured during the work of this PhD, fibres (e) and (f) were courtesy of Blazephotonics Ltd.

(p. 16)

**Fig. 2.4.** Schematic sketch of allowed (dark grey) and forbidden ranges of modal index  $n_m = \beta/k$

in silica, air and a suitable PCF cladding ( $k$  is the free-space wave-vector). (p. 17)

**Fig. 2.5.** SEM photographs of (a) air core HC-PCF (low-index inclusions) and (b) all solid silica core PBG fibre (high-index inclusions). Fibre (a) was courtesy of Blazephotonics. and fibre (b) was manufactured during this PhD and will be explained in detail in Chapter 8.

(p. 18)

**Fig. 2.6.** Schematic illustration of the tapering process. (p. 19)

**Fig. 2.7.** (a) Photograph of the taper rig at the University of Bath, (inset) metallic burner used to produce the tapering flame. (b) Schematic drawing of the flame brush technique used for tapering.

(p. 20)

**Fig. 2.8.** Illustration of the behaviour of the light in a taper. The fundamental mode in the core spreads out as it narrows until it is guided by the outer boundary in the taper waist.

(p. 21)

**Fig. 2.9.** Degrees of freedom when tapering PCFs; (a) Stretching: reduce cross-section, constant  $d/\Lambda$ ; (b) Hole collapse: change  $d/\Lambda$ , approximately constant cross-section.

(p. 22)

**Fig. 2.10.** Evolution of the calculated dispersion spectra of taper waists (a strand of silica surrounded by air) as the diameter (labelled) decreases, together with the dispersion of the bulk silica material.

(p. 25)

### Chapter 3

#### Sol-Gel, Aerogel and Tapered Conventional Fibres

**Table 3.1:** Parameters of the three different fabricated LPGs. (p. 34)

**Fig. 3.1.** Modified dip coating setup. (p. 30)

**Fig. 3.2.** [From Taylor 92] Change in refractive index of laser-densified (open circles) and furnace-fired (closed circles) TEOS coatings. (p. 31)

**Fig. 3.3.** Schematic CO<sub>2</sub> laser rig set-up. (p. 32)

**Fig. 3.4.** Transmission spectra of (light grey solid line) LPG A, (light grey dashed line) LPG B, and (dark grey solid line) LPG C. (p. 34)

**Fig. 3.5.** Transmission spectra of sol-gel LPG with number of periods erased in successive scans of the CO<sub>2</sub> laser beam until the grating pattern is totally erased. (p. 35)

**Fig. 3.6.** Transmission spectra of three different LPGs written and erased on top of each other in the same taper waist. Final erasure of the third LPG leaves a background loss of less than 0.4 dB. (p. 36)

**Fig. 3.7.** Removable furnace integrated into the taper rig. (p. 37)

**Fig. 3.8.** Variation of coupling wavelength with temperature: (solid triangles) with increasing temperature; (closed circles) with decreasing temperature. (p. 38)

**Fig. 3.9.** Supercritical drying of methanol. (p. 41)

**Fig. 3.10.** Photograph of the sol-gel mould with dimensions. (p. 43)

**Fig. 3.11.** Autoclave and sketch of the one litre volume inside. (p. 44)

**Fig. 3.12.** 20 µm tapered fibre embedded in bulk aerogel with He-Ne laser propagating through the fibre: (left) lights on, (right) lights off. The background is 5 mm squared paper. (p. 45)

**Fig. 3.13.** Photograph showing a broken sample hanging from the two 20 µm tapered fibre embedded in it. (p. 45)

## Chapter 4

### Submicron Fibre Waveguides

**Table 4.1:** Typical loss per unit length, for taper waists with the specified diameter and length, compared with the results of Tong et al. (p. 51)

**Fig. 4.1.** Evolution of the calculated dispersion spectrum of taper waists (a strand of silica surrounded by air) as the diameter (labelled) decreases. The straight lines mark zero dispersion and 532 nm wavelength. (p. 48)

**Fig. 4.2.** SEM image of a taper waist with a nominal diameter of 620 nm, as predicted by Eq. 4.1. (p. 50)

**Fig. 4.3.** SC spectra generated by taper waists for diameter, length and average laser power of (a) 920 nm, 90 mm and around 3 mW, and (b) 510 nm, 20 mm and around 1.5 mW respectively. The grey curve in (a) is for a sample made from Nufern 630-HP fibre instead of Corning SMF-28. (p. 52)

**Fig. 4.4.** Output far-field patterns from a 920 nm diameter tapered fibre made from SMF-28 for (a) low and (b) maximum power. The pattern in (b) was passed through 10-nm bandpass filters at (c) 450, (d) 589 and (e) 633 nm. (f) The variation of the SC spectra with average pump power. (p. 53)

**Fig. 4.5.** Conventional fibre drawing: the drawing force  $F$  is uniform along the neck-down region in the furnace, so wider parts are being drawn at low stress even if the fibre leaves the furnace at breaking stress. (p. 55)

**Fig. 4.6.** SEM images of PCF cores of diameter 3.1 (untapered), 0.7 and 0.5  $\mu\text{m}$  (left to right; different scales). (p. 56)

**Fig. 4.7.** Supercontinuum spectra generated by PCF cores of diameter (a) 700 nm and (b) 500 nm. Both were 90 mm long and carried an average power of around 1.7 mW. (p. 57)

## Chapter 5

### Hole Inflation in PCFs

**Table 5.1:** Dimensions of the inflated PCFs shown in Fig. 5.4. The scaled fibre values are obtained by multiplying the initial fibre values by the same factor of 0.92, to represent the effect of the slight tapering if the holes did not deform. (p. 66)

**Table 5.2:** Parameters for the inflated and tapered fibres shown in Fig. 5.6. (p. 69)

**Fig. 5.1.** Calculated MFD at a wavelength of 1  $\mu\text{m}$  for PCFs with a 5  $\mu\text{m}$  diameter solid core and varying  $d/\Lambda$ . (p. 61)

**Fig. 5.2.** Photographs of (a) the gas cell used to pressurise the holes of the fibres and allow optical input and output from the core, (inset) frontal view of the optical window; (b) silica burner with 108 holes of 125 $\mu\text{m}$  diameter and (c) typical steel burner used in our taper rig. Photographs (b) and (c) are roughly at the same scale. (p. 63)

**Fig. 5.3.** Schematic drawing of fibre inflation and tapering process to produce small core highly nonlinear PCFs with large air holes, connected to both ends to ESM PCF pigtailed with small air holes. (p. 64)

**Fig. 5.4.** SEMs of (a) the original 5  $\mu\text{m}$  core ESM PCF (b)-(d) the same PCF inflated at pressures of 6, 8 and 10 bar respectively. (p. 65)

**Fig. 5.5.** SEMs of (a) the original 12  $\mu\text{m}$  core ESM PCF (b) the same PCF inflated at pressure of 10 bar. (p. 67)

**Fig. 5.6.** SEM images of the inflated and tapered fibres. (top) initial 5  $\mu\text{m}$  core ESM PCF, (middle) inflated PCF and (bottom) tapered inflated PCF. All pictures to the same scale. Left to Right; Final taper core diameters 1.1, 1.6, 1.9  $\mu\text{m}$  respectively. (p. 68)

**Fig. 5.7.** Supercontinuum spectra for inflated fibres. For the tapered core diameter of 1.6  $\mu\text{m}$  and coupled power of 123 and 92 mW, and the tapered core diameter of 1.9  $\mu\text{m}$  and coupled power of 130 and 103 mW. (p. 70)

**Fig. 5.8.** The PCF (a) before and (b) after inflation and tapering with one hole blocked next to the core. (p. 71)

**Fig. 5.9.** Near-field images at the output (a) with the input fibre present, and (b) with the input fibre removed and a defocused launch so that the cladding features were illuminated for comparison. (c) Measured polarisation beating. (p. 73)

## Chapter 6

### Interfacing SMFs to PCFs: The “Ferrule” Idea

**Fig. 6.1.** Longitudinal section, showing how the mode spreads out from the tapered SMF core to become guided by the surrounding PCF core. (p. 76)

**Fig. 6.2.** Schematic diagram of the ferrule fabrication process. (p. 77)

**Fig. 6.3.** Optical photographs of (a) starting structure OD=2.86 mm; (b) and (c) ferrule transition at a point with OD= 2.05 mm, without and with circles marking the gaps between the SMF and the preform (grey) and the unblocked holes (black) respectively; (d) at a point in the transition with OD=1.38 mm, showing the complete collapse of the gaps. (p. 79)

**Fig. 6.4.** (a) SEM of a 2.86 mm diameter ferrule. (b) Optical micrograph of the central void in such a ferrule containing a 125  $\mu\text{m}$  diameter SMF-28. (c) SEM of the endlessly single-mode solid-core PCF drawn from the ferrule. (d) Schematic drawn of a ferrule interfacing device. (p. 80)

**Fig. 6.6.** (a) Optical photograph of a high air-filling-fraction ferrule. Each hole is 380  $\mu\text{m}$  across flats. (b) Optical photograph of one of the holes containing a SMF. (c) SEM of a highly nonlinear PCF with a 2.8  $\mu\text{m}$  core drawn from the ferrule. (d) Supercontinuum spectra at the output of the PCF when femtosecond pulses were coupled into the SMF-28. The average output powers were 0.03, 5, and 21 mW (dashed, dotted, and solid curves, respectively) as estimated by integrating the curves. (p. 81)

**Fig. 6.7.** (a) SEM of the ferrule. Central hole is 145  $\mu\text{m}$  across flats. (b) SEM of a highly nonlinear PCF with a 2.6  $\mu\text{m}$  core drawn from the ferrule. (c) SC spectra at the output of the

PCF when 532 nm nanosecond pulses were coupled into the SMF-28. (c) insets: (bottom) measured far field image at the PCF output of the high-order modes SC, (top) SC spectra near field image dispersed by a grating and projected onto a piece of paper. (p. 82)

## Chapter 7

### Using Ferrules to Interface More than One SMF to One PCF

**Fig. 7.1.** (a) SEM of the voids (separated by 1.5 mm) in a two-core ferrule. (b) Photograph of the undrawn end of the ferrule containing two SMFs. (c) SEM of the drawn 110  $\mu\text{m}$  diameter two-core PCF. (p. 85)

**Fig. 7.2.** (a)-(c) Near field images at the output of the PCF for light coupled into both SMFs then each SMF alone in turn. (d) Graph showing detected power of the near field at the output of the PCF whilst scanning a photodiode across the horizontal axis of the PCF cores (coupling the light into each SMF alone in turn). (p. 86)

**Fig. 7.3.** Evolution of light through a “null” coupler when launched (a) into the larger fibre and (b) into the smaller fibre. (p. 87)

**Fig. 7.4.** (a) Schematic diagram of the construction of a ferrule transition between two dissimilar SMFs and a multimode PCF. (b) Schematic diagram showing the behaviour of the light propagating in a “null” coupler waist. (p. 88)

**Fig. 7.5.** SEMs of (a) the empty ferrule and (b) the final multimode PCF. (c) Measured far field patterns at the output PCF, for light of two wavelengths in the first (top) and the second (bottom) input SMFs. (p. 89)

**Fig. 7.6.** Power detected by a photodiode scanned along the line X-X' across the LP<sub>11</sub> mode far field pattern (upper inset); (lower inset) the spectrum of the supercontinuum source and the photodiode response. (p. 90)

**Fig. 7.7.** [From Su 05] Transmission spectra of a uniform multimode fibre Bragg grating at different mode excitation conditions measured with 0.1nm resolution. (a) Transmission spectrum for low-order mode excitation and (b) transmission spectrum for highly multimode excitation. (p. 92)

**Fig. 7.8.** [From Bland-Hawthorn 04] Comparison of reflection spectrum of an aperiodic fibre Bragg grating (top panel) with the targeted OH emission lines (bottom panel). (p. 93)

**Fig. 7.9.** A taper transition between a MMF and several SMFs. Each MMF mode evolves adiabatically into a supermode of weakly-coupled SMF cores and distributed between separate SMFs at the output. (p. 94)

**Fig. 7.10.** (a) Optical micrograph of the ferrule. The holes were 380  $\mu\text{m}$  across flats, and the solid outer jacket was 260  $\mu\text{m}$  thick. (b) A MMF-SMF transition made by drawing ferrule cane filled with SMFs. (c) SEM image of the multimode PCF drawn from the filled ferrule after the central 19 holes were each filled with a piece of SMF. (d) Actual photo of the ferrule transition, (e) output of the 19 SMFs when launching He-Ne light into the multimode PCF. (p. 95)

**Fig. 7.11.** Schematic diagram of a MMF grating device made by inserting  $N$  SMF gratings between the  $N$  SMF ports of two ferrule MMF-SMFs transitions. (p. 96)

**Fig. 7.12.** (a) Transmission spectrum of the MMF grating device measured when all 19 gratings were at room temperature (solid line), together with the average (broken line) of the 19 SMF gratings as calculated from their data sheets. (b) as (a) but measured when 9 of the gratings were heated by 60  $^{\circ}\text{C}$  (solid line), together with the calculated average (broken line) with 9 of the gratings shifted in wavelength by the measured amount. (p. 97)

## Chapter 8

### All Solid-Silica Photonic Bandgap Fibres

**Table 8.1:** Index table of all the fabricated solid-silica PBG fibres. (p. 101)

**Fig. 8.1.** (a) Optical micrograph of the end-face of the empty ferrule preform. (b) Optical micrograph of part of the partly-filled preform, showing some multimode fibres whose large cores will form rods in the bandgap fibre's cladding, and the one single-mode fibre (lower left) that will form the effectively-undoped core of the bandgap fibre. (c) Scanning electron micrograph of the end-face of fibre A drawn from a filled preform. The residual single-mode core is barely visible within the low-index bandgap-guiding core in the centre. The high-index rods appear light in the backscattered-electron image because Ge is a stronger scatterer of electrons than Si (a carbon coating was used under the SEM, as it is more transparent than gold). (p. 100)

**Fig. 8.2.** SEM micrographs of samples of fibres (left to right) B, C and D. The black regions in C and D are (random) air bubbles that, apart from possibly contributing to the loss, did not appear to affect the guidance properties of the fibres. They were due to air trapped during the evacuation of the air-gaps between the PCF preform and the fibres. (p. 102)

**Fig. 8.3.** Transmission spectra of fibre A ( $\Lambda=6\ \mu\text{m}$ ) (black curve) for 0.2 m and (blue curve) for 10 m. The wavelengths of the images in the inset are marked as coloured circles on the

corresponding curve. (inset) Output near-field images from 10 m of fibre A at indicated wavelengths for wide illumination (hence the nodes are lit up). A bandgap-guided mode is present in the central core for green and orange light. (p. 103)

**Fig. 8.4.** (Fibre B) Transmission in the first two bandgaps of fibre B ( $\Lambda = 7.5 \mu\text{m}$ , length 0.15 m) for illumination of the core alone. Insets are filtered images of the fibre endface for wide illumination. (Fibre C) Transmission in the first 4 bandgaps of a sample of fibre C ( $\Lambda = 10 \mu\text{m}$ , length 0.4 m). Insets are modes excited in the rods by focusing light into the core at the high-loss wavelengths for a sample of fibre C. (Fibre D) Transmission of fibre D ( $\Lambda = 6 \mu\text{m}$ , length 0.4 m). Insets show the two modes supported by the core ( $LP_{01}$  and  $oLP_{11}$ ) at  $\lambda = 1064 \text{ nm}$ . The high-order mode cutoffs are indicated, corresponding to high-loss wavelengths. Spectra have been normalised to give 0 dB transmission in the first bandgap. (p. 105)

# References

- [Agrawal 95] Govind P. Agrawal, "Fiber-Optic Communications Systems", Wiley (New York), 3<sup>rd</sup> ed, 1995.
- [Agrawal 01] Govind P. Agrawal, "Nonlinear Fiber Optics", Academic Press(San Diego), 3<sup>rd</sup> ed, 2001.
- [Argyros 05a] A.Argyros, T.A.Birks, S.G.Leon-Saval, C.M.B.Cordeiro, F.Luan, P.St.J.Russell, "Photonic bandgap with an index step of one percent", Opt. Express 13, pp 309, 2005.
- [Argyros 05b] A.Argyros, T.A.Birks, S.G.Leon-Saval, C.M.B.Cordeiro, P.St.J.Russell, "Guidance properties of low-contrast photonic bandgap fibres", Opt. Express 13, pp 2503, 2005.
- [Arkwright 91] J. W. Arkwright, D. B. Mortimore and R. M. Adnams, "Monolithic 1x19 single-mode fused fibre couplers", Electron. Lett. 27, pp 737, 1991.
- [Bansal 86] N.P. Bansal and R. H. Doremus, "Handbook of Glass Properties", Academic Press(San Diego), 1986.
- [Bilodeau 88] F. Bilodeau, K. O. Hill, S. Faucher and D. C. Johnson, "Low-loss highly overcoupled fused couplers: fabrication and sensitivity to external pressure", IEEE J. Lightwave Technol. 6, pp 1476, 1988.
- [Bird 05] Prof. D. Bird calculations, private personal communications.
- [Birks 92] T. A. Birks and Y. W. Li, "The shape of fiber tapers", IEEE J. Lightwave Technol. 10, pp 432, 1992.
- [Birks 94] T. A. Birks, S. G. Farwell, P. St.J. Russell, C. N. Pannell, "Four-port fiber frequency shifter with a null taper coupler", Opt. Lett. 19, pp 1964, 1994.
- [Birks 95a] T. A. Birks, D. O. Culverhouse, S. G. Farwell and P. St.J. Russell, "All-fiber polarizer based on a null taper coupler", Opt. Lett. 20, pp 1371, 1995.
- [Birks 95b] T. A. Birks, P. J. Roberts, P. St. J. Russell, D. M. Atkin, T. J. Shepherd, "Full 2-D photonic bandgaps in silica/air structures", Electron. Lett. 31, pp 1941, 1995.
- [Birks 97] T.A. Birks, J.C. Knight, and P.St.J. Russell, "Endlessly single-mode photonic crystal fibre," Opt. Lett. 22, pp 961, 1997.
- [Birks 99] T. A. Birks, D. Mogilevtsev, J. C. Knight, P. St.J. Russell, J. Broeng, P. J. Roberts, J. A. West, D. C. Allen, J. C. Fajardo, "The analogy between photonic crystal fibres and step index fibres", Proc. Opt. Fiber Commun. Conf. (OFC '99, San Diego, California) paper FG4, 1999.
- [Birks 00] T. A. Birks, W. J. Wadsworth and P. St.J. Russell, "Supercontinuum generation in tapered fibers", Opt. Lett. 25, pp 1415, 2000.
- [Birks 02] T.A. Birks, G. Kakarantzas, P.St.J. Russell and D.F.Murphy, "Photonic crystal fibre devices", Proc SPIE, 4943, pp 142, 2002.



[Birks 04] T. A. Birks, D. M. Bird, T. D. Hedley, J. M. Pottage, P. St. J. Russell, "Scaling laws and vector effects in bandgap-guiding fibres," *Opt. Express* 12, pp 69, 2004.

[Birks 05a] T.A.Birks, S.G.Leon-Saval, W.J.Wadsworth, P.St.J.Russell, "Optical micro- and nano-structures using fibre tapers", Proc. Conference on Lasers and Electro-Optics (CLEO'05, Baltimore, Maryland) paper CMD1, 2005.

[Birks 05b] T.A.Birks, S.G.Leon-Saval, J.Bland-Hawthorn, M.Englund, "Adiabaticity in multicore fibre transitions", Proceedings of the Workshop on Optical Waveguide Theory and Numerical Modelling (Sydney, Australia), July 2005, p.19 (*invited*).

[Bise 02] R. T. Bise, R. S. Windeler, K. S. Kranz, C. Kerbage, B. J. Eggleton, D. J. Trevor, "Tunable photonic bandgap fiber", *Optical Fiber Communication*, Vol. 70 of OSA Trends in Optics and Photonics (Optical Society of America, Washington, D.C.), pp 466, 2002.

[Black 87] R. J. Black, J. Lapierre, J. Bures, "Field evolution in doubly clad lightguides," *IEE Proc. Pt. J.* 134, pp 105, 1987.

[Bland-Hawthorn 04] J. Bland-Hawthorn, M. Englund and G. Edvell, "New approach to atmospheric OH suppression using an aperiodic fibre Bragg grating", *Opt. Express* 12, pp 5902, 2004.

[Brambilla 04] G. Brambilla, V. Finazzi, D. J. Richardson, "Ultra-low-loss optical fiber nanotapers", *Opt. Express* 12, pp 2258, 2004.

[Brinker 90] C.J. Brinker and G.W. Scherer, "Sol-Gel Science: The Physics and Chemistry of Sol-Gel Processing", Academic Press(New York), 1990.

[Buck 95] J. A. Buck, "Fundamentals of Optical Fibers", John Wiley and Sons(New York),1995.

[Bures 99] J. Bures and R. Ghosh, "Power density of the evanescent field in the vicinity of a tapered fiber", *J. Opt. Soc. Am. A* 16, pp 1992, 1999.

[Burns 86] W.K. Burns, M. Abebe, C.A. Villarruel and R.P. Moeller, "Loss mechanisms in single-mode fiber tapers", *J. Lightwave Tech.*, Vol. LT4, No. 6, 1986.

[Chandalia 01] J.K. Chandalia, B.J. Eggleton, R.S. Windeler, S.G. Kosinski, X. Liu, C. Xu, "Adiabatic coupling in tapered air-silica microstructured optical fiber", *IEEE Photonics Tech. Lett.* 13 (1), pp 52, 2001.

[Coen 01] S. Coen, A. Chau, R. Leonhardt, J. D. Harvey, J. C. Knight, W. J. Wadsworth and P. St.J. Russell, "White-light supercontinuum generation with 60-ps pump pulses in a photonic crystal fiber", *Opt. Lett.* 26, 1356-1358 (2001).

[Cordeiro 05] C. M. B. Cordeiro, W. J. Wadsworth, T. A. Birks and P. St.J. Russell, "Engineering the dispersion of tapered fibers for supercontinuum generation with a 1064 nm pump laser", *Opt. Lett.* 30, pp 1980, 2005.

[Cregan 99] R. F. Cregan, B. J. Managan, J. C. Knight, T. A. Birks, P. St. J. Russell, P. J. Roberts, D. C. Allen, "Single-mode photonic bandgap guidance of light in air", *Science* 285, pp 1537, 1999.

[Dimmick 99] T.E.Dimmick, G.Kakarantzas, T.A.Birks, P.St.J.Russell, "CO<sub>2</sub> laser fabrication of fused fiber couplers and tapers", *Applied Optics* 38, pp 6845, 1999.

[Dudley 02a] J.M. Dudley, L. Provino, N. Grossard, H. Maillotte, R. S. Windeler, B. J. Eggleton, and S. Coen, "Supercontinuum generation in air-silica microstructured fibers with nanosecond and femtosecond pulse pumping", *J. Opt. Soc. Am. B* 19, pp 765, 2002.

[Dudley 02b] J.M. Dudley, S. Coen, "Coherence properties of supercontinuum spectra generated in photonic crystal and tapered optical fibers", *Opt. Lett.* 27, pp 1180, 2002.

[Efimov 03] A.Efimov, A.J.Taylor, F.G.Omenetto, J.C.Knight, W.J.Wadsworth, P.St.J.Russell, "Nonlinear generation of very high-order UV modes in microstructured fibers", *Opt. Express* 11, pp 910, 2003.

[Erdogan 97] T. Erdogan, "Cladding-mode resonances in short- and long-period fiber grating filters", *J. Opt. Soc. Am A* 14, pp 1760, 1997.

[Espindola 99] R. P. Espindola, R. S. Windeler, A. A. Abramov, B. J. Eggleton, T. A. Strasser and D.J. DiGiovanni, "External refractive index insensitive air-clad long period fibre grating", *Electron. Lett.* 35, pp 327, 1999.

[Flockhart 03] G. M. H. Flockhart, W. N. MacPherson, J. S. Barton, J. D. C. Jones, L. Zhang, and I. Bennion, "Two-axis bend measurement with Bragg gratings in multicore optical fiber", *Opt. Lett.* 28, pp 387, 2003.

[Foster 04] M. A. Foster, A. L. Gaeta, "Ultra-low threshold supercontinuum generation in sub-wavelength waveguides", *Opt. Express* 12, pp 3137, 2004.

[Gambling 77] W. A. Gambling, H. Matsumura, "Simple characterisation factor for practical single-mode fibres", *Electron. Lett.* 13, pp 691, 1977.

[Ghosh 94] G. Ghosh, "Temperature dispersion of refractive-indexes in some silicate fiber glasses", *IEEE Photon. Technol. Lett.* 6, pp 431, 1994.

[Gnauck 00] A. H. Gnauck, L. D. Garrett, Y. Danziger, U. Levy and M. Tur, "Dispersion and dispersion-slope compensation of NZDSF over the entire C band using higher-order-mode fibre", *Electron. Lett.* 36, pp 1946, 2000.

[Hecht 99] J. Hecht, "Understanding Fiber Optics", Prentice Hall(Columbus), 1999.

[Hench 90] LL. Hench, J. K. West, "The sol-gel process", *Chem. Rev.* 90, pp 33, 1990.

[Hoang 97] G. C. Hoang, H. S. Lee, "Properties and Applications of Dielectric Materials", *Proc. of the 5<sup>th</sup> International Conference* vol.1, pp 174, 1997.

[Jedrzejewski 86] K.P.Jedrzejewski, F.Martinez, J.D.Minelly, C.D.Hussey, F.P.Payne, "Tapered-beam expander for single-mode optical-fiber gap devices", *Electron. Lett.* 22, pp 105, 1986.

[Jensen 82] S. M. Jensen, "Analysis of nonlinear dual-core waveguides for switching operation," *IEEE J. Quantum Electron.* QE- 18, pp 1580, 1982.

[Joannopoulos 95] J. D. Joannopoulos, R. D. Meade, J. N. Winn, "Photonic Crystals", Princeton University Press, 1995.

- [Johnson 01] S. G. Johnson and J. D. Joannopoulos, "Block-iterative frequency-domain methods for Maxwell's equations in a planewave basis", *Opt. Express* 8, pp 173, 2001.
- [Kakarantzas 01] G. Kakarantzas, B.J. Mangan, T.A. Birks, J.C. Knight and P.St.J. Russell, "Directional coupling in a twin-core photonic crystal fiber using heat treatment", *Proc. of Conference on Lasers & Electro-Optics (CLEO'01, Baltimore, Maryland)*, paper JTuD2, 2001.
- [Kakarantzas 02] G. Kakarantzas, T.A. Birks and P.St.J. Russell, "Structural long-period gratings in photonic crystal fibers", *Opt. Lett.* 27, pp 1013, 2002.
- [Kakarantzas 04] G.Kakarantzas, S.G.Leon-Saval, T.A.Birks, P.St.J.Russell, "Low-loss deposition of sol-gel derived silica films on tapered fibers", *Opt. Lett.* 29, pp.694, 2004.
- [Kashyap 99] R. Kashyap, "Fibre Bragg Gratings", Academic Press(San Diego), 1999.
- [Keck 73] D.B. Keck, R.D. Maurer, and P.C. Schultz, "On the ultimate lower limit of attenuation in glass optical waveguides", *Applied Physics Letters* 22, pp 307, 1973.
- [Keddie 91] J.L. Keddie and E.P. Giannelis, "Mechanism and kinetics of sol-gel oxide thin film formation", presented at 6<sup>th</sup> Int. Workshop on Glasses and Ceramics from Gels, 1991.
- [Kingery 59] W.D. Kingery, "Surface tension of some liquid oxides and their temperature coefficients", *J. Am. Ceramic Soc.* 42, pp 6, 1959.
- [Knight 96] J.C. Knight, T.A. Birks, P.St.J. Russell, and D.M. Atkin, "All-silica single-mode fiber with photonic crystal cladding", *Opt. Lett.* 21, pp 1547, 1996; Errata, *Opt. Lett.* 22, pp 484, 1997.
- [Knight 98] J. C. Knight, T. A. Birks, R. F. Cregan, P. St. J. Russell and J. -P. de Sandro, "Large mode area photonic crystal fibre", *Electron. Lett.* 34, pp 1347, 1998.
- [Ladouceur 90] F. Ladouceur and J. D. Love, "Multiport single-mode fibre splitters", *Opt. Quantum Electron.* 22, pp 453, 1990.
- [Lægsgaard 04] J. Lægsgaard, "Gap formation and guided modes in photonic bandgap fibres with high-index rods", *J. Opt. A* 6, pp 798, 2004.
- [Landau 42] L. D. Landau, B. G. Levich, *Acta Physiochim (U.R.S.S.)* 17, pp 42, 1942.
- [Leon-Saval 04a] S.G.Leon-Saval, T.A.Birks, W.J.Wadsworth, P.St.J.Russell, M.W.Mason, "Efficient single-mode supercontinuum generation in submicron-diameter silica-air fibre waveguides", *Proceedings of the Conference on Lasers and Electro-Optics (CLEO, San Francisco, California)*, May 2004, *postdeadline paper* CPDA6.
- [Leon-Saval 04b] S.G.Leon-Saval, T.A.Birks, W.J.Wadsworth, P.St.J.Russell, M.W.Mason, "Supercontinuum generation in submicron fibre waveguides", *Opt. Express*, 12, 2864, 2004.
- [Leon-Saval 05a] S.G.Leon-Saval, T.A.Birks, N.Y.Joly, A.K.George, W.J.Wadsworth, G.Kakarantzas, P.St.J.Russell, "Splice-free interfacing of photonic crystal fibers", *Opt. Lett.* 30, pp 1629, 2005.
- [Leon-Saval 05b] S.G.Leon-Saval, T.A.Birks, A.K.George, W.J.Wadsworth, P.St.J.Russell, "Wavelength-independent high-extinction fibre mode convertor", *Proceedings of the*

Conference on Lasers and Electro-Optics (CLEO, Baltimore, Maryland), May 2005, paper CThZ2.

[Leon-Saval 05c] S.G.Leon-Saval, T.A.Birks, J.Bland-Hawthorn, M.Englund, "Single-mode performance in multimode fibre devices", Proceedings of the Optical Fiber Communication Conference (OFC, Anaheim, California), March 2005, *postdeadline paper* PDP25.

[Leon-Saval 05d] S.G.Leon-Saval, T.A.Birks, J.Bland-Hawthorn, M.Englund: "Multimode fibre devices with single-mode performance", Opt. Lett. 30, pp 2545, 2005.

[Liu 01] X. Liu, C. Xu, W. H. Knox, J. K. Chandalia, B. J. Eggleton, S. G. Kosinski and R. S. Windeler, "Soliton self-frequency shift in a short tapered air-silica microstructure fiber", Opt. Lett. 26, pp 358, 2001.

[Li 85] T. Li (ed.), "Optical Fiber Communications: Fiber Fabrication", Academic Press(San Diego), Vol. 1, 1985.

[Lines 99] M. E. Lines, W. A. Reed, D. J. Di Giovanni, J. R. Hamblin, "Explanation of anomalous loss in high delta single-mode fibres", Electron. Lett. 35, pp 1009, 1999.

[Litchinitser 03] N. M. Litchinitser, S. C. Dunn, B. Usner, B. J. Eggleton, T. P. White, R. C. McPhedran, C. M. de Sterke, "Resonances in microstructured optical waveguides," Opt. Express 11, pp 1243, 2003.

[Lizé 04] Y. K. Lizé, E. C. Mägi, V. G. Ta'eed, J. A. Bolger, P. Steinvurzel, B. J. Eggleton "Microstructured optical fiber photonic wires with subwavelength core diameter" Opt. Express 12, 3209 (2004).

[Love 86] J.D. Love and W.M. Henry, "Quantifying loss minimisation in single mode fibre tapers", Electron. Lett. 22, pp 912, 1986.

[Love 87] J.D. Love, "Spot size, adiabaticity and diffraction in tapered fibres," Electron. Lett. 23, pp 993, 1987.

[Luan 04] F. Luan, A. K. George, T. D. Hedley, G. J. Pearce, D. M. Bird, J. C. Knight, P. St. J. Russell, "All-solid photonic bandgap fiber", Opt. Lett. 29, pp 2369, 2004.

[Magi 04] E. C. Magi, P. Steinvurzel, B. J. Eggleton, "Tapered photonic crystal fibers", Opt. Express 12, pp 776, 2004.

[Mangan 00] B.J. Mangan, J.C. Knight, T.A. Birks, P.St.J. Russell and A.H. Greenaway, "Experimental study of dual-core photonic crystal fibre", Electron. Lett., 36, pp 1358, 2000.

[Milam 76] D. Milan and M. J. Weber, "Measurement of nonlinear refractive-index coefficients using time-resolved interferometry - application to optical-materials for high-power neodymium lasers", J. Appl. Phys. 47, pp 2497, 1976.

[Mizunami 00] T. Mizunami, T. V. Djambova, T. Niiho and S. Gupta, "Bragg gratings in multimode and few-mode optical fibers", IEEE J. Lightwave Technol. 18, pp 230, 2000.

[Mortimore 91] D. B. Mortimore and J. W. Arkwright, "Monolithic wavelength-flattened 1x7 single-mode fused fiber couplers: theory, fabrication, and analysis", Appl. Opt. 30, pp 650, 1991.

[Nagel 82] S.R. Nagel, J.B. MacChesney, and K.L. Walker, "An overview of the modified chemical vapor deposition (mcvd) process and performance", *IEEE J. of Quant. Electron.*, pp 459, 1982.

[Nguyen 05] H.C. Nguyen, B.T. Kuhlmeier, M.J. Steel, C.L. Smith, E.C. Magi, R.C. McPhedran, B.J. Eggleton, "Leakage of the fundamental mode in photonic crystal fiber tapers", *Opt. Lett.* 30, pp 1123, 2005.

[Ortigosa-Blanch 02] A. Ortigosa-Blanch, J.C. Knight and P.St.J. Russell: "Pulse breaking and supercontinuum generation with 200-fs pump pulses in photonic crystal fibers," *J. Opt. Soc. Am. B* 19, pp 2567, 2002.

[Ozeki 75] T. Ozeki, T. Ito and T. Tamura, "Tapered section of multimode cladded fibers as mode filters and mode analyzers", *Appl. Phys. Lett.* 26, pp 386, 1975.

[Pajonk 98] G.M. Pajonk, "Transparent silica aerogels", *J. Non-Cryst. Solids* 225, pp 307, 1998.

[Pierre 02] A.C. Pierre, G.M. Pajonk, "Chemistry of aerogels and their applications", *Chem. Rev.* 102, pp 4243, 2002.

[Poole 94] C. D. Poole, J. M. Wiesenfeld, D. J. DiGiovanni and A. M. Vengsarkar, "Optical fiber-based dispersion compensation using higher order modes near cut-off", *IEEE J. Lightwave Technol.* 17, pp 1746, 1994.

[Prassas 84] M. Prassas and L.L. Hench, "Ultrastructure Processing of Ceramics, Glasses, and Composites", John Wiley & Sons (New York), pp. 100-125, 1984.

[Provino 01] L. Provino, J. M. Dudley, H. Maillotte, N. Grossard, R. S. Windeler and B. J. Eggleton, "Compact broadband continuum source based on microchip laser pumped microstructured fibre", *Electron. Lett.* 37, pp 558, 2001.

[Ramachandran 02] S. Ramachandran, Z. Wang, M. Yan, "Bandwidth control of long-period grating-based mode converters in few-mode fibers", *Opt. Lett.* 27, pp 698, 2002.

[Ranka 00] J. K. Ranka, R. S. Windeler and A. J. Stentz, "Visible continuum generation in air-silica microstructure optical fibers with anomalous dispersion at 800 nm", *Opt. Lett.* 25, pp 25, 2000.

[Rao 94] A. V. Rao, G.M. Pajonk, N.N. Parvathy, "Effect of solvents and catalysts on monolithicity and physical properties of silica aerogels", *J. Mat. Sci.* 29, pp 1807, 1994.

[Reeves 03] W.H. Reeves, D.V. Skryabin, F. Biancalana, J.C. Knight, P. St.J. Russell, F. Ominetto, A. Efimov, and A.J. Taylor, "Transformation and control of ultra-short pulses in dispersion-engineered photonic crystal fibres", *Nature* 424, pp 511, 2003.

[Riishede 04] J. Riishede, J. Lægsgaard, J. Broeng, A. Bjarklev, "All-silica photonic bandgap fibre with zero dispersion and a large mode area at 730 nm", *J. Opt. A* 6, pp 667, 2004.

[Russell 03] P.St.J. Russell, "Photonic Crystal Fibers", *Science* 299, pp 359, 2003.

[Salathe 96] R.P. Salathe, H. Gilgen, G. Bodmer, "Coupled-mode propagation in multicore fibers characterized by optical low-coherence reflectometry", *Opt. Lett.* 21, pp 1006, 1996.

[Schiffner 80] G. Schiffner, H. Schneider and G. Schoner, "Double-core single-mode optical fiber as directional coupler", *Applied Physics*, 23, pp 41, 1980.

[Schmidt 90] H.K. Schmidt, in: "Better Ceramics Through Chemistry IV", *Mater. Res. Soc. Symp. Series* (Materials Research Society, Pittsburgh, PA), Vol. 180, p. 961, 1990.

[Seo 03] J. T. Seo, Q. Yang, S. Creekmore, B. Tabibi, D. Temple, S. Y. Kim, K. Yoo, A. Mott, M. Namkung, S. S. Jung, "Large pure refractive nonlinearity of nanostructure silica aerogel" *Appl. Phys. Lett.* 82, pp 4444, 2003.

[Shen 84] Y. R. Shen, "Principles of nonlinear optics", Wiley(New York), 1984.

[Smith 03] C. M. Smith, N. Venkataraman, M. T. Gallagher, D. Muller, J. A. West, N. F. Borrelli, D. C. Allan, K. W. Koch, "Low-loss hollow-core silica/air photonic bandgap fibre," *Nature* 424, pp 657, 2003.

[Snyder 83] A. W. Snyder, J. D. Love, "Optical Waveguide Theory", Chapman and Hall(London), 1983.

[Sprehn 98] G.A.Sprehn et al "Aerogel-clad optical fiber" US patent number 5684907 (1997); K.Tsubaki et al "Optical fiber" US patent number 5790742, 1998.

[Stewart 85] W.J. Stewart and J.D. Love, "Design limitation on tapers and couplers in single mode fibres", *Proc. ECOC'85* (Venice), pp. 559, 1985.

[Su 05] L. Su and C. Lu, "Multimode fiber Bragg grating based lasers and optical sensors", *Proc. Conference Optical Fiber Components (OFC'05, Anaheim, California)*, paper OME16, 2005.

[Sun 03] Y. Sun, T. Szkopek and P. W. E. Smith, "Demonstration of narrowband high-reflectivity Bragg gratings in a novel multimode fiber", *Opt. Commun.* 223, pp 91, 2003.

[Tabor 69] D. Tabor, "Gases, Liquids and Solids," Penguin Books (Harmondsworth, UK), 1969.

[Tajima 94] K. Tajima, M. Tateda and M. Ohashi, "Viscosity of GeO<sub>2</sub>-doped silica glasses", *IEEE J. Lightwave Technol.* 12, pp 411, 1994.

[Taylor 92] D.J. Taylor, B.D. Fabes, "Laser Processing of Sol-gel Coatings", *J. Non-Cryst. Solids* 147, pp 457, 1992.

[Teipel 03] J. Teipel, K. Franke, D. Turke, F. Warken, D. Meiser, M. Leuschner, H. Giessen, "Characteristics of supercontinuum generation in tapered fibers using femtosecond laser pulses", *Appl. Phys. B* 77, pp 245, 2003.

[Thomas 00] G.A. Thomas, B. I. Shraiman, P. F. Glodis, and M.J. Stephen, "Towards the clarity limit in optical fibre", *Nature* 404, pp 262, 2000.

[Tong 03] L. Tong, R. G. Gattas, J. A. Ashcom, S. He, J. Lou, M. Shen, I. Maxwell and E. Mazur, "Subwavelength-diameter silica wires for low-loss optical wave guiding", *Nature* 426, pp 816, 2003.

[Tong 04] L. Tong, J. Lou and E. Mazur, "Single-mode guiding properties of subwavelength-diameter silica and silicon wire waveguides", *Opt. Express* 12, pp 1025, 2004.

[Tong 05] L.Tong, J.Lou, R.R.Gattass, S.He, X.Chen. L.Liu, E.Mazur, "Assembly of silica nanowires on silica aerogels for microphotonic devices", *Nano Lett.* 5, pp 259, 2005.

[Villeneuve 92] P. R. Villeneuve, M. Piché, "Photonic bandgaps in two-dimensional square and hexagonal lattices", *Phys.Rev. B* 48, pp 4969, 1992.

[Wadsworth 02] W.J. Wadsworth, A. Ortigosa-Blanch, J.C. Knight, T.A. Birks, T-P.M. Man and P. St.J. Russell, "Supercontinuum generation in photonic crystal fibres and optical fibre tapers: A novel light source", *J. Opt. Soc. Am. B* 19, pp 2148, 2002.

[Wadsworth 04a] W. J. Wadsworth, N. Joly, J. C. Knight, T. A. Birks, F. Biancalana and P. St.J. Russell, "Supercontinuum and four-wave mixing with Q-switched pulses in endlessly single-mode photonic crystal fibres", *Opt. Express* 12, pp 299, 2004.

[Wadsworth 04b] W. J. Wadsworth, R. M. Percival, G. Bouwmans, J. C. Knight, T. A. Birks, T. D. Hedley and P. St.J. Russell, "Very high numerical aperture fibers", *IEEE Photon. Technol. Lett.* 16, pp 843, 2004.

[Wadsworth 05] W.J.Wadsworth, A.Witkowska, S.G.Leon-Saval, T.A.Birks, "Hole inflation and tapering of stock photonic crystal fibres", *Opt. Express*, 13, pp 6541, 2005.

[Wagh 99] P.B. Wagh, R. Begag, G.M. Pajonk, A.V. Rao, D. Haranath, "Comparison of some physical properties of silica aerogel monoliths synthesized by different precursors", *Mat. Chem. and Phys.* 57, pp 214, 1999.

[White 02] T. P. White, R. C. McPhedran, C. M. de Sterke, N. M. Litchinitser, B. J. Eggleton, "Resonance and scattering in microstructured optical fibers", *Opt. Lett.* 27, pp 1977, 2002.

[Witkowska 05] A. Witkowska, W. J. Wadsworth, S. G. Leon-Saval, T. A. Birks, "Novel optical devices made by inflating the holes of a photonic crystal fibre", *Photonex Europe 05*, Coventry (UK), 2005.